High p_T Charged Hadron Production at RHIC

Dissertation
presented for the degree of
Doctor of Philosophy in Physics
by

CLAUS O. E. JØRGENSEN

SEPTEMBER 20, 2004

NIELS BOHR INSTITUTE
FACULTY OF SCIENCE – UNIVERSITY OF COPENHAGEN

High p_T Charged Hadron Production at RHIC

by Claus O. E. Jørgensen
Supervisor: Prof. Dr. Jens Jørgen Gaardhøje

This dissertation is approved by:

Prof. Dr. John Renner Hansen (chair)
University of Copenhagen

Dr. Jurgen Schukraft
CERN

Prof. Dr. Thomas Peitzmann
Univertsity of Utrecht

2004

NIELS BOHR INSTITUTE
FACULTY OF SCIENCE – UNIVERSITY OF COPENHAGEN

Preface

A new era in the field of relativistic heavy ion physics began in the summer of 2000 when the Relativistic Heavy Ion Collider (RHIC) at Brookhaven National Laboratory, USA, started operating. The center of mass energy of the nuclear collisions produced by this new machine is an order of magnitude higher than what has been produced previously in the laboratory. The collisions were therefore expected to exhibit new features and reveal fundamental structures of hot and dense hadronic matter. Today, four years later, a general understanding of collisions in this energy regime has been acquired. The experimental and theoretical studies are now focused on the more detailed description of the created matter and its properties.

Even though many details in the picture are missing, it is clear that a major discovery has been made at RHIC. In the early stages of a head on collision between two heavy ions, the hadronic structure of matter is dissolved and an extended region of strongly interacting quarks and gluons, no longer confined in hadrons, is created.

One of the key observations leading to the discovery, is the suppression or quenching of jets in the central collisions. Jets are used to probe the dense matter created in the collisions and the strong suppression of jets evidences very high densities in the early stages of the collisions. The subject of this thesis is the production of high transverse momentum p_T particles, related to the production and modification of jets in the high density medium created in the collisions. The high p_T measurements presented here have been made with the BRAHMS detector during the 2002 and 2003 runs. The collision systems in these experiments were $p+p$, $d+Au$ and $Au+Au$ at a center–of–mass energy of 200 GeV per nucleon. Also, preliminary results of high p_T hadron production in $Au+Au$ collisions at center–of–mass energy of 62.4 GeV per nucleon (from the 2004 RHIC run) is presented.

Personally, I started working with BRAHMS in 1999 when I wrote my bachelor project on the time resolution of the BRAHMS time–of–flight detectors. Later, in 2001, I wrote my master thesis, which included some of the first results from RHIC. The subject was charged particle production in $Au+Au$ collisions at a center–of–mass energy of 130 GeV per nucleon. In 2001, I started my Ph.D. studies on high p_T particle production at RHIC. I have therefore been in the lucky position where I have been able to follow the development of a heavy ion experiment, from the first detectors were installed in the experimental hall to the discovery of new physics. I have been involved in detector systems tests, helping out with the typical student tasks like pulling kilometers of cables, taking endless night shifts, analyzing of the data, developing and maintaining of software, writing papers and presenting results at conferences. The BRAHMS experiment is small enough to allow a student to get involved in more or less all the tasks and to figure out how things work (and what doesn't work). It is also small enough to get to know the people in the collaboration (see appendix D), which makes it easier to understand what is going on. All in all, it has been a great experience and I have learned a lot about physics and how physicists work.

This thesis concludes what I have been doing the last three years – or at least, a large part of the physics my work has evolved around. The thesis is written with different purposes in mind. First, it is meant to describe my contribution to the field of heavy ion high p_T physics. Second, it is meant to put the presented results into the context of high p_T physics and heavy ion physics at RHIC energies in general. Finally, it contains elements of an *analysis guide* to help future BRAHMS students. It has been a difficult task to find a balance between the different purposes. I hope both master students and professors in heavy ion physics can read it without getting (too) lost or (too) bored. The use of technical language has been kept on a level that a student in heavy ion physics should be able to understand. Definition of variables and coordinate systems used throughout the thesis are given in appendix A.

Details on the high p_T analysis are found in chapter 5 while the results are presented and discussed in chapter 6. Chapter 2 contains (an experimentalists understanding) of the theory behind high p_T particle production. The idea of this chapter is to give intuitive pictures of the different mechanisms that influences the particle production at high p_T and to give a theoretical basis for the discussions in chapter 6. Chapter 3 describes the experimental setup – this is done very briefly since detailed descriptions can be found elsewhere. In chapter 4 the general data reconstruction is explained. Special focus is here put on the angular and momentum resolution of the spectrometers (since this is important for the high p_T measurements) and on the reconstruction of the signals in the BRAHMS Cherenkov counters (since this is what I worked on the first year of my Ph.D.). Chapter 1 contains a short general introduction to high energy heavy ion physics and a brief review of the RHIC results.

Acknowledgements

I owe a great thanks to the many people that have helped and inspired me during the last three years. First of all, I would like to thank Jens Jørgen Gaardhøje, who first inspired me to join the HEHI group and has been an excellent supervisor during the last six years. Thanks also to the people I've worked closely together with. I'm here thinking about Djamel Ouerdane (who fixed a large amount of my bugs and kept a high spirit, even in the stressed periods) and Ian Bearden (who have always managed to motivate us students to do our best). Thanks for the good team–work! Former and present members of the HEHI group have created a nice working atmosphere, I'd like to thank Ole Hansen, Peter Christiansen, Pawel Staszel, Hans Bøggild, Truls Larsen, Catalin Ristea, Christian Christensen, Davis Sandberg, Erik Jakobsen and Marco Germinario (not to mention all the others). I have had some contact with the local theorists at NBI (and Nordita). Thanks to Ralf Rapp and Boris Tomášik for the useful discussions (and explanations). The periods I've spent in Brookhaven have been the most instructive periods of my Ph.D. My special thanks go to Flemming Videbæk who taught me a lot about experimental heavy ion physics. Also, thanks to the rest of the BRAHMS collaboration – it's been fun working with you. During the fall of 2003 I spend four weeks at Giessen University (Germany) working on software for the HADES and the PANDA experiments. Thanks to Wolfgang Kühn, James Ritmann, Tiago Perez and Alberica Toia for making it such a pleasant stay. Also people outside the physics community have supported and inspired me. In particular, I'm thinking about my family who have always supported and encouraged me. Special thanks also to Kasper Bech, Peter Bonnén, Ulrik Hübbe, Karl Roos and Adam Simonsen. Finally, I'd like to thank the people who have taken the time to read and comment this work during the last hectic weeks: Ole Hansen, Jens Jørgen Gaardhøje, Djamel Ouerdane, Truls Larsen and Finn E. Jørgensen.

Contents

1 Heavy Ion collisions at RHIC **1**
1.1 Quantum Chromo Dynamics and the Quark Gluon Plasma . . . 1
1.1.1 Basics of Quantum Chromo Dynamics . . . 1
1.1.2 The Quark Gluon Plasma . . . 2
1.2 High Energy Heavy Ion Collisions . . . 3
1.2.1 The Collision Geometry . . . 4
1.2.2 The Collision Evolution . . . 5
1.3 Results from RHIC . . . 6
1.3.1 Charged Particle Multiplicity . . . 6
1.3.2 Soft Spectra – Thermal Freeze Out . . . 6
1.3.3 Elliptic Flow – a Sign of Early Thermalization . . . 7
1.3.4 Particle Ratios – Chemical Freeze Out . . . 8
1.3.5 Net Proton Distribution – Baryon Stopping . . . 9
1.3.6 Initial Energy Density – The Bjorken Prescription . . . 9
1.3.7 Conclusions from RHIC . . . 10

2 High p_T Particle Production **11**
2.1 Jet Production . . . 12
2.2 The Nuclear Modification Factor . . . 13
2.3 Nuclear Modifications . . . 13
2.3.1 Cronin Enhancement . . . 14
2.3.2 Nuclear Shadowing . . . 15
2.3.3 Saturation . . . 16
2.3.4 Jet Quenching . . . 16
2.3.5 Remarks . . . 18
2.4 Models . . . 18
2.4.1 Shadowing and Jet Quenching in HIJING . . . 18
2.4.2 Vitev-Gyulassy . . . 20
2.4.3 Cassing-Gallmeister-Greiner . . . 21
2.4.4 Hirano–Nara . . . 22
2.5 The Color Glass Condensate . . . 23

3 The Experimental Setup **25**
3.1 The Relativistic Heavy Ion Collider . . . 25
3.1.1 The Interaction Region . . . 26
3.2 The BRAHMS Experiment . . . 26
3.2.1 Basic Idea of the Setup . . . 26
3.2.2 Acceptance . . . 27
3.2.3 Global Detectors . . . 28
3.2.4 Spectrometer Components . . . 30

3.2.5 Triggers . . . 33

4 Data Reconstruction **35**
4.1 Event Characterization . . . 35
4.1.1 Vertex Determination . . . 35
4.1.2 Centrality Determination . . . 36
4.2 Track Reconstruction . . . 38
4.2.1 Local Tracking . . . 38
4.2.2 Track Matching . . . 38
4.2.3 Global Tracking . . . 40
4.2.4 Angular and Momentum Resolution . . . 40
4.3 Particle Identification . . . 45
4.4 The Cherenkov Reconstruction . . . 45
4.4.1 C1 Reconstruction . . . 46
4.4.2 RICH Reconstruction . . . 47

5 High p_T Analysis **55**
5.1 Event Selection . . . 55
5.2 Track Selection . . . 57
5.3 Scaling Up the Number of Events/Tracks . . . 58
5.4 Corrections . . . 59
5.4.1 Acceptance Correction . . . 59
5.4.2 Efficiency Correction . . . 62
5.4.3 Decay Correction . . . 64
5.4.4 Transverse Momentum Smearing Correction . . . 64
5.4.5 Bin Shift Correction . . . 66
5.4.6 Correction Summary . . . 66
5.5 Making Spectra . . . 67
5.5.1 The $Au + Au$, $d + Au$ and $p + p$ Analyses . . . 68
5.6 The Reference Spectra . . . 69
5.7 Calculating the Number of Binary Collisions . . . 71
5.8 Systematic Errors . . . 72

6 Results and Discussion **75**
6.1 The Spectra . . . 75
6.2 The Nuclear Modification . . . 76
6.2.1 Comparison to Models . . . 82
6.3 Consistency of RHIC Results . . . 83
6.4 Other High p_T Measurements . . . 84
6.4.1 Identified Particles . . . 84
6.4.2 Back-to-back Jets . . . 85

7 Conclusion **87**

A Variables and the Coordinate Systems **89**

B The Power–Law **91**

C Bending Angle Resolution Derivation **92**

D The BRAHMS Collaboration **93**

Chapter 1

Heavy Ion collisions at RHIC

This chapter gives a short introduction to ultra relativistic heavy ion physics. First, the theoretical description of hot and dense strongly interacting matter is introduced. The theory of the strong interaction motivates the field of experimental heavy ion physics, which is the subject of the second part of the chapter. The collision geometry and the present understanding of the collision evolution are sketched in section 1.2.1 and 1.2.2. In the last part of the chapter, some of the main results from the first years of RHIC operation are reviewed and interpreted.

1.1 Quantum Chromo Dynamics and the Quark Gluon Plasma

The standard model describes matter as built up of quarks and leptons, which interact via gauge bosons. The dominant interaction in hadronic physics is the strong interaction and the mediator of this interaction is the gluon. The strong interaction is described by Quantum Chromo Dynamics (QCD) which dictates the characteristic structure of hadronic matter. Among the consequences of the theory is the prediction of a state of matter, in which the quarks and gluons are not confined in hadrons, the so called quark gluon plasma (QGP).

1.1.1 Basics of Quantum Chromo Dynamics

The word *chromo* reflects that QCD introduces a charge called color, carried by both quarks and gluons. Color charges are red, green or blue (or the corresponding anti–charges). Colored particles interact strongly, and the fact that gluons are colored has important implications for the structure of hadronic matter. The gluon-gluon coupling leads to a complicated form of the strength of the interaction. As the momentum transfer between the strongly interacting particles becomes larger, (or, from uncertainty principle, the distance shorter) the effective coupling becomes smaller and vice versa, as shown in figure 1.1. The effective potential between two colored objects grows linearly with distance in the strong coupling regime, i.e. at large distances, and is therefore very different from the potentials of the other fundamental forces.

When the quarks approach each other, the effective coupling becomes weaker and at very small distances it almost vanishes. This is called the *asymptotic freedom.* When the distance between quarks grows, the effective coupling grows and at some point the energy becomes large enough to from a new quark–antiquark pair. These new quarks combine with the original ones and new hadrons are formed. Intuitively, one can think of the color field between the quarks as confined in a small tube. The gluon-gluon interaction makes the tube radius approximately constant and as the quarks are separated, the color flux in the tube grows. Eventually the tube breaks and energy is converted into new particles. One consequence of the growing quark-quark potential is that a single quark cannot be observed – quarks are confined in systems of two or more quarks. These systems are colorless, which means that they either contain the same amount of all three color charges (red, green and blue) or the same number of color and anti-color charges. The common configurations are

$q_r q_g q_b$ (baryons) or $q_c \bar{q}_c$ (mesons), but both QCD calculations and recent measurements indicate the existence of short lived configurations of five quarks [2]. The baryons and mesons also contain a large number of virtual quarks (the sea quarks) and a number of gluons that binds the quarks together.

In the large momentum transfer regime (hard scattering processes) perturbation theory can be applied and perturbative QCD (pQCD) calculations show good agreement with data (see section 2.1 on hard processes and pQCD). However, in the small momentum transfer regime (soft processes) the perturbative approximation is not valid. In this regime, QCD calculations can still be performed by solving the QCD Lagrangian path integrals numerically on a discretized lattice in space-time – this is called lattice QCD (for a review, see ref. [3]). Even though the soft physics is dominating the observed processes, the hard physics still plays a role for the structure of hadronic matter. The hard processes can in principle be calculated in the lattice QCD framework, but in practice approximations are needed in order to achieve reasonable simplicity of the numerical algorithms and reasonable computation time. Therefore the results from QCD lattice calculations are still somewhat uncertain. Also, a non vanishing baryon chemical potential complicates the calculations and only recently is this domain being investigated [4].

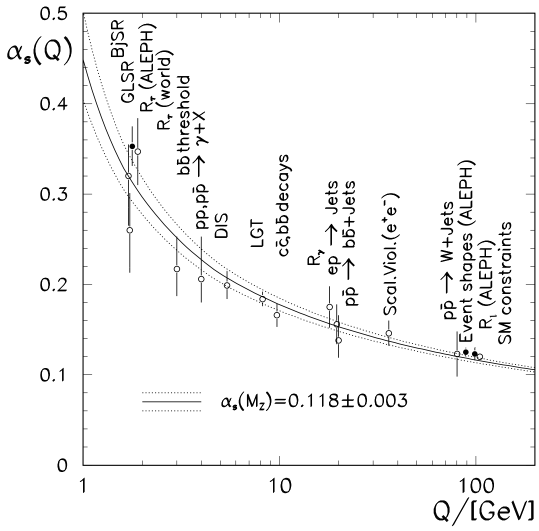

Figure 1.1: The strong coupling constant α_S as function of momentum transfer Q. The plot is from ref. [1]

One of the early successes of lattice QCD calculations was the prediction that quark matter under normal conditions (densities and temperatures like in an atomic nucleus) will have the known structure with the quarks confined in hadrons [5].

It should be noted, that lattice QCD calculations give the properties of static equilibrated systems and can therefore not model the dynamics of heavy ions collisions which evolve on short time scales.

1.1.2 The Quark Gluon Plasma

Before the quark model and QCD were formulated, an upper temperature limit of hadronic matter in the normal state was proposed. The arguments came from the observed rapid growth in the number of hadronic resonance states with temperature of the hadronic matter. The number of states indicated a divergent behavior with an upper temperature around $\sim 165\,\text{MeV}$ – this is known as the Hagedorn limit.

Lattice QCD confirmed this upper temperature limit of normal nuclear matter. The behavior of modeled thermodynamical quantities clearly shows the existence of a phase transition between hadron gas and quark gluon plasma. Figure 1.2 shows the energy density ϵ divided by the temperature T to the fourth power as a function of the fraction of the critical temperature. The quantity ϵ/T^4 is proportional to the number of thermodynamic degrees of freedom of the system. A dramatic increase is seen around the critical temperature where the phase changes: the relevant degrees of freedom are no longer hadronic but partonic. In the partonic environment, i.e. when the quarks are closely surrounded by many color charges, the quark–quark potential is screened. A similar effect is known in Quantum Electro Dynamics, the Debye screening of electrons in a high pressure crystal. The effective quark–quark potential becomes constant (flattens out) at some distance, which depends on the energy density. Figure 1.3 shows a lattice QCD study of this effect.

QCD also predicts the so called chiral symmetry restoration. As the energy density rises, the coupling between the quarks diminish. This has the consequence that the number of virtual quarks

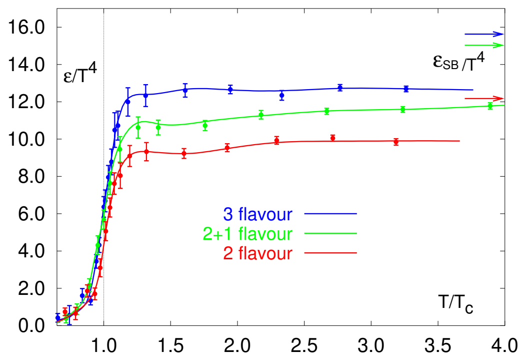

Figure 1.2: Lattice QCD calculations show that the number of thermodynamic degrees of freedom shows a drastic increase around the certain temperature (the critical temperature T_c). The plot is from ref. [6].

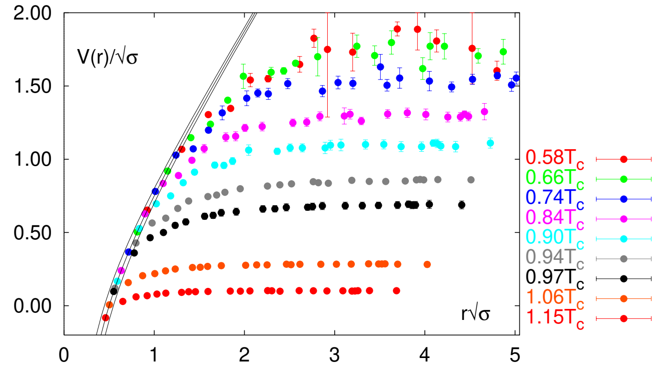

Figure 1.3: The effective quark quark potential as function of distance for different fractions of the critical temperatures (both axis are normalized by the string tension $\sqrt{\sigma}$). The two lowest curves are for temperatures above the critical. The plot is from ref. [6].

and gluons decreases (the quark condensate becomes less dense). In the limit, the light quarks lose their *constituent mass* and become (nearly) massless. In this limit (of no masses), the left– and righthanded quarks decouple leading to a degeneracy in states of opposite parity. The QCD Lagrangian now has the two symmetric terms describing the left– and right–handed quarks (the word *chiral* is greek and refers to the handedness of the particles). At low energy density, when the quarks are confined, the symmetry is broken and the hadrons require their non–degenerate masses.

A scenario where the quarks are deconfined but not yet massless could exist. The transition to a deconfined phase does therefore not a priori result in chiral symmetry restoration – it could require an even higher energy density to restore the symmetry.

1.2 High Energy Heavy Ion Collisions

High energy heavy ion collisions provide the opportunity to study the properties of hot and dense (nuclear) matter and thereby test and improve QCD. In the early stages of relativistic heavy ion collisions, many particles are created in a small region in space. One of the main goals of the experiments is to create a quark gluon plasma, to study the properties of this phase and to characterize the phase transition.

The observables are found in the final state of the particles that leaves the collision zone. These particles are measured long time after the *break up* of the collision zone and an understanding of the collision evolution can therefore only be obtained via models and theory.

Two major high energy heavy ion programs have produced vast amounts of data from different collision systems at center–of–mass energies $\sqrt{s_{NN}}$ from 2 GeV to 200 GeV. One at Brookhaven National Laboratory, where the Alernating Gradient Synchrotron (AGS), $\sqrt{s_{NN}} \approx 2-5$ GeV, and the Relativistic Heavy Ion Collider (RHIC), $\sqrt{s_{NN}} = 62.4 - 200$ GeV, are located. The other program is located at CERN, where the Super Proton Synchrotron (SPS), $\sqrt{s_{NN}} = 9-20$ GeV, is still operating and where the Large Hadron Collider (LHC), $\sqrt{s_{NN}} = 5.5$ TeV, is under construction. This thesis will focus on heavy ion physics in the RHIC energy regime – recent reviews of AGS and SPS physics can be found in ref. [7, 8].

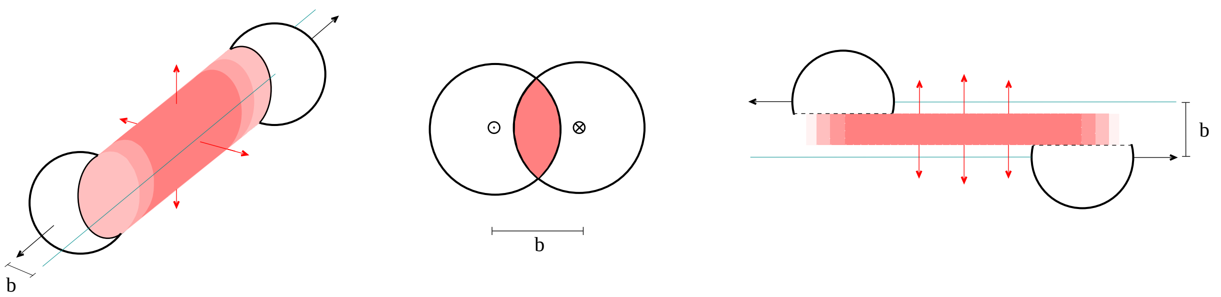

Figure 1.4: Schematic drawing of the geometry of a symmetric collision. The nuclei are depicted as *hard* spheres. The collisions is seen in perspective (left drawing), from the beam axis (middle drawing) and from the top (right drawing).

1.2.1 The Collision Geometry

Figure 1.4 shows a schematic drawing of a heavy ion collision at very high energy. The nucleons outside the overlap region (parallel to the beam axis) are called the spectators. After the collision, they move on with their initial momentum and fragment into smaller systems with little transverse momentum. The nucleons inside the overlap region are called the participants. The number of participants is related to the impact parameter, b, defined as the transverse distance between the centers of the colliding nuclei (see figure 1.4).

The reaction plane (or event plane) is defined as the plane spanned by the impact parameter vector and the beam axis. The azimuthal angle of this plane (in the coordinate system of the detector) is denoted Ψ. In figure 1.4, the orientation of the event plane is horizontal, which means that $\Psi = 0$.

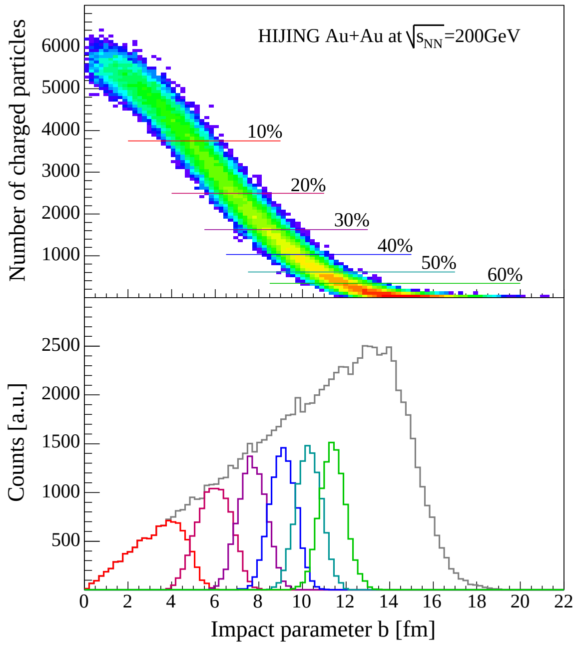

Figure 1.5: Upper panel: Total charged particle multiplicity versus impact parameter from the HIJING model. Lower panel: Impact parameter distributions for different centrality classes as selected from the charged particle multiplicity.

The impact parameter cannot be directly measured – instead an experimental quantity, the centrality c, is used. Typically, the measured charged particle multiplicity is used to define the centrality. Collisions that gives a charged particle multiplicity among the $N\%$ highest (of all inelastic collisions) have $c \leq N\%$. Normally, the data is presented in different centrality bins, for example $0-5\%$ or $20-40\%$. There will be fluctuations in the number of produced particles for collisions with a given impact parameter. This means that the impact parameter distribution for events of a given centrality will have a certain width. The challenge is to define the centrality (from measurable quantities), so that the width of the impact paramter distribution is minimized, i.e. so that the impact parameter distributions for the different centrality classes have as little overlap as possible. The relation between the impact parameter and the centrality can only be studied using models (where the impact parameter is known).

Figure 1.5 shows the total charged particle multiplicity as a function of the impact parameter for $Au + Au$ collisions at $\sqrt{s_{NN}} = 200\,\text{GeV}$ as given by the HIJING model [9]. The horizontal lines in the upper panel indicate different centralities and the lower panel shows the corresponding impact parameter distributions. It is clear, that for peripheral collisions, the centrality defined from the charged particle multiplicity gives large overlaps in the impact parameter distributions. When studying peripheral collisions, centrality can be defined from the correlation between charged particle multiplicity and the number of measured neutrons at very small angles (see section 4.1.2).

Two quantities, the number of participants N_{part} and the number of binary collisions N_{bin}, are often used instead of centrality (or as normalization parameters). The number of participants is simply the number of participating nucleons, i.e. the nucleons in the transverse overlap region of the two nuclei (see figure 1.4). The number of binary collisions is calculated by letting the two nuclei pass each other and, for each nucleon, count how many nucleons (from the other nuclei) it collides with. The number of binary collisions is the sum of all the nucleon–nucleon collisions. The number of participants and number of binary collisions are normally derived using the so called Glauber approach (see section 5.7).

1.2.2 The Collision Evolution

Figure 1.6 lists the different stages in the evolution of a central collision at RHIC energy – the observations related to the different stages are listed on the right.

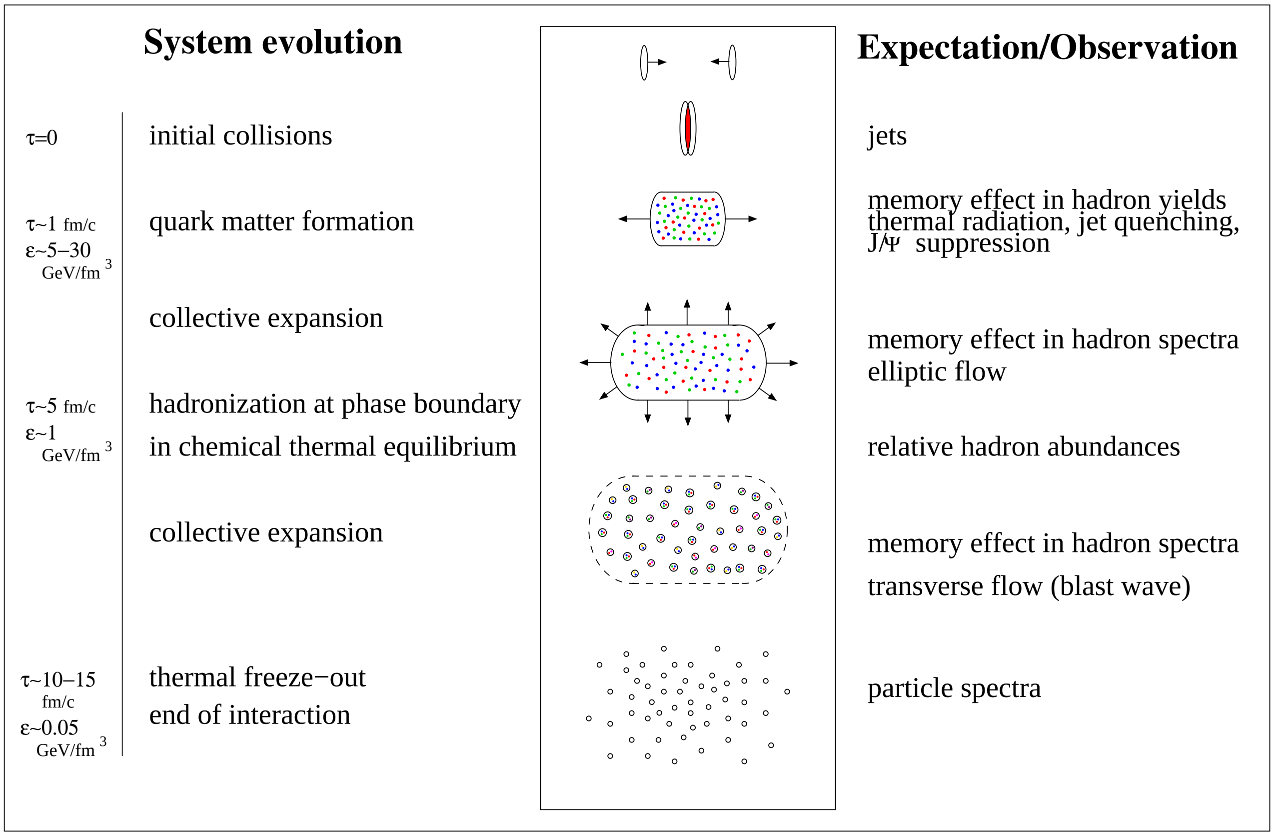

Figure 1.6: Schematic overview of the collision evolution at RHIC.

After the initial collision, a cylindrical zone of high energy density is built up between the fragments of the initial nuclei. Measurements of the elliptical flow indicate that shortly after the initial collisions ($t \lesssim 1\,\mathrm{fm/c}$) the partonic matter interacts strongly and is highly thermalized. The hot and dense zone expands and cools down. Around $t \sim 5\,\mathrm{fm/c}$ hadrons are created. The hadrons are either created in chemical equilibrium or they reach it quickly in the strongly interacting hadron gas. A large pressure gradient is built up and the hadron gas expands rapidly and cools. After an additional $\sim 6 - 10\,\mathrm{fm/c}$ the hadrons stop interacting elastically and the kinetic freeze out is reached. The particle spectra at the kinetic freeze out indicates local thermal equilibrium and a large radial expansion velocity. This picture of the collision evolution is supported by the measurements presented in the following sections.

1.3 Results from RHIC

In the following sections, some of the main results from the Au+Au runs at RHIC will be presented. The text will follow the time–line of the collision, starting with the charged particle multiplicity of the final state and then going back in time, from the shape of the particle spectra (linked to the kinetic freeze out) to measurements related to the initial conditions of the collision. The focus here will be on the bulk matter production. Measurements of the high p_T particle production, which is the main subject of this work, will be discussed in chapter 6. The results quoted in the following are for central $Au + Au$ collisions at $\sqrt{s_{NN}} = 200\,\mathrm{GeV}$, unless differently stated.

1.3.1 Charged Particle Multiplicity

The number of charged particles produced gives the first rough picture of the collision and it has ruled out a number of models proposed for the RHIC energy regime. In the experimental papers [10, 11, 12, 13] two main topics are in focus: The effect of gluon saturation/shadowing and the interplay between soft and hard collision processes.

Saturation and shadowing models explains the observed modification of the parton distribution function in a nucleon bound in a nucleus as compared to a free nucleon – the partons carrying a low fraction of the nucleon momentum x are depleted when the nucleon is bound in a nucleus. The measurements cannot distinguish between saturation models and models including standard parametrization of nuclear shadowing (see sections 2.3.2 and 2.3.3 for a description of shadowing and saturation). However, models with depletion of the low$-x$ partons seem to be more successful in reproducing the multiplicity.

The interplay between soft and hard processes has been investigated by parameterizing the centrality dependence of the charged particle pseudo–rapidity density around mid–rapidity, $dN_{ch}/d\eta = AN_{part} + BN_{coll}$. The first term describes the contribution from soft scattering production, which is expected to scale with the number of participants N_{part}. The necessity of a second term proportional to the number of binary collisions N_{bin} has been taken as a hint of the importance of hard scattering processes. The hard scattering term is (within errors) independent of the centrality and it is questionable how much such a parameterization actually reveals about the processes leading to particle production. Furthermore, the PHOBOS experiment has shown that the centrality dependence of the total charged particle multiplicity scales linearly with the number of participants [14] – the hard scattering term is only needed for describing the charged particle density in limited pseudo–rapidity regions. This suggests that the necessity of the second term is related to the redistribution of particles in the phase space rather than contribution from hard scattering.

1.3.2 Soft Spectra – Thermal Freeze Out

The shape of the transverse momentum spectra in the low p_T region ($< 2\,\mathrm{GeV/c}$) reflects the temperature and kinematics of the source of particles. According to statistical physics, energy of particles emitted from a thermalized source will follow a thermal distribution. In heavy ion collisions the spectra from the different particle species exhibit a different behavior: the shape (and in particular, the steepness) of the spectra has a strong dependence on the particle mass. This can be interpreted using the so–called blast wave models [15]. In these models, the collision zone is described as locally thermalized with a fast collective radial motion – the energy of the emitted particles is partly thermal energy and partly translational kinetic energy from the blast. The blast originates from the pressure built up by the frequent scattering in the original dense system.

The shape of particle spectra is modeled by "...integrating the partial differential equations of hydrodynamics over the reaction zone by assuming certain thermal and velocity profiles." [16]. The resulting functions are normally used to fit spectra of several different particle species simultaneously, which gives a temperature T_k and a flow velocity $\langle\beta\rangle$ at the kinetic freeze out. The agreement between the blast wave fits and the soft particle spectra is remarkable and holds over a large energy span. In central collisions $T_k \approx 100\,\mathrm{MeV}$ and $\langle\beta\rangle \approx 0.7c$ are extracted from such analyses [17, 18].

The blast wave fits have some difficulties describing spectra of the Ξ and Ω particles (simultaneously with the spectra of the particles of lower mass) – this can be explained by the weaker coupling of these particles as compared to the singly strange and non strange hadrons. "Assuming that the $\pi + Xi$ and $\pi + \Omega$ cross–sections are small, the blast wave fits suggest that flow has developed first within partonic matter, affecting all particles, and then within hadronic matter, affecting only particles with large hadronic cross–sections." [19].

1.3.3 Elliptic Flow – a Sign of Early Thermalization

Collective flow can also be studied by investigating the azimuthal anisotropy of the emitted particles relative to the reaction plane. It is quantified by the harmonic Fourier coefficients v_n in the azimuthal distribution of particles relative to the reaction plane.

$$\frac{d^3n}{p_T dp_T dy d\phi} = \frac{d^2n}{2\pi p_T dp_T dy}\left(1 + 2\Sigma_n v_n \cos(n(\phi - \Psi_{RP}))\right). \tag{1.1}$$

Ψ_{RP} is the azimuthal angle of the reaction plane and ϕ is the azimuthal angle of a single particle (with respect to the laboratory frame). The first harmonic v_1 measures the (asymmetric) flow of particles in the direction of the impact parameter vector (toward one of the colliding nuclei) – it is called direct flow. In a symmetric collision, the direct flow ($n = 1$) is zero at mid–rapidity, since the particles do not prefer the direction of one of the nuclei to the other – the size of v_1 typically becomes larger at forward or backward rapidities. The second harmonic v_2 describes the symmetric flow of particles both parallel and perpendicular to the impact parameter vector. A large v_2 is caused by an elliptic shape of the source and is therefore called the elliptic flow. It is typically the largest of the harmonic coefficients. The higher harmonics are discussed in ref. [21] and references therein.

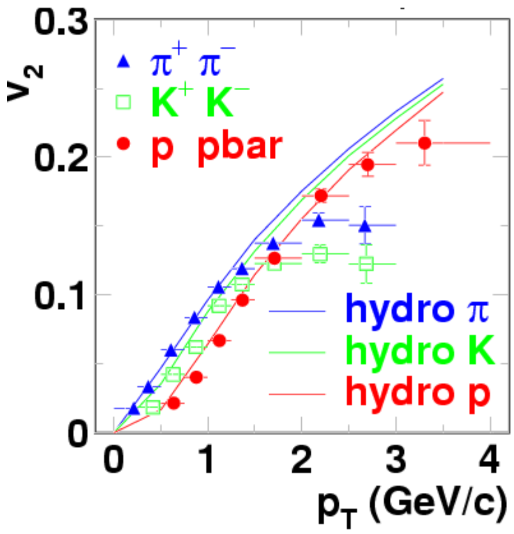

Figure 1.7: Elliptic flow parameter v_2 as function of p_T measured by PHENIX. The figure is from ref. [20].

How can an elliptic flow be interpreted? In ref. [22] it is stated that "Elliptic flow has its origin in the spatial anisotropy of the system when it is created in the non-central collision, and in particle re–scattering in the evolving system which convert the spatial anisotropy to momentum anisotropy. The spatial anisotropy in general decreases with system expansion, thus quenching this effect and making elliptic flow particularly sensitive to the early stages of the system evolution. Being dependent on re–scattering, elliptic flow is sensitive to the degree of thermalization of the system at this early time.". In other words, a large elliptic flow indicates frequent re–scattering and thereby a high degree of thermalization in the early stages of the collision. Hydrodynamical calculations which describe the system as a fully thermalized expanding gas, set the upper limit for elliptic flow.

Data from RHIC exhibit a large elliptic flow consistent with the predictions from hydrodynamics. Figure 1.7 shows measurements of the elliptic flow for identified particles as a function of p_T [20].

In ref. [23] Kolb and Heinz concludes from the RHIC data: "The data on elliptic flow can only be understood if thermalization of the early partonic system takes less than about 1 fm/c. At this early time, the energy density in the reaction zone is about an order of magnitude larger than the critical value for quark deconfinement, leading to the conclusion that a well–developed, thermalized quark-gluon plasma is created in these collisions which, according to hydrodynamics, lives for about 5 − 7 fm/c before is hadronizes.".

1.3.4 Particle Ratios – Chemical Freeze Out

The relative abundances of different particles are well reproduced by the statistical thermal model. The model [24, 25] describes the source as a hadron gas in thermal equilibrium. Bose–Einstein and Fermi statistics and a few conservation laws predict the relative yields of the different particles. The only free parameters are the chemical freeze out temperature T_{ch} and the baryo-chemical potential μ_b. In more peripheral collisions (and at lower energy) the model has some difficulties reproducing the relative yields and a strangeness suppression factor γ_s is added to take into account the lack of strangeness equilibration – in the central collisions at RHIC γ_s approaches 1, indicating a high degree of strangeness equilibration. The interpretation of the fits to the data is not straight forward since the model predicts the total (4π) yield from the grand–canonical ensemble, while most of the data are from a narrow region around mid–rapidity. Assuming that there is an independent source of particles at each rapidity and that redistribution of particles in the longitudinal direction is limited, the model is still meaningful. The statistical model has been applied to RHIC data in ref. [17, 26, 27]. It is found that the temperature at the chemical freeze out is ≈ 170 MeV, while the chemical potential (at mid–rapidity) is ≈ 25 MeV – this is on the border of the phase transition to the quark gluon plasma as predicted by lattice QCD calculations (see figure1.8).

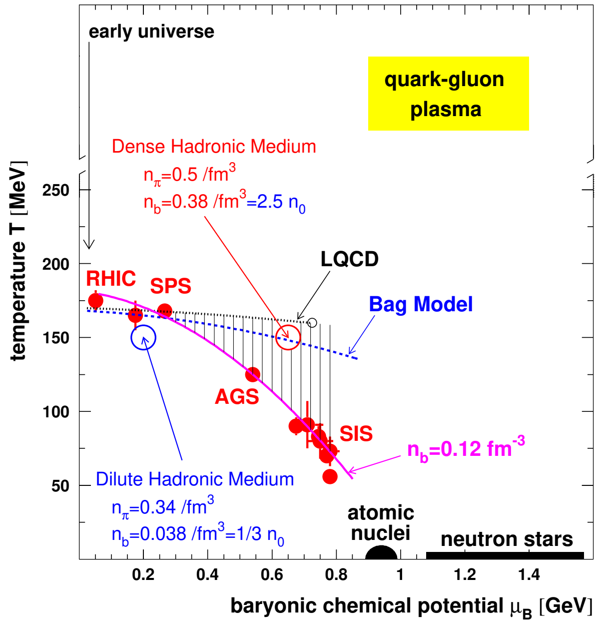

Figure 1.8: Chemical freeze-out temperature as function of the baryo-chemical potential extracted from a statistical model (figure from ref. [28]).

1.3.5 Net Proton Distribution – Baryon Stopping

The net-proton rapidity distribution $(dN(p)/dy - dN(\bar{p})/dy)$ shows that the mid–rapidity region has few net–baryons and most of the baryons from the beam are situated at rapidities around $2.5-5$ [29]. This observation shows that the collision scenario is very different from what was observed at lower energies, where most the baryons are situated around mid–rapidity (see figure 1.9). Such a collision scenario was predicted by Bjorken in 1983: "There exists a “leading-baryon” effect. That is, the net baryon number of the projectile is found in fragments of comparable momentum (more precisely within $\sim 2-3$ units of rapidity of the source).” [30]. The stopping is quantified by the average rapidity loss of baryons

$$\langle \delta y \rangle = y_b - \frac{2}{N_{part}} \int_0^{y_b} y \frac{dN_{net-b}(y)}{dy} dy, \tag{1.2}$$

where y_b is the rapidity of the beam and $dN_{net-b}(y)/dy$ is the net-baryon rapidity density. Note, that the measurements depicted in figure 1.9 show net–protons and not net–baryons. In order to estimate the net–baryons (and thereby the net–baryon rapitiy loss), the contribution from the other baryons must be estimated via models. At lower energies it was found that the stopping is proportional to the beam rapidity [31].

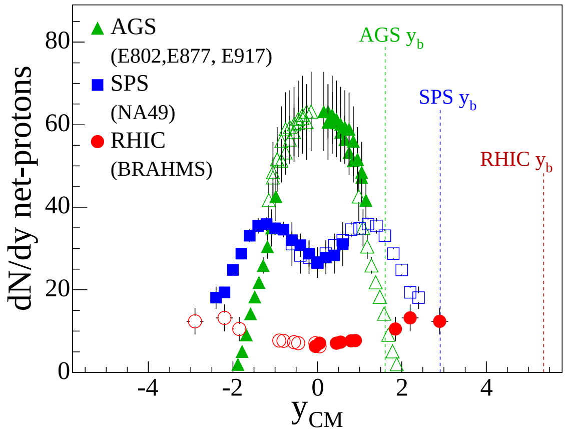

Figure 1.9: Net-proton rapidity densities for central heavy ion collisions ($Au+Au$ or $Pb+Pb$) at different energies.

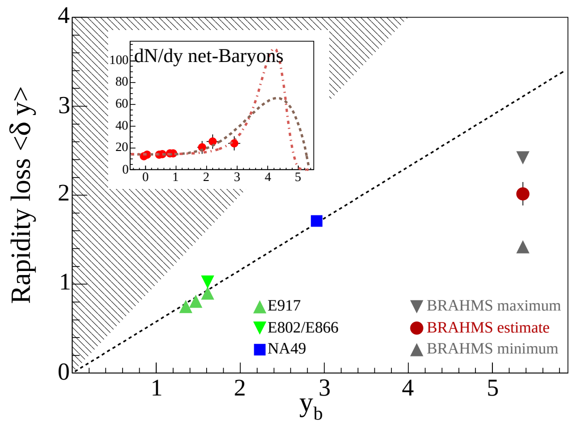

Figure 1.10: Stopping (average rapidity loss of baryons) as function of beam rapidity.

At RHIC this simple proportionality is clearly broken (see figure 1.10) – in fact, the stopping is not much higher than at SPS and it therefore seems likely that the stopping *saturates* and becomes independent of the beam energy. The stopping is related to the amount of kinetic energy of the initial nuclei that is converted to particle production and excitation of the collision zone. The total energy loss of baryons in the top 5% central $Au + Au$ collisions is estimated to be approximately 25 TeV [29].

1.3.6 Initial Energy Density – The Bjorken Prescription

In the previous section, it was described how the transparency of collisions at RHIC resembles the scenario proposed by Bjorken. Another assumption in this model is *boost invariance* at rapidities near $y = 0$, which means that the abundances of particles (dN/dy) is independent of y. This seems to be the case at RHIC in at least one unit of rapidity ($|y| < 0.5$). Based on his collision picture (transparency, boost invariance and hydrodynamical evolution of the source) Bjorken gives a formula for the energy density ϵ_{Bj} in the early stages of the collision. He looks at a thin slab of matter at mid–rapidity. The energy density is calculated from estimations of the energy in a thin slab of matter. Since the source is boost invariant, the energy flow in the longitudinal direction can be disregarded and the energy is estimated from the mean transverse energy ($\langle E_T \rangle \approx \langle m_T \rangle \cosh(y)$) times the number of particles (dN). The volume of the slab is the transverse area (πR^2) times the length (Δz), which is estimated from the expansion time τ_0 and the longitudinal expansion velocity. From the relation $z = \tau_0 \gamma \beta = \tau_0 \sinh(y)$, the length of the slab can be calculated $\Delta z = \tau_0 \cosh(y) \Delta y$. The energy density can now be written:

$$\epsilon_{Bj} = \frac{\langle E \rangle}{V} = \frac{\langle m_T \rangle \cosh y \frac{dN}{dy} \Delta y}{\pi R^2 \tau_0 \cosh y \Delta y} = \frac{\langle m_T \rangle}{\pi R^2 \tau_0} \frac{dN}{dy} \tag{1.3}$$

The expansion time τ_0 is set to the estimated time it takes to create the particles (the formation time). At RHIC it is generally estimated to be on the order of 0.3 fm/c [32], while a conservative upper limit of 1 fm/c is often used. In central Au+Au collisions ($R \approx 6$ fm) at $\sqrt{s_{NN}} = 200$ GeV the mean transverse mass is found to be ≈ 0.6 GeV and the rapidity density is ≈ 950. Using the conservative estimate of $\tau_0 = 1$ fm/c, equation 1.3 gives $\epsilon_{Bj} \approx 5\,\mathrm{GeV/fm^3}$ [33]. This is 5 times higher than the critical energy density as determined from QCD lattice calculations [34].

1.3.7 Conclusions from RHIC

The previous sections listed a number of measurements that give a comprehensive picture of heavy ion collisions at the RHIC energy. The conclusions are:

- The energy density built up in the early stages of the collisions is well above the expected critical energy density for the creation of deconfined matter.

- The collision scenario is very different from that observed at lower energies. The two nuclei interpenetrate and the collision zone is built up between them. The central part of the collision zone is almost depleted of net-baryons – which is consistent with the low baryo-chemical potential extracted from statistical analysis of the particle ratios at mid–rapidity.

- The relative abundances of particles are well described by thermal statistical models that give temperature and baryo-chemical potential on the border of the phase transition between hadron gas and quark gluon plasma. This observation does not say anything about whether the particles are created in hadronization from a QGP or if they simply are created in this equilibrium.

- The large elliptical flow indicate a high degree of thermalization in the early stages of the collision. The measurements in the low p_T region ($< 1.5 - 2$ GeV/c) are consistent with hydrodynamical models that set the upper limit for the azimuthal anisotropy. This indicates a high degree of thermalization at an early time $t \lesssim 1$ fm/c.

- The shape of the transverse spectra indicate that the particles are in local thermal equilibrium, but also exhibit a large collective motion in the transverse direction. The difference in temperature from the chemical to the kinetic freeze out indicate a time scale of at least $\Delta t \approx 6$ fm/c [17].

The observations related to the different stages of the collision give a comprehensive and consistent picture of the collision evolution. The bulk matter properties are well described and understood in terms of different models, e.g. hydrodynamical, thermal statistical and blast wave. Here, the bulk matter production have been in focus. Other observables that can reveal properties of the dense medium created in the early stages of the collisions are the thermal photons, the J/Ψ meson and the high p_T hadrons. The latter is discussed in chapters 2, 6 and 7.

Chapter 2

High p_T Particle Production

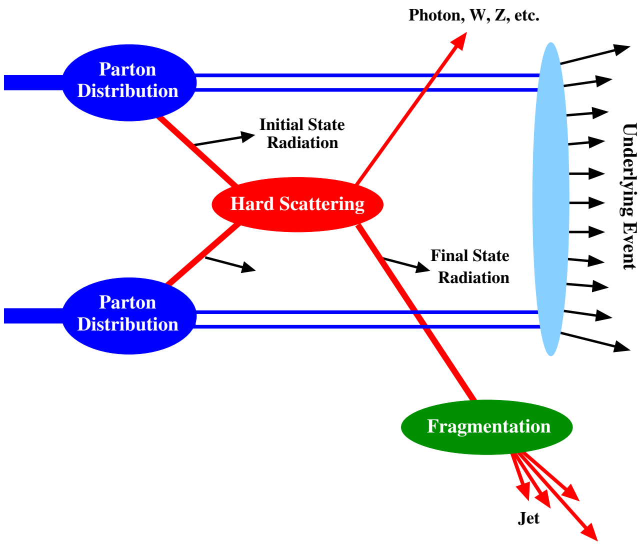

Figure 2.1: Schematic view of a hard scattering in a heavy ion collision.

High p_T particles[1] are produced in processes with large momentum transfer Q – called hard processes. In nucleon-nucleon collisions these processes are relatively well understood and pQCD calculations have been successful in describing the data over a large span of energies [35]. In nucleus–nucleus collisions, the high p_T particles are also expected to be produced in hard processes (in the collisions between the particles inside the nucleus). Modeling the yields of high p_T particles in nucleus–nucleus collisions is however more difficult, since a number of different nuclear effects can alter the production mechanisms: modifications of the parton distribution functions, multiple scattering in the initial state, energy loss of the produced high energy particles in the medium and modifications to the fragmentation processes. These nuclear effects (or modifications) are often divided into initial and final state effects, i.e. processes before and after the hard scattering. This separation is not well defined in all cases, since a parton could undergo two (or more) semi–hard scattering and result in high p_T particle production.

The nuclear effects can be studied by comparing the yields from nucleon–nucleon collisions and the yields from nucleus–nucleus collisions. Such comparisons with varying collision systems and collision energies can help to disentangle and understand the different nuclear effects. In particular, the energy loss of high energy particles is of great interest, since it is sensitive to the properties of the traversed medium. Also, the modification of the parton distribution functions has been in focus, since it may be related to the proposed new kind of matter, the Color Glass Condensate.

The purposes of this chapter are to describe the pQCD baseline for modeling high p_T particle production, to present how the comparison between yields from nucleon–nucleon and nucleus–nucleus collisions are done and to give brief intuitive descriptions of the different effects that may modify the high p_T particle production. In the last part of the chapter, the nuclear effects are illustrated with more detailed descriptions of a few specific models. The focus is on the production of charged (unidentified) hadrons, since this is the subject of the experimental work presented later in this thesis.

[1]Typically, the limit between high and low (or hard and soft) is around 2 GeV/c.

2.1 Jet Production

In nucleon–nucleon interactions high p_T particles are emitted in jets. These jets are typically produced in pairs and the process is interpreted as elastic scattering of two partons. The elastic scattering *knocks out* the two partons from their respective nucleons. The two partons fragment into hadrons that are emitted back–to–back in two narrow cones, i.e. the jets. Due to momentum conservation the jets exhibit a strong azimuthal correlation. It has also been observed that a typical jet has one hadron that carries much more energy than the rest, around 20% of the total jet energy – this is called the leading hadron. A hard scattering process is illustrated in figure 2.2.

The cross sections for high p_T particle production in elementary collisions can be calculated using factorization [36], which implies that the elastic scattering and the fragmentation can be treated as independent processes. The elastic parton–parton cross section and the (subsequent) fragmentation is represented by two independent functions.

The invariant differential cross section for $p + p \to h + X$ is often calculated from the following equation:

$$E_h \frac{d\sigma_h^{pp}}{d^3p} = K \sum_{abcd} \int dx_a dx_b \int d^2k_a d^2k_b g(k_T^a) g(k_T^b) f_{a/p}(x_a, Q_a^2) f_{b/p}(x_b, Q_b^2) \times \frac{d\sigma^{ab\to cd}}{d\hat{t}} \frac{D_{h/c}(z_c, Q_c^2)}{\pi z_c}, \tag{2.1}$$

where a, b denote the partons before the hard scattering and c and d denote the partons after, $x_a = p_a/P_A$ and $x_b = p_b/P_B$ are the initial momentum fractions of the interacting partons, $\hat{t}$ is a Mandelstam variable (see [35] for details), $z_c = p_h/p_c$ is the momentum fraction of the final state hadron, f is the parton distribution function, $\sigma^{ab\to cd}$ is the cross section calculated from leading order pQCD and $D_{h/c}(z_c, Q_c^2)$ is the fragmentation function. The parton distribution and fragmentation functions are parameterized from fits to measurements of reference processes, for example deep inelastic lepton scattering or annihilation.

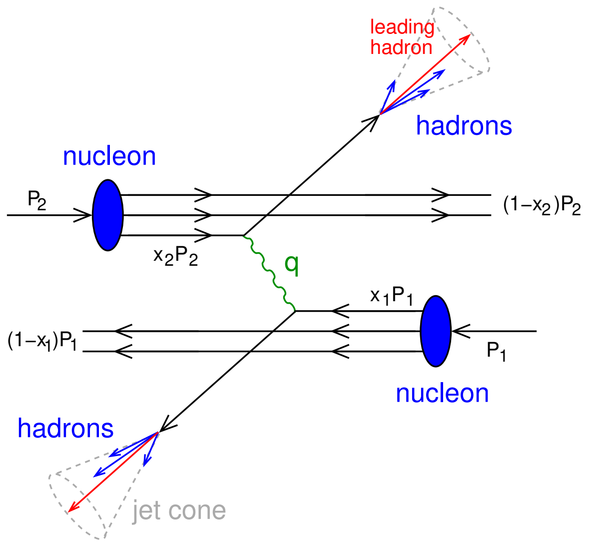

Figure 2.2: Schematic drawing of a parton–parton scattering in the parton model. The two partons are *knocked out* from the nucleons.

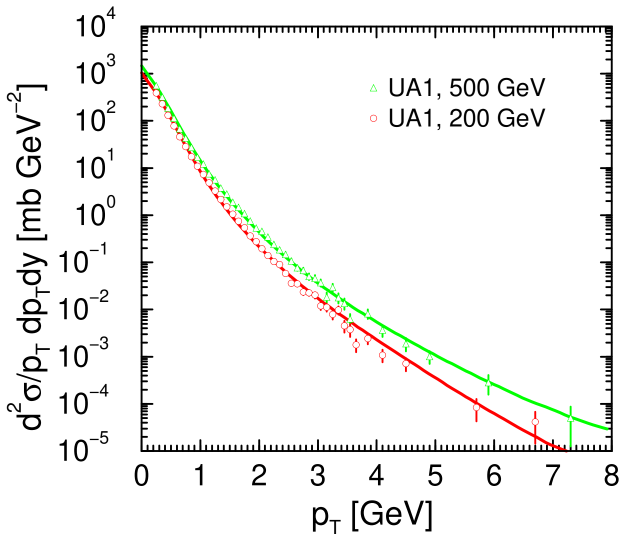

Figure 2.3: Comparison of UA1 data ($p + \bar{p}$) and leading order pQCD calculation. The figure is from ref. [37].

The leading order pQCD calculation of the cross section and the standard parameterizations of the parton distribution and fragmentation functions give too low cross sections for hadron production in $p + p$ collisions. This is often corrected for by introducing a phenomenological K factor and a Gaussian broadening ($g(k_T)$) of the intrinsic parton transverse momentum distribution. The K factor correction takes into account the higher order terms in the pQCD calculations of the cross sections. Figure 2.3 shows the good agreement between hadron yields from $p + \bar{p}$ collisions and leading order pQCD calculation. Using next–to–leading order pQCD calculations gives better agreement with the data and in this case the K factor is not needed. However, the models describing high p_T particle production in heavy ion physics typically use the leading order calculations and the phenomenological K factor. For a detailed description of pQCD calculation of the high p_T particle production in $p+p$ collisions, see ref. [35].

The p_T spectra obtained from pQCD calculations (and the measurements) have the shape of a power–law distribution (see appendix B). Therefore, the data is often fitted by a (pQCD inspired) power–law function.

2.2 The Nuclear Modification Factor

In nucleus–nucleus collisions, the interactions leading to production of high p_T particles are the hard scatterings of partons inside the nucleons of the nucleus. In a hard scattering, the momentum transfer Q is high and, by the uncertainty principle, the collision (or formation) time is small. These collisions could therefore be expected to be incoherent. The high p_T yields should in this case scale with the number of (binary) collisions N_{bin}. This has led to the definition of the nuclear modification factor R_{AB}, which quantifies the deviation in yields from $A + B$ collisions relative to the scaled yields from nucleon-nucleon ($N + N$) collisions:

$$R_{AB} = \frac{d^2 N^{AB}/dp_T d\eta}{\langle N_{bin}^{AB}\rangle d^2 N_{inel}^{NN}/dp_T d\eta}. \tag{2.2}$$

Traditionally the yields from elementary collisions have been expressed in terms of the cross section σ_{inel}^{NN}. The denominator in equation 2.2 then reads $T_{AB} d^2\sigma_{inel}^{NN}/dp_T d\eta$, where $T_{AB} = \langle N_{bin}\rangle/\sigma_{inel}^{NN}$ is the nuclear overlap function which can be calculated from Glauber calculations (see section 5.7).

Construction of the nuclear modification factor R_{AB} requires a p_T spectrum from elementary collisions ($N + N$) at the same energy. Since this is not always available, comparison between central and more peripheral collisions is often used instead. As the collisions become more peripheral, the nuclear effects are expected to play a relatively small role and the yields from peripheral collisions substitute the yields from elementary collisions in equation 2.2. However, quantitative evaluation of the nuclear modifications becomes complicated, since the modifications in peripheral collisions cannot be neglected. Comparison between central and more peripheral collisions is quantified by

$$R_{CP} = \frac{\langle N_{bin}^{P}\rangle\, d^2 N^{C}/dp_T d\eta}{\langle N_{bin}^{C}\rangle\, d^2 N^{P}/dp_T d\eta}, \tag{2.3}$$

where the C and P denotes central and peripheral collisions respectively.

Interpretation of data normalized by the number of binary collisions should be done with caution. First, $\langle N_{bin}\rangle$ is not an observed quantity, it is model dependent and somewhat uncertain. Second, it is implicitly assumed that the collisions in the interior and on the back face of the nucleus are nucleon–nucleon collisions similar to the first collision on the front face of the nucleus (here assuming that the collisions are incoherent). This can obviously not be the case, since a nucleon must be excited and lose energy (or have disintegrated) after the first collision. The term *number of binary collisions* should therefore not be taken literally.

2.3 Nuclear Modifications

In the following, the *standard* nuclear effects will be described. The division into four sections (effects) is not completely logical – the Cronin enhancement is not an effect, but an observation explained by different effects. Moreover, the effects covered by the words shadowing and saturation are (in the normal interpretation) not exclusive. The idea is to give a brief intuitive description of the different effects and illustrate the inconclusive state of the field.

2.3.1 Cronin Enhancement

In the mid 70's it was observed that the particle production in p–nucleus collisions was enhanced at moderately high p_T compared to the expectation from elementary collisions. The observation was first made by Cronin *et al.* [38], hence the name Cronin enhancement. The process is often attributed to multiple scattering of particles in the initial state, but recently other theoretical explanations have been developed for the Cronin enhancement in high energy collisions.

Multiple Scattering

The basic idea is that the intrinsic k_T distribution of the partons in the nucleon (represented by the $g(k_T)$ terms in equation 2.1) is broadened by scattering as the projectile traverses the nuclear medium. The broadening will result in (slightly) lower production rates at low p_T and in an enhancement at moderately high p_T. The scattering is modeled both as scattering of the nucleon as a whole and scattering of the individual partons before the hard scattering. Recent $e+A$ data from the HERMES experiment [39] indicate that scattering in the final state could also contribute to the enhancement. A short review of multiple scattering description of the Cronin enhancement is given in [40].

How should the Cronin enhancement (explained by multiple scattering) evolve with the collision energy? Wang reflects on this in ref. [41]: "At low energies, the differential cross section for a single hard scattering decreases very fast with p_T (large power). It is then easier for the incident parton to acquire a large p_T through two successive scatterings, each with a small transverse momentum transfer, than through a single large p_T scattering. This is why multiple scattering in pA collisions cause the enhancement of large p_T parton production. As the energy increases, the differential cross section for a single scattering decreases less rapidly with p_T as compared to low energies. It is no longer more economical to produce a large p_T parton through double scattering than through single scattering. At extremely high energies, the Cronin effect will disappear.". Broadening of the k_T distributions is therefore not included in the HIJING model (see section 2.4.1). However, in a later papers, e.g. ref. [42], Wang introduces a parametrization of the k_T broadening that gives a Cronin enhancement at RHIC energies.

What are the consequences of multiple scattering at higher pseudo–rapidities? Answers to this question in the literature are sparse. In ref. [43] the pseudo–rapidity dependence of the nuclear modification is calculated using standard pQCD calculations. Here the phenomenological parameters defining the broadening are determined from SPS data and are assumed not to vary with the pseudo–rapidity, and the resulting nuclear modification factors at the different pseudo–rapidities are also quite similar.

Parton Recombination

Recent quark recombination (or coalescence) models have been able to reproduce the observed Cronin enhancement in $d+Au$ collisions at RHIC [44]. The particle production at moderate to high p_T ($2-8\,\mathrm{GeV/c}$) can be modeled by recombination of partons from different sources. In the high multiplicity and high temperature environment created in the collisions, a non–negligible fraction of the moderate p_T partons originate from the thermal component. The model evaluates the coalescence of partons, both from jets and from the thermal component, which gives the measured p_T behavior (Cronin enhancement) observed at RHIC. The approach leads to a slowly decreasing Cronin enhancement as p_T increases toward the very high p_T region. At forward rapidities, the thermal component dies out faster, and high p_T particles are also less abundant. This means that Cronin peak should be strongly reduced at forward rapidities.

2.3.2 Nuclear Shadowing

The observed depletion of low$-x$ partons in a nucleon inside a nucleus as compared to a free nucleon [45] is termed shadowing. The effect was first observed in deep inelastic scattering (DIS) by the European Muon Collaboration (EMC) experiment [46]. The depletion is normally shown as the ratio between the parton structure functions of a bound and a free nucleon. Figure 2.4 shows measurements of the modification of the parton structure function over the full x range.

The modification is typically modeled by a parametrization of the parton distribution function (PDF) ratios in terms of shadowing functions (that includes an enhancement in the anti-shadowing region) and it is assumed that the gluon modification (which is not measured) is similar to the quark modification. The parameterizations are constrained by the DIS data and evolved using the DGLAP[2] equations [48, 49, 50].

What causes the modification? Close to $x = 1$ the ratio shows a strong enhancement which can be explained by Fermi motion of the nucleons in the nucleus [45].

In the lower $x-$regions, the depletion is investigated using two different formalisms. One describes the phenomenon in the rest frame of the nucleus – here shadowing is explained by (coherent) multiple scattering. The other approach describes the phenomenon in a frame where the nucleus is moving fast – here, the depletion is a consequence of gluon recombination [51].

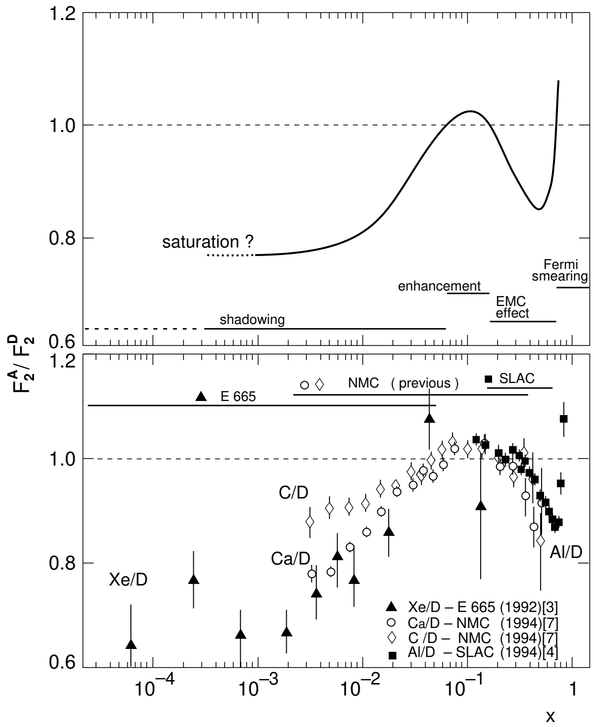

Figure 2.4: Top panel: Schematic drawing of the ratio of the parton structure function in a large nucleus compared to deuteron. The different effects in the different x-ranges are indicated (note that the Q^2 regions covered are different for the different x regions). Bottom panel. Corresponding measurements. The plot is from ref. [47].

In the multiple scattering picture, the "coherence length of the probe (the $q\bar{q}-$pair in DIS) $l_c \sim 1/(2m_N x)$ exceeds the intra–nuclear longitudinal distance between any two nucleons in the nucleus. The parton distribution is not merely the sum of nucleon parton distributions but also contains the interference between the parton distributions of the nucleons. When the coherence length is larger than the nuclear diameter [...] the $q\bar{q}-$pair interacts coherently with the entire nucleus, and the collective effects are expected to be important." [51].

The other approach considers the parton distribution in the swiftly moving nucleus. The number of virtual gluons seen by the probe is large (because of the high energy or low$-x$) and the gloun wave functions overlap. This causes gluon recombination (or gluon fusion), which depletes the parton distribution function at low$-x$. If the energy is high enough (or the x is low enough), the nucleus appears saturated with gluons. The saturation sets in below a certain momentum transfer, the so called saturation scale. Saturation is described in more details in the following section.

Both the coherent multiple scattering and the saturation approach lead to a slight enhancement (anti–shadowing) in the parton distribution function ratio at higher x. This is a consequence of momentum conservation: the sum of the momentum fractions (the x from the different partons) must add up to the total nucleon momentum. It has been shown that the multiple scattering approach and the saturation approach are mathematically equivalent in some kinematic regions [52]. The differences between the (multiple scattering) shadowing and the saturation formalism are discussed

[2]DGLAP is an acronym for the physicists that developed the equations: Dokshitzer, Gribov, Lipatov, Altarelli and Parisi.

in more detail in ref. [53] and [51].

2.3.3 Saturation

From the uncertainty principle the transverse area occupied by a particle is of the order of $\sim \pi/Q^2$, where Q is the transverse momentum [54]. The parton can be probed with the cross section $\sigma \sim \alpha_s(Q^2)\pi/Q^2$ (see figure 2.5). In a swiftly moving nucleus (with radius R_A and atomic number A), the sum of the partons transverse areas is larger than the transverse area of the nucleus πR_A^2 when the number of partons exceeds

$$N_A \sim \frac{1}{\alpha_s(Q^2)} Q^2 R_A^2. \tag{2.4}$$

An overlap will result in parton-parton interaction (e.g. gluon recombination or fusion), which will prevent further growth of the parton density. For a given momentum transfer the gluon density grows rapidly as $x \to 0$ and saturation consequently occurs when x is low enough. Conversely, for a given x, saturation sets in for transverse momenta below some critical value, the saturation scale

$$Q_S^2 \sim \frac{A^{1/3}}{x^\lambda} \tag{2.5}$$

where λ is an empirical parameter ($\lambda \approx 0.3$). Since the p_T of a produced particle scales with the momentum transfer of the hard scattering, saturation affects particle production below a certain p_T. Relevant for the high p_T study is of course the size of this saturation scale. In central $Au + Au$ collisions at RHIC energy the saturation scale is estimated to be $1 - 2\,\mathrm{GeV/c}$ at mid–rapidity [51], which is too small to affect the high p_T region.

How does the saturation scale change with rapidity? The rapidity difference between the produced hadron and the incoming parton can be written $y_h - y_p = \ln(1/x)$ [51]. The saturation scale therefore grows with difference in rapidity as $Q_S^2 \propto e^{\lambda(y_h - y_p)}$. The saturation effects in a nucleus should therefore be largest for hadrons emitted at rapidities opposite to that of the nucleus. In symmetric collisions (like $Au + Au$) it is difficult to measure this, since it is only the saturation (low$-x$ parton distribution) in one of the nuclei that can be probed. In asymmetric collisions, like $d + Au$, the saturation effects should be easier to investigate (close to the rapidity of the deuteron) since it sets in at lower momentum transfer and is stronger in the Au nucleus than in the deuteron. Figure 2.6 shows a toy model prediction of the nuclear modification factor as function of momentum k divided by the (mid–rapidity) saturation scale for $p + Au$ collisions [55]. The highest curve shows the mid–rapidity prediction at RHIC energy. The lower (solid) curve is the prediction for very high collision energies or high rapidity (in the direction of the proton). The two dashed curves show interpolation to intermediate collision energies.

The idea of saturation is formulated in an effective QCD theory that describes the low x partons as a coherent state of matter, called the Color Glass Condensate (CGC). A brief description of the theory is found in section 2.5.

2.3.4 Jet Quenching

Energetic particles traversing a dense medium lose energy via elastic scattering (collisional energy loss) and radiation of gluons (radiative energy loss). The energy loss via gluon radiation is much higher in a medium than in the QCD vacuum. In the dense medium created in heavy ion collisions, jets can therefore be partially or completely absorbed, hence the name jet quenching. The quenching results in a suppression of the high p_T particle yield as compared to the binary scaled yields from nucleon–nucleon collisions (where jet–quenching cannot occur).

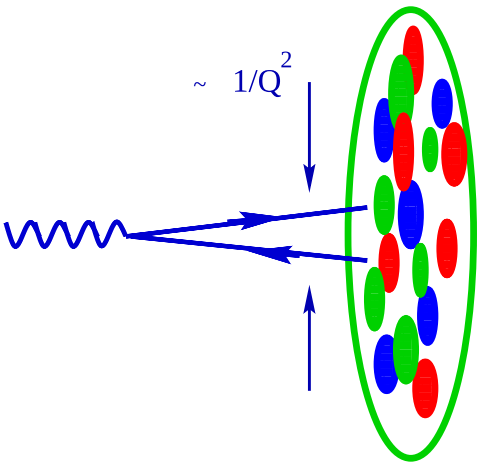

Figure 2.5: Hard probe interaction with a high energy nucleus. The incoming virtual photon splits into a $q\bar{q}$–pair that probes a transverse area $\sim 1/Q^2$. The figure is from ref. [54]

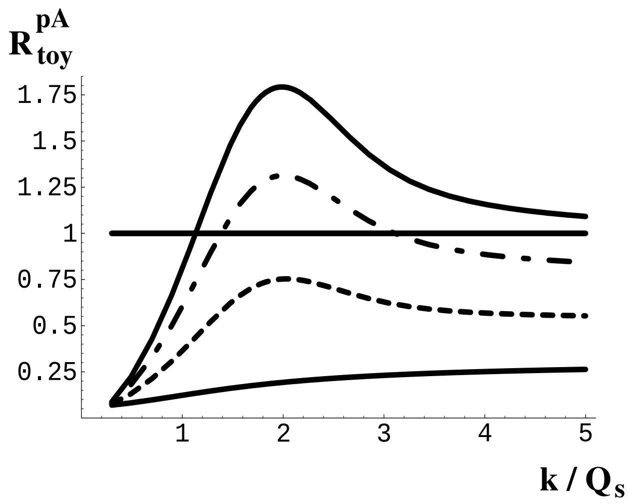

Figure 2.6: Toy model prediction of the nuclear modification factor as function of momentum in fractions of the mid–rapidity saturation momentum [55]. The upper curve shows a mid–rapidity prediction for $p+Au$ collisions at RHIC energy. The lower curves correspond to higher energies or higher rapidities.

The detailed pattern of the energy loss depends on the properties of the energetic particle and of the traversed medium – this *jet tomography* is a complicated theoretical problem (for a review see ref. [56]). The obvious questions relevant for the work presented later in this thesis are: How does the high p_T suppression depend on the properties of the medium? Can a strong suppression of the high p_T yields be explained by energy loss of partons or hadrons in a hadronic medium?

The first studies of energy loss focused on collisional energy loss via elastic re–scattering. It was shown that even in a hot ($T \sim 200\,\text{MeV}$) QCD plasma the energy loss was too small ($dE/dx \approx 0.5\,\text{GeV/fm}$) to extinguish jets [57].

Energy loss via photon radiation due to multiple scattering in a medium containing electrical charges was first studied by Landau, Pomeranchuk and Migdal (LPM) [58, 59]. A similar effect is seen in a colored medium, where multiple scattering between colored particles leads to gluon radiation (radiative energy loss). In a QCD medium with temperatures around 200 MeV the radiative energy loss dominated over collisional energy loss due to elastic scattering [57] and that it is clearly sufficient to extinguish jets. Theoretical studies have shown that the radiative energy loss in a static medium scales with the path length squared $\Delta E \propto L^2$ [57].

The detailed calculations of the energy loss depend on the coherence length (related to the formation time of the emitted gluons), the gluon mean free path in the medium and a transport coefficient (related to the typical momentum transfer in the inelastic collisions and the mean free path). The calculations become even more complicated when the expansion of the medium is taken into account. Theoretical studies show that the energy loss relates to the gluon density integrated over the path length L of the parton in the medium [56, 60]. This gives the possibility to relate the observed high p_T suppression to the density of the medium.

To answer the second question (can a strong suppression of the high p_T yields be explained by energy loss of partons or hadrons in a hadronic medium?), the formation time of the hard parton/hadron has to be evaluated. In ref. [61] Wang estimates the formation time of a 10 GeV pion to be 35 – 70 fm/c. This has to be compared to the estimated lifetime of the source. Wang argues that even though these numbers are "order–of–magnitude estimations, they are still much longer than the typical size or lifetime of the dense medium in heavy–ion collisions at RHIC.". This means that the energy loss of hadrons can only come from the late stage of the collision, i.e. it is energy loss of partons in the dense medium that gives suppression at high p_T. Can the dense medium traversed by the parton then be hadronic? Since the energy loss scales with the gluon density (related to the energy density) of the medium, it can provide information on the density of the medium. The high p_T suppression pattern cannot directly determine the phase of the medium. Only indirectly, via the estimated energy density, the suppression pattern is able to indicate whether the dense medium is deconfined or in the hadronic phase.

2.3.5 Remarks

How can the different nuclear effects be disentangled?

A strong suppression of the high p_T yields in central Au+Au collisions at $\sqrt{s_{NN}} = 130$ and $200\,\mathrm{GeV}$ was the first interesting high p_T observation at RHIC. This led to a discussion on whether the suppression was due to initial state shadowing or saturation effects or due to final state energy loss effects (jet quenching). The $d + Au$ run at $\sqrt{s_{NN}} = 200\,\mathrm{GeV}$ settled this issue – a significant enhancement at $p_T \approx 2 - 10\,\mathrm{GeV/c}$ was observed, which ruled out the initial state effects as explanation for the observed suppression in the $Au + Au$ collisions. If the suppression in the $Au + Au$ collisions was due to modification of the parton wave–functions in the Au nucleus, a similar modification would be present in the Au nucleus of the $d + Au$ collision.

The jet quenching effect in the $Au + Au$ collisions at RHIC has (roughly) been disentangled from the other effects by the *null* experiment – the $d + Au$ collisions. However, detailed descriptions of the different nuclear effects are still missing. The standard explanation of the Cronin enhancement is based on purely phenomenological extrapolations, the theoretical connection between shadowing and saturation is not fully developed [51], the lack of low$-x$ data leaves validity of the saturation theories unsettled and the description of the energy loss in a dense QCD medium is still somewhat uncertain. The first years of RHIC running have improved the knowledge about the nuclear effects significantly. To get an even better understanding of the RHIC high p_T data more detailed measurements and more theoretical work is needed.

What can be concluded about the medium created in the central $Au + Au$ collisions from the present understanding of the jet quenching effect? From the estimation of the hadron formation time, it can be concluded that the suppression primarily stems from radiative energy loss of the hard partons in the medium. The strength of the suppression indicates densities in the initial stages of the central $Au + Au$ collisions of $12 - 20\,\mathrm{GeV/fm^3}$ [56], which is about 100 times higher than the normal nuclear matter density. Within the current understanding of QCD, a strongly interacting medium with this energy density cannot be in a hadronic phase. Also, models including re–scattering and absorption in a hadronic medium have not been able to reproduce the observed suppression (see section 2.4.3).

The following sections describe a few of the commonly cited models in the field.

2.4 Models

2.4.1 Shadowing and Jet Quenching in HIJING

Wang and Gyulassy's microscopic model, HIJING [9, 62], merges string phenomenology and pQCD based calculations to describe the particle production in $p + p$, $p + A$ and $A + A$ collisions at high energy. String phenomenology has successfully described the global properties of particle production at AGS and SPS energies. At higher energies, hard and semi-hard processes (calculable from pQCD) become more important and must be taken into account to describe particle production. A detailed description of how the model merges these two approaches can be found in ref. [41].

Two nuclear effects, nuclear shadowing and jet quenching, were introduced in the model shortly after the first publication [63].

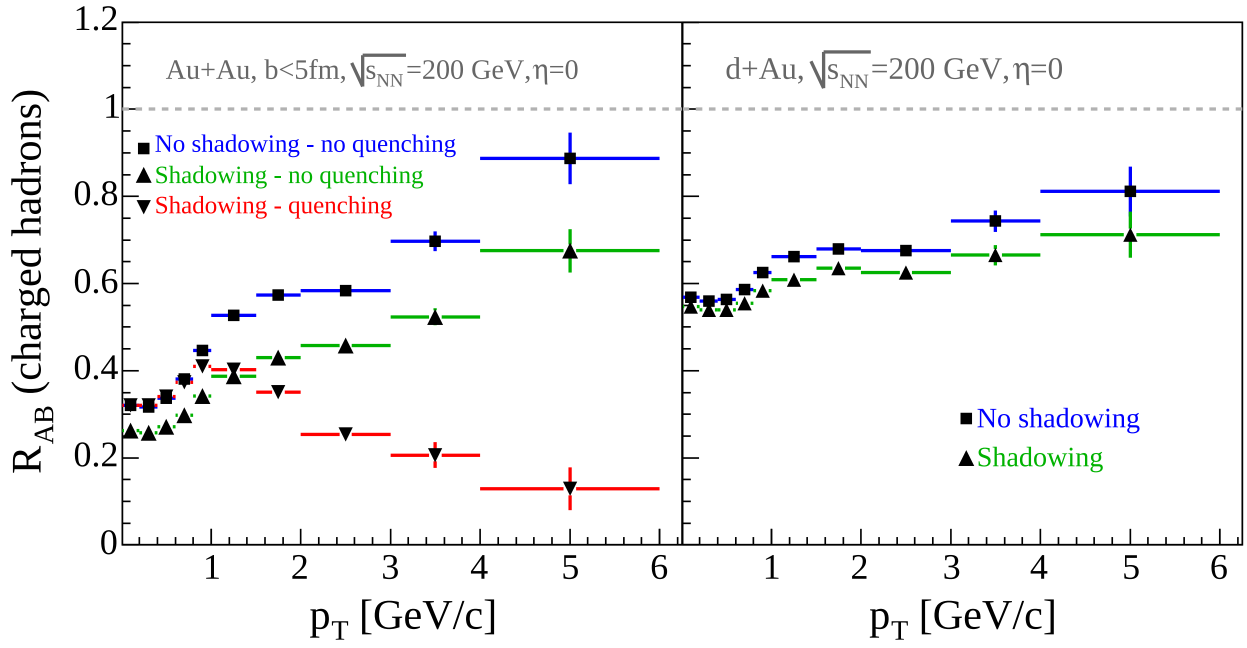

Figure 2.7: HIJING predictions of the nuclear modification factor R_{AB} for unidentified charged hadrons. Left: Central $Au + Au$ collisions ($b < 5\,\mathrm{fm} \sim 0 - 10\%$). Right: $d + Au$ collisions (no centrality selection). The used reference is constructed from HIJING $p + p$ collisions and the mean number of binary collisions is taken from the analyzed event sample. The effect of shadowing is larger in central $Au + Au$ than in $d + Au$, since the depletion of low x partons is significant in both the Au nuclei. The jet quenching mechanism clearly suppresses the high p_T region in $Au + Au$ – the high p_T suppression results in slightly enhanced particle production at lower p_T.

Shadowing in HIJING is modeled by a simple modification of the parton structure function. The depletion is constrained by data from the EMC experiment and it is assumed that quarks and gluons are equally shadowed in the low$-x$ region. The parton structure function suppression (for partons in a bound nucleon as compared to a free) is given by a simple parametrization of the nuclear radius, the atomic number and the transverse distance from the nucleon to the center of the nucleus (see ref. [41] for details). The shadowing mechanism is purely phenomenological. It does not have any adjustable parameters and cannot be used to study shadowing in a more quantitative manner.

Jet quenching is modeled by letting the high p_T partons lose energy along their path uniformly, i.e. the energy lost per unit length (dE/dl) is constant. The path length on the way out of the reaction zone is calculated assuming a simple cylindrical geometry of the opaque medium. The number of interactions, i.e. the number of times the parton looses energy, is calculated from the path length and the mean free path λ_s. The lost energy is distributed to the quark-diquark strings that represent the pre–hadronization state in the model. This mechanism naturally leads to a quenching of the the high p_T particles, while the lost energy leads to an enhanced production of lower p_T particles. The default values used in the model are $dE/dl = 2\,\mathrm{GeV/fm}$ and $\lambda_s = 1\,\mathrm{fm}$. "While this jet quenching mechanism is obviously very schematic, it is sufficient to estimate the order of magnitude of the effects that are likely to result from final state interactions. More quantitative estimates will require the development of a microscopic parton shower and cascade model ..." [63].

HIJING (with quenching and shadowing) was very successful in describing the overall multiplicity of $Au + Au$ collisions at RHIC. The model is less successful in describing the high p_T nuclear modification. In the $Au + Au$ collisions the nuclear modification shows the qualitative features of the data: a raise at low p_T and a drop off above some maximum. The model does not include Cronin effect and is less successful in $d + Au$ collisions. Figure 2.7 illustrates the effect of the shadowing and jet quenching $Au + Au$ and $d + Au$ collisions around mid–rapidity at $\sqrt{s_{NN}} = 200\,\text{GeV}$.

2.4.2 Vitev-Gyulassy

Vitev and Gyulassy have developed a model of the nuclear modification that includes nuclear shadowing, Cronin effect and jet quenching [60]. It is a good example of how the three effects can be modeled and it illustrates well how they interplay at different energies.

The model only describes the modification of the high p_T inclusive hadron spectra and is not valid below $p_T = 2\,\text{GeV/c}$. The base line in the model is standard phenomenological pQCD calculation of inclusive hadron spectra from $p + p(\bar{p})$ collisions (see equation 2.1). The calculation is modified to take into account the nuclear geometry and the three nuclear effects:

$$\begin{aligned} E_h \frac{dN_h^{AB}}{d^3p} &= KT_{AB} \sum_{abcd} \int dx_a dx_b \int d^2k_a d^2k_b g_A(k_T^a) g_B(k_T^b) \\ &\times S_A(x_a, Q_a^2) S_B(x_b, Q_b^2) f_{a/p}(x_a, Q_a^2) f_{b/p}(x_b, Q_b^2) \\ &\times \frac{d\sigma^{ab\to cd}}{d\hat{t}} \int_0^1 d\epsilon P(\epsilon) \frac{z_c^*}{z_c} \frac{D_{h/c}(z_c^*, Q_c^2)}{\pi z_c}. \end{aligned} \tag{2.6}$$

The shadowing is modeled by shadowing functions $S(x, Q^2)$, the Cronin enhancement by modification of the k_T broadening functions $g(k)$ and the jet quenching by an energy loss term and modification of the fragmentation. The K factor (see section 2.1) is independent of collision type ($N + N$ or $A + B$) and cancels out in the nuclear modification factor.

The modeling of the nuclear shadowing is done using the EKS98[3] parametrization [64] of the shadowing function.

The Cronin effect is modeled by an additional k_T broadening of the parton distribution function – the $g(k_T^{a/b})$ functions in equation 2.1 have become $g_{A/B}(k_T^{a/b})$. The origin of the Cronin effect is assumed to be random elastic scattering in the initial state. If L_A and λ denotes the path length in the nucleus and mean free path, respectively, the partons undergo L_A/λ scatterings. In a simple picture, each scattering broadens the k_T distribution by μ (where μ is the screening scale). This broadening in the model is modified by a logarithmic function so that

$$\langle k_T^2 \rangle_{pA} \approx \langle k_T^2 \rangle_{pp} + L_A \frac{\mu^2}{\lambda} \ln(1 + p_T^2 c/\mu^2) \tag{2.7}$$

The phenomenological transport parameters ($\hat{q} = \mu^2/\lambda$ and c/μ^2) are set according to expectations and fits to data from $p + A$ collisions. The initial broadening $\langle k_T^2 \rangle_{pp}$ (together with the K factor) is set to reproduce data from $p + \bar{p}$ over the full p_T range.

The jet quenching is incorporated in the fragmentation function by modifying the momentum fraction of the jet $z = p_h/p_{jet}$ carried away by the leading hadron, $z^* = z/(1 - \epsilon)$, where ϵ is the fractional energy

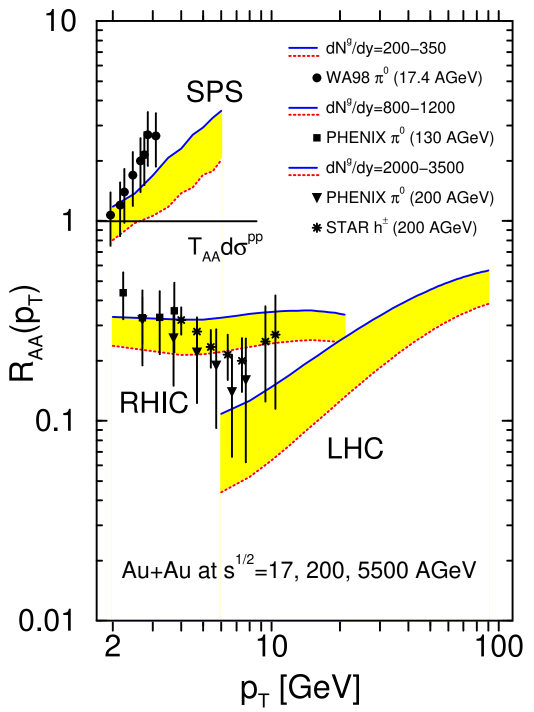

Figure 2.8: Nuclear modification factors at mid–rapidity for central collisions at SPS ($Pb + Pb$), RHIC ($Au + Au$) and LHC ($Pb + Pb$). The plot is from [60].

[3]EKS are the initials of the physicists who came up with the parameterization, Eskola, Kolhinen and Salgado. 1998 was the year of the publication.

loss. The energy loss is calculated from the radiative gluon energy spectrum as in ref. [65] (the GLV[4] approach). The distribution of the fractional energy loss $P(\epsilon)$ is integrated over the longitudinal expansion of the medium.

Figure 2.8 shows the nuclear modification factors (for central $Au+Au$ collisions) at mid–rapidity for SPS, RHIC and LHC energies, calculated with different assumptions on the gluon density (yellow bands). The figure also includes data from SPS and RHIC and the model seems to describe the data fairly well. The model was presented before the 2003 $d+Au$ run at RHIC and it turned out that the prediction (see ref. [60] for details) was in qualitative agreement with the data (unlike most predictions for the $d+Au$ nuclear modification factors before the $d+Au$ RHIC run).

Does the model have any weaknesses? It could be argued, that the assumptions behind the modeling of the Cronin effect is only valid in cold nuclear matter – the parameters that go into the k_T broadening are determined from $p+A$ data. How well this applies in the dense medium created in $A+A$ collisions is not obvious and it is also not discussed in ref. [60]. Another problem is the implicit assumption that the different nuclear effects can be modeled independently and implemented by multiplicative functions or modifications to the phenomenological pQCD calculations, i.e. it is assumed that the modifications factorize.

2.4.3 Cassing-Gallmeister-Greiner

Gallmeister, Greiner and Xu challenged the *standard* explanation of the observed jet quenching due to parton energy loss in ref. [37]. They argued that most of the hadrons stemming from jets could materialize early enough to lose a significant amount of energy in late hadronic final state interaction (elastic and inelastic scattering) with the bulk of co–movers. The observed suppression could therefore be due to elastic hadron scattering instead of the proposed parton scattering in a deconfined medium. The paper does not exclude the partonic description, but emphasizes the importance of investigating the role of late hadron elastic scattering.

In a later paper [66] Gallmeister, Greiner and Cassing suggest a model that includes both pre–hadronic and hadronic interactions. The conception *pre–hadron* is not discussed in the paper.

The model uses the hadron–string dynamics (HSD) [67] to describe the bulk matter, i.e. quark–diquark (baryonic) or quark–antiquark (mesonic) strings, and hadrons after hadronization. The production of jets (partons with $p_T > 1.5\,\mathrm{GeV/c}$) is modeled using the PYTHIA event generator [68]. The merging of a string model (to describe the soft particle production) and pQCD (to describe the hard particle production) resembles the approach used in HIJING (see section 2.4.1). The formation time τ_f of hadrons in the model (the time in which the partons are treated as pre–hadrons) is assumed to be constant in the rest frame of the hadron and thus independent of the particle specie. The model distinguishes between leading particles and secondary particles. The leading particles are the quarks or diquarks of the jets in the pre–hadronic phase and the leading hadron of the jets in the hadronic phase. In the pre–hadronic phase, the leading particles do not interact with secondary strings, but only with other leading particles. In the hadronic phase, the leading particles can interact with both other leading hadrons and secondary hadrons. The cross sections for interactions between the leading parton and a quark–diquark or quark–antiquark are the hadron (baryon or meson) cross sections weighted by the number of valence quarks in the (baryon or meson) string. In the hadronic phase, the known hadronic cross sections are used. The interactions of the leading particles with the medium (strings in the pre–hadronic phase and hadrons in the hadronic phase) result in a strong high p_T suppression.

The model also incorporates initial state multiple scattering by adding a simple k_T broadening term in the string fragmentation, $\langle k_T^2\rangle = \langle k_T^2\rangle_{pp}(1+\alpha N_{prev})$, where N_{prev} is the number of previous collisions and $\alpha \approx 0.25 - 0.4$ is fixed to fit the measured distributions.

In the model, late final state hadron energy loss still contributes significantly to the suppression, but it is concluded that "the interaction of fully formed hadrons are practically negligible in central $Au+Au$ collisions at $\sqrt{s_{NN}} = 200\,\mathrm{GeV}$ for $p_T \geq 6\,\mathrm{GeV/c}$, but have some importance for the shape

[4] GLV stands for Gyulassy, Levin and Vitev

of the ratio R_{AA} at lower p_T ($\leq$ 6 GeV/c)." [69]. Figure 2.9 show the comparison of the model predictions with the STAR and PHENIX data. The blue band is with the Cronin k_T broadening, the purple curve is without.

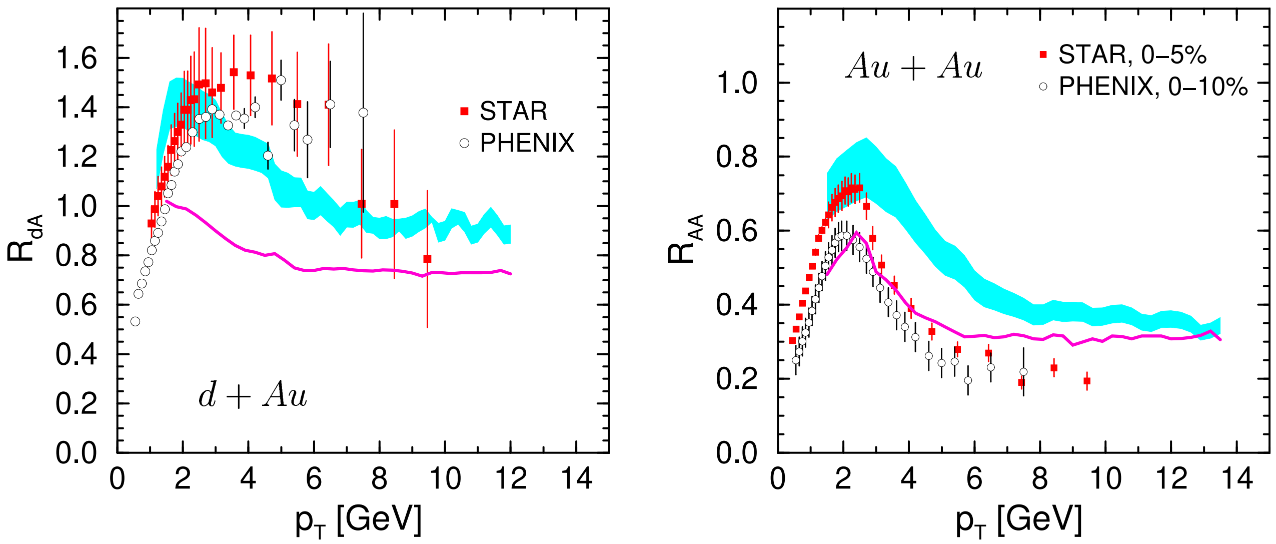

Figure 2.9: Comparison between the Cassing–Gallmeister–Greiner model and data from STAR and PHENIX. The nuclear modification factor is shown for minimum bias $d + Au$ collisions (left panel) and for central $Au + Au$ collisions (right panel). The model predictions are shown as the purple curves (without k_T broadening) and as light blue bands (with k_T broadening).

The fact that the leading particles in the pre–hadronic phase are only allowed to interact with other leading particles could be questioned, especially when the high density of non–leading partons (strings) is considered. It could therefore be argued that the model underestimates the importance of the pre–hadronic energy loss. At the same time it seems to overestimate energy loss by hadronic re–scattering, i.e. the modeled nuclear modification factor is lower than the data for the $d + Au$ collisions (figure 2.9, left panel) and slightly higher than the data for the central $Au + Au$ collisions (figure 2.9, right panel). In conclusion, the model uses a different approach to calculate the energy loss, which seems to favor the importance of the hadronic re–scattering, and still concludes that energy loss in the pre–hadronic phase is important at RHIC.

2.4.4 Hirano–Nara

The ingredients in Hirano and Naras model [70] are hydrodynamic description of the expanding dense medium and pQCD for the production of hard particles.

The expanding medium is assumed to be in the QGP phase in the initial stages of the collision and assumptions on the initial conditions (spacial extension and equation of state) of the medium is made. The medium expands and hadronizes at a temperature T_C = 170 MeV. The evolution in the hadronic state is described using the the partial chemical equilibrium model (PCQ) [71]. This detailed model of the bulk matter evolution provides the medium densities (and local velocities) for calculating the energy loss of the hard particles. Moreover it reproduces the measurements of the low p_T particles (multiplicities and radial and elliptical flow).

The hard partons are generated according to PYTHIA [68]. Nuclear shadowing is modeled using the EKS98 parametrization (as in the Vitev–Gyulassy model, section 2.4.2). Multiple initial state scattering is modeled using a (standard) Gaussian broadening of the initial transverse momentum distribution. The fragmentation into hadrons are also obtained by PYTHIA fragmentation scheme.

The fragmentation cannot be treated independently in the low p_T region and for the reference spectrum, the Lund string fragmentation model is used (which is also incorporated in the PYTHIA model). This gives the possibility to construct a reliable nulcear modification factor for $p_T < 2\,\mathrm{GeV/c}$.

The jet–quenching is simulated by letting the hard partons lose energy in the medium using an approximation to the GLV formula. The energy loss in the pre–thermalization phase ($\tau < 0.6\,\mathrm{fm/c}$) is neglected. The energy loss is calculated in the local rest frame of the medium, which means the the expansion of the medium (also in the longitudinal direction) is taken into account.

Figure 2.10 shows the calculation of the nuclear modification factor for charged hadrons at $\eta = 0$, $\eta = 2.2$ and $\eta = 3.25$. The modification is approximately the same for the three pseudo–rapidities – this illustrates that the suppression does not simply depend on the number of particles the jet *meets* on the way out (the pseudorapidity density), but that the expansion of the medium also plays an important role.

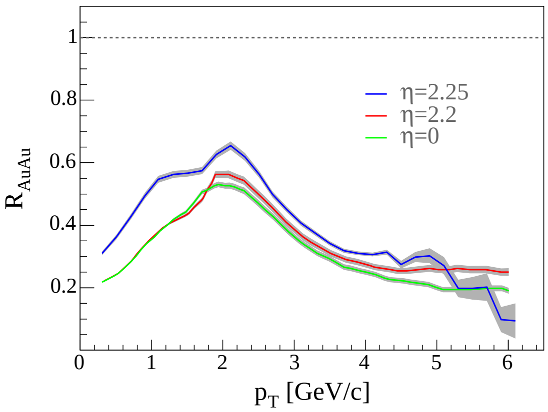

Figure 2.10: Nuclear modification factors for charged hadrons at $\eta = 0$, $\eta = 2.2$ and $\eta = 3.25$ for central $Au + Au$ collisions.

In ref. [70] the model calculations are compared to BRAHMS data on the pseudo–rapidity dependence on the high p_T suppression. The measured nuclear modification factor is for negatively charged hadron, while the model considers both negative and positive hadrons. This difference is not mentioned in the paper.

2.5 The Color Glass Condensate

The Color Glass Condensate theory describes the evolution of the gluon density (and thereby also the cross sections in hadron collisions) for very small values of x. In deep inelastic scattering it has been observed that the gluon density grows rapidly with decreasing x. This has traditionally been described by the so called QCD evolution equations (BFKL[5] [72, 73] and DGLAP [48, 49, 50]).

In the high energy limit of QCD (defined as the limit $x \to 0$ with constant momentum transfer Q) the traditional linear evolution equations (BFKL) have an *infrared problem* – that is, the gluon densities (and thereby the cross sections) diverge. This lead to the conjecture that the density of gluons is limited, i.e. there exist gluon saturation. The saturation is explained by gluon recombination (or gluon fusion) that is expected to play a role at densities $\sim 1/\alpha_S$ [74]. The saturated gluons act highly coherently and resemble a condensate. The low$-x$ gluons are generated from gluons at larger values of x. In high energy collisions the time scales of these gluons are Lorentz dilated. The time dilated scales are transfered to the low$-x$ gluons, which therefore evolve very slowly compared to the natural (non–dilated) time scales. This property resembles the property of a glass. The glass–like condensate of gluons is called The Color Glass Condensate (CGC).

Figure 2.11 shows the domains of the different QCD evolution frameworks in the $\tau - \ln Q^2$ plane ($\tau = \ln(1/x)$). The non–linear CGC evolution equations reduce to the BFKL and DGLAP equations in appropriate limits, i.e. high x and high Q^2. The momentum transfer where the saturation sets in for a given x is given by $Q_S \sim (x_0/x)^\lambda$, where x_0 and λ can be determined experimentally.

Measurements of virtual photon scattering on protons at HERA for $x \leq 10^{-2}$ and $Q^2 \leq 45\,\mathrm{GeV}^2$ show good agreement with the CGC model, while the BFKL approach gives too high cross sections in the low Q^2 range. These measurements determines λ to be ~ 0.3

In heavy ion collisions, the saturation momentum Q_S is higher, since the parton wave function not only overlaps within the nucleon but wihtin the whole nucleus. The saturation momentum is

[5]BFKL are the initials of the physicists who developed the equations, Balitsky, Fadin, Kuraev and Lipatov.

expected to scale with $A^{1/3}$. The collision between the two nuclei can be "visualized as the scattering of two sheets of colored glass." [75]. In this description, the very early stage of the collision is a melting Color Glass Condensate, which evolves into the highly exited collision zone. The evolution of the collision is shown in figure 2.12.

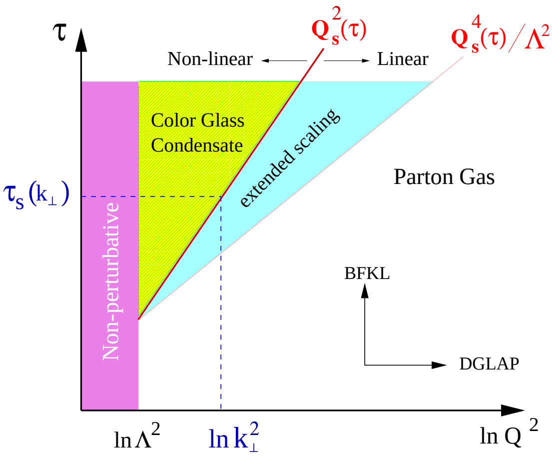

Figure 2.11: Regions of QCD evolutions in the $\tau - \ln Q^2$ plane ($\tau = \ln(1/x)$). The Color Glass Condensate describes the QCD cross sections at low x. The figure is from ref. [74].

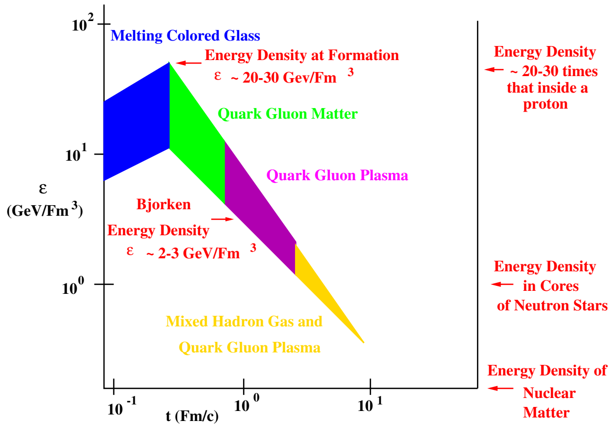

Figure 2.12: The evolution of an ultrarelativistic heavy ion collision in the CGC picture. The quark gluon plasma is created from a melting CGC. The figure is from ref. [32].

Chapter 3

The Experimental Setup

3.1 The Relativistic Heavy Ion Collider

The Relativistic Heavy Ion Collider (RHIC) [76] is part of the accelerator complex at Brookhaven National Laboratory (BNL) in Long Island, USA. It is designed to collide nuclei at ultra relativistic energies. RHIC started operating in 2000 with the primary goals of colliding $Au + Au$ and $p + p$ at $\sqrt{s_{NN}} = 200\,GeV$. Table 3.1 shows an overview of the RHIC running periods until now. Figure 3.1 shows a schematic overview of the accelerator complex. The beam is accelerated in several steps before it is split into two beams and sent into the two RHIC rings. The beam going clock–wise around RHIC has been named the *blue* beam and the one going counter clock–wise is the *yellow* beam. At four of the six interaction regions (beam crossing points), the blue and the yellow beams are brought to collision. The ions in the beams are bunched – in the $Au+Au$ runs there are 56 bunches of $\sim 10^9$ ions in each of the RHIC rings. The bunching is done in order to control the time of the interactions and the width of the interaction $z-$distribution (along the beam axis). The crossing of two bunches gives a relatively narrow time and z window where interactions can occur. At the four interaction regions, the four RHIC detectors (STAR [77], PHENIX [78], PHOBOS [79] and BRAHMS [80]) are located.

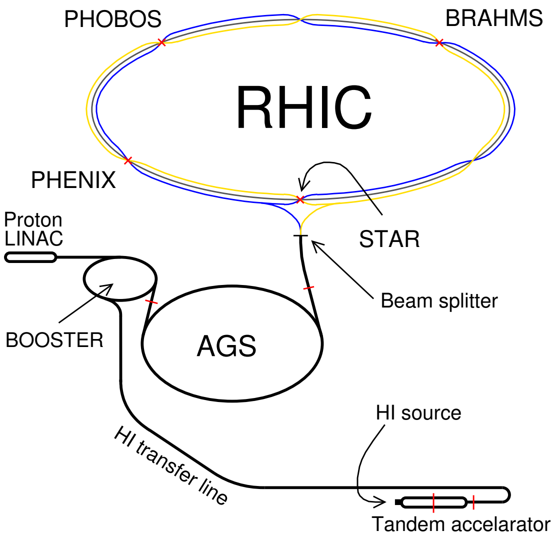

Figure 3.1: Schematic overview of the RHIC accelerator complex.

	system	$\sqrt{s_{NN}}$ [GeV]	period
Run I	$Au + Au$	130	summer 00
Run IIa	$Au + Au$	200	fall 01
Run IIb	$p + p$	200	fall 01
Run IIIa	$d + Au$	200	winter 02/03
Run IIIb	$p + p$	200	spring 03
Run IVa	$Au + Au$	200	winter 03/04
Run IVb	$Au + Au$	62.4	spring 04
Run IVb	$p + p$	200	spring 04

Table 3.1: The running periods at RHIC untill now.

3.1.1 The Interaction Region

Figure 3.2 shows a schematic top view of the interaction region (IR). The two DX magnets steer the beams into a single beam pipe so that the nuclei collide at zero angle. The transverse dimensions of the beams are typically $1-2$ mm. The beam pipe between the DX magnets has a radius of 3.81 cm. Around the nominal interaction points (± 0.75m in the BRAHMS IR) it is made of beryllium in order to reduce secondary interactions. The beryllium beam pipe is 1.2 mm thick.

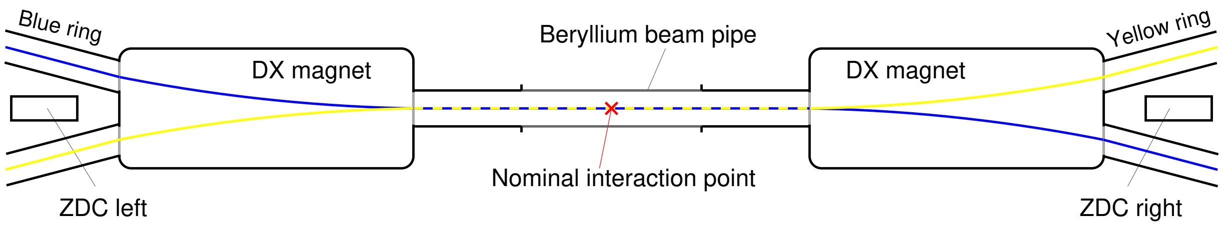

Figure 3.2: Schematic view of the interaction region.

3.2 The BRAHMS Experiment

The BRAHMS experiment [80] is designed to measure charged hadrons produced in high energy heavy ion collisions. BRAHMS has the capability to identify particles over a broad range of angles and momenta (or rapidities and transverse momenta), though with the drawback that only small regions of the phase space are investigated per setting of the detectors. A complete *average* picture of the final state (the extended spectra) is obtained by combining data sets from many different settings.

3.2.1 Basic Idea of the Setup

The experimental setup consists of two independent small solid angle spectrometers and a set of detectors for event[1] characterization. Figure 3.3 shows a schematic (top) view of the setup. The two spectrometers can rotate around the nominal interaction point (IP) in the horizontal plane and they thus cover two different polar angle ranges.

The Midrapidity Spectrometer (MRS) is designed to measure charged particles emitted around mid–rapidity and covers angles from 30° to 90°. The main detectors are two time projection chambers (TPC), TPM1 and TPM2, that can measure the particle trajectories through the spectrometer. A dipole magnet (D5) is positioned between the TPCs – here, the charged particles trajectories are deflected and the momentum to charge ratio can be determined. Three detectors for particle identification are located in the back end of the spectrometer: A time-of-flight detector (TOFW), a threshold Cherenkov detector (C4) and a second time-of-flight detector (TFW2). A number of smaller scintillator detectors have been added for calibration and trigger purposes. The first three components (TPM1-D5-TPM2) of the spectrometer are positioned on a platform that can be moved back by up to 50 cm – this is done in order to reduce the track density in TPM1 in runs where large particle densities are expected, e.g. $Au+Au$ runs where MRS is positioned at lower angles.

The Forward Spectrometer (FS) measures particles emitted in the forward direction. It has two independent parts, the front forward spectrometer (FFS) and the back forward spectrometer (BFS). The FFS can rotate from 2.3° to 30°, while the BFS improves the momentum resolution and extends the particle identification performance at the lower angles, from 2.3° to 15°. The sign of the rotation

[1] The word *event* is used for the data recorded when the data acquisition is started by a trigger. One event ideally correspond to one collision.

angle (or the fact that the spectrometer is positioned on the other side of the beam as compared to the MRS) can be ignored since the collisions are statistically axial symmetric.

In the FFS, a dipole magnet (D1) is placed in front of the first TPC (T1). It selects particles of one charge sign and sweeps away low momentum particles in order to keep the track density in first TPCs on a reasonable level. After the D1 magnet, the design is similar to that of the MRS: TPC (T1), dipole magnet (D2), TPC (T2), time-of-flight detector (H1) and threshold Cherenkov detector (C1). In the lowest angle settings ($< 3°$) C1 must be taken out to make room for the DX magnet. The BFS consist of three drift chambers (T3, T4 and T5) and two dipole magnets (D3 and D4) a time-of-flight detector (H2) and a ring imaging Cherenkov detector (RICH). Like in the MRS, scintillator slat detectors have been added for calibration and trigger purposes.

The TPCs and magnets are placed on an arc – the arrangement is such that at full magnetic field (B_{max}) a particle with momentum of 22.5 GeV/c follows the arc of the spectrometer. At a lower magnetic field (B_{max}/N) particles of a lower momentum ($p = 22.5/N$ GeV/c) will follow the arc. The momentum $22.5/N$ GeV/c is called the reference momentum for the given magnet field setting. The back end of the FFS (components after D1) can be rotated so that the (FFS) reference momentum becomes smaller. This setting can be used to measure low momentum particles at the lowest angle setting without having a too high track density in T1.

The spectrometer components are described in more detail in section 3.2.4.

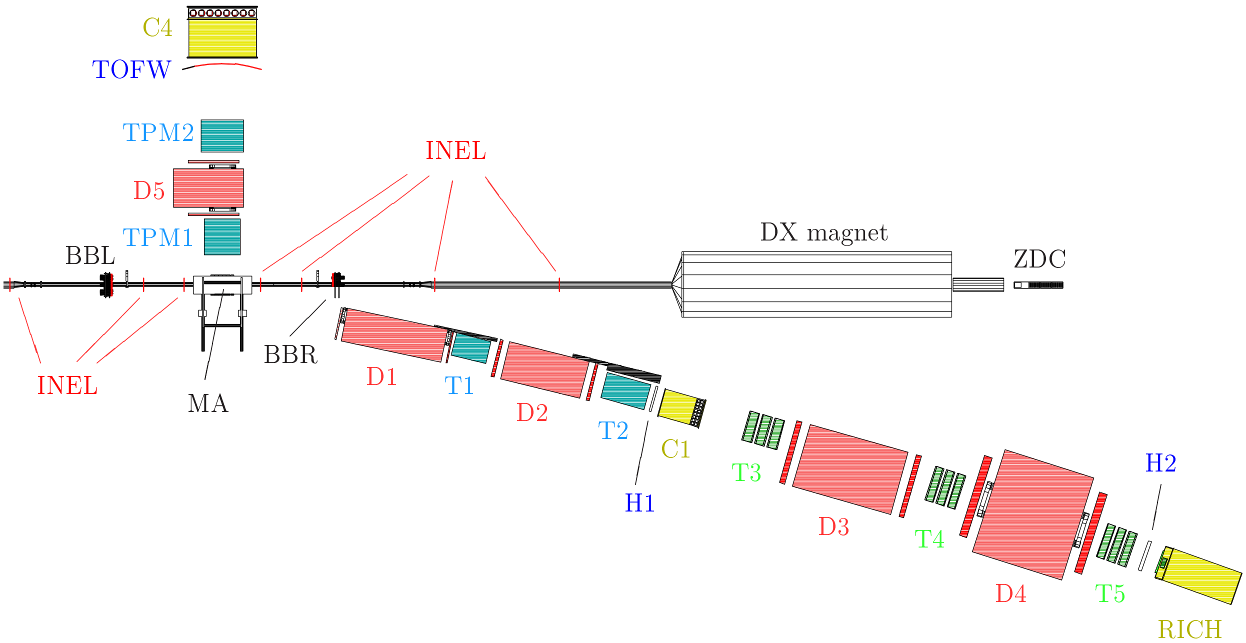

Figure 3.3: Top view of the BRAHMS experiment.

3.2.2 Acceptance

The spectrometers described above allow for particle identification in large ranges of the $y - p_T$ space. This is depicted in figure 3.4 where the acceptances for identified pions, kaons and protons are shown for different spectrometer settings. The areas are calculated from a Monte Carlo simulation with a detailed description of the detector geometry. In this simulation, the collision vertex is varied over ± 15 cm around the nominal interaction point. The shaded gray background shows the complete coverage of the spectrometers.

Charged hadrons are accepted (can be measured) by the spectrometers in the pseudo–rapidity range $-0.2 < \eta \lesssim 3.5$ and to very high transverse momenta. In the MRS there is, in principle no p_T limit. A particle of infinite high momentum will make a straight track through the spectrometer and be measured, however with a very uncertain momentum determination. In the FFS, it is also possible to reconstruct particles of arbitrarily high momentum. In the full FS however, the components are placed in an arc so that a straight line cannot be drawn through the spectrometer. A particle of very high momentum (which would be deflected little by the magnetic fields) can therefore not make it through the full FS, i.e. there is a limit to how high momentum (or p_T) particles can have and be measured. The limitation in the high p_T measurements is however mostly set by the statistics in the high p_T region.

3.2.3 Global Detectors

The so called global detectors are designed to measure the overall characteristics of the collisions and to provide triggers for the data acquisition (DAQ). The overall characteristics are the collision vertex and the collision centrality/multiplicity. The global detectors are: The beam-beam counters (BBC), the multiplicity array (MA), the zero degree calorimeters (ZDC) and the inelastic scintillation counters (INEL).

Beam-Beam Counters

The Beam-Beam counters are designed to measure the collision vertex, determine a start time for the time-of-flight measurements and provide triggers. They also give information on the charged particle multiplicity in the pseudorapidity region $2.2 < |\eta| < 4.6$. The two counters are positioned along beam line at 2.19 meters on each side of the nominal IP. Each counter consist of an array of Cherenkov detectors – small cylindric radiators attached to fast photo–multiplier (PM) tubes. The left counter is azimuthally symmetric, while the right is asymmetric so that particles can stream freely toward the FS.

The time signals in the counters come from fast particles and the time difference from the "average" time in the left and the right counters is used for vertex and start time determination. The quotation marks indicate that the average is not a simple average, but is derived from an elaborate algorithm (see section 4.1.1 or ref. [81] for details).

The accuracy of the time measurement depends on the occupancy of the detectors (tubes) that are used in the time calculation. If a large fraction of the tubes are not hit by a fast particle, a good time signal cannot be calculated. This is the reason for the different sized tubes. In high multiplicity events, most of the small tubes are hit and a very accurate time signal can be calculated. In low multiplicity events, a large fraction of the small tubes are not hit and the "average" is not accurate, but the occupancy in larger tubes is still good and a reasonable time measurement can be obtained.

The resolution of the vertex and start time measurements therefore depends on the multiplicity – for central Au+Au collisions it is $\approx 20\,\mathrm{ps} \sim 0.6\,\mathrm{cm}$.

Zero Degree Calorimeters

The two zero degree calorimeters are designed to measure the spectator neutrons that continue at very small angles after the collision.

The calorimeters are located 18 m down stream on each side of the nominal interaction point (IP), just behind the DX magnets, each covering a solid angle of 2 mrad. Spectator neutrons that are not bound in charged nuclear fragments (which are swept away by the DX magnet) give signals in the detectors. The number of neutrons can be estimated from the high resolution energy measurements – this can give information on the collision centrality (see section 4.1.2), while the time signals are used to determine the collision vertex (as for the BBC).

The ZDCs, that are common to all four RHIC experiments, are also used for beam intensity measurements by the RHIC operators and in the minimum bias trigger in the heavy ion collisions studies. More details can be found in ref. [82].

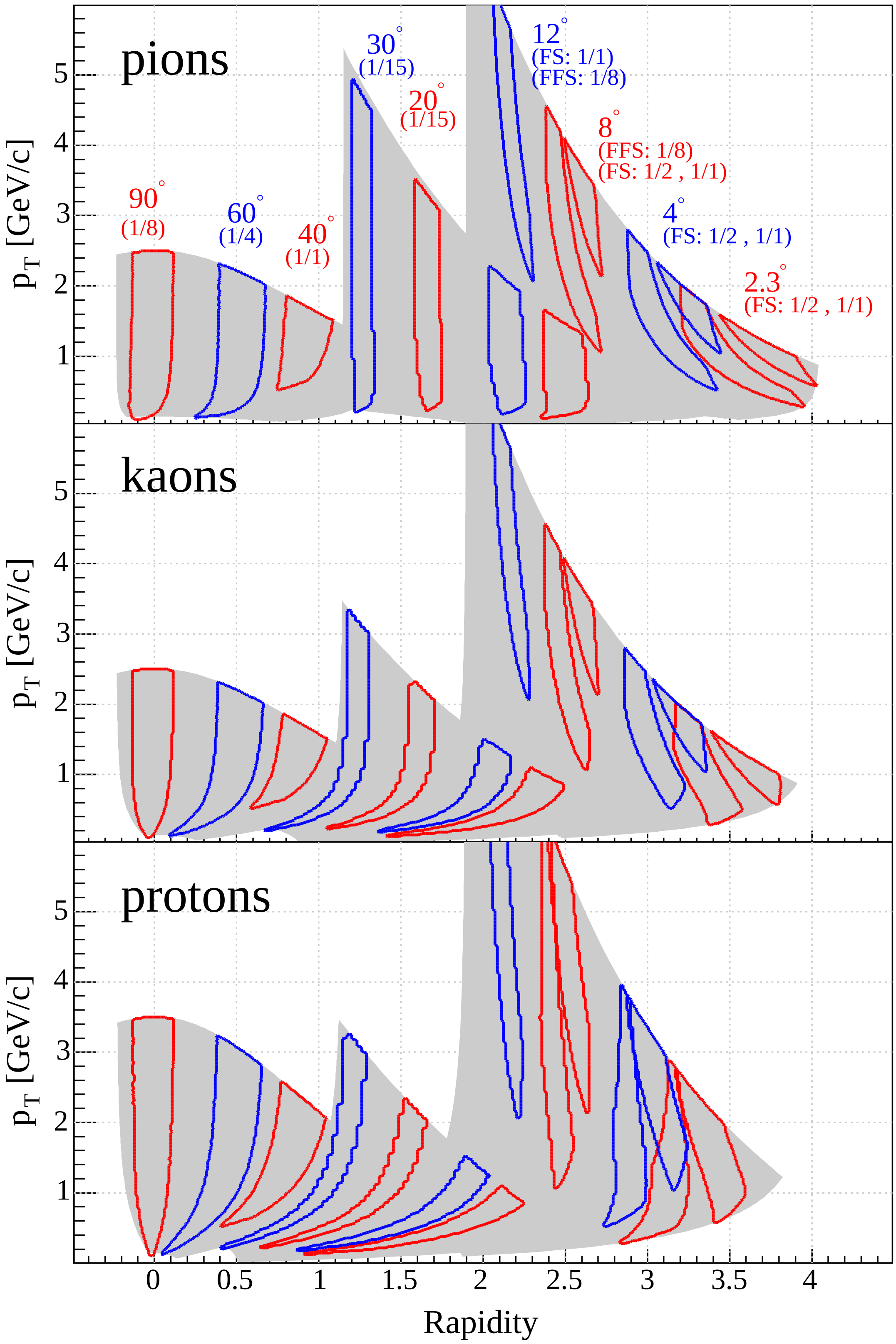

Figure 3.4: BRAHMS acceptance for pions, kaons and protons. The red and blue regions indicate the coverage of single spectrometer settings.

Multiplicity Array

The multiplicity array is used to establish overall charged particle multiplicities and provide measurements of the collision centrality (see section 4.1.2). It has also been used for charged particle fluctuation measurements [83, 84]. The MA consist of two hexagonal detector barrels that surround the interaction region and cover the pseudorapidity range $-2.2 < \eta < 2.2$ with respect to the nominal IP. The inner part is a highly segmented silicon detector (SiMA) while the outer part is a more roughly segmented detector built of scintillator tiles (TMA). In order to limit the material in front of the two spectrometers and let particles pass freely, the two vertical sides in the barrel are not fully instrumented.

Both detector systems measure the energy deposited by charged particles from which the charged particle multiplicity and collision centrality can be determined. Details on the MA array can be found in ref. [85]. In the fall 2003 (before Run IV), the silicon detector array was rearranged to make the determination of the reaction plane possible.

Inelastic Counters

In collisions between smaller systems (e.g. $p + p$ and $d + Au$), the multiplicity is so low that a good minimum bias trigger cannot be achieved from the BBC or ZDC signals. Therefore, the inelastic counters have been added. These consist of eight rings of scintillation detectors, four on each side of the interaction region, positioned at $z = \pm 75, \pm 155, \pm 416$ and ± 660 cm. Each ring consist of four plastic scintillation plates, surrounding the beam pipe, each connected to a PM tube. The counters measure charged particles and apart from the trigger purpose, they can also measure the collision vertex from the difference between the time signals. In $p + p$, the vertex resolution is ~ 5 cm and the minimum bias trigger selects events corresponding to $\approx 71\%$ of the interaction cross section (see section 5.4.2). Figure 3.5 shows an overview of the inelastic counters.

3.2.4 Spectrometer Components

Tracking Devices

The Time Projection Chambers are designed to determine the three dimensional trajectories of charged particles through the spectrometers. TPM1 and TPM2 are placed on each side of the D5 magnet, while T1 and T2 are placed on each side of D2.

Each of the four TPCs consists of a box filled with gas that is easily ionized by charged particles. In this sensitive volume, a strong homogeneous electrical field makes the created electrons drift up toward a complex readout system. The charge distribution on the segmented two dimensional readout plane in the top of the box gives the $x - z$ coordinates along the charged particle trajectory. The drift time (time signals) combined with the known drift velocity of the electrons in the electrical field gives the y coordinates. Details can be found in ref. [86, 80, 87].

The angular resolution of the tracks measured by the TPCs are $\sim 0.1°$.

The Drift Chambers (T3, T4 and T5) are the tracking devices in the BFS. Here, the number of tracks per event is lower than in the MRS or FFS so that drift chambers, that cannot handle the same high track density as the TPCs, are sufficient.

The DCs are wire chambers – each has three modules that consist of a sensitive gas volume with a number of wire planes (spanning the $x - y$ direction). The combined hit information from the wire planes gives a number of hits in the different $x - y$ planes, which are combined to tracks. The angular resolution of the DC tracks are $\sim 0.05°$.

Magnets

The four magnets are all conventional dipole electromagnets. Each of them is positioned between tracking chambers (except for D1), in order to deflect charged particle trajectories for momentum

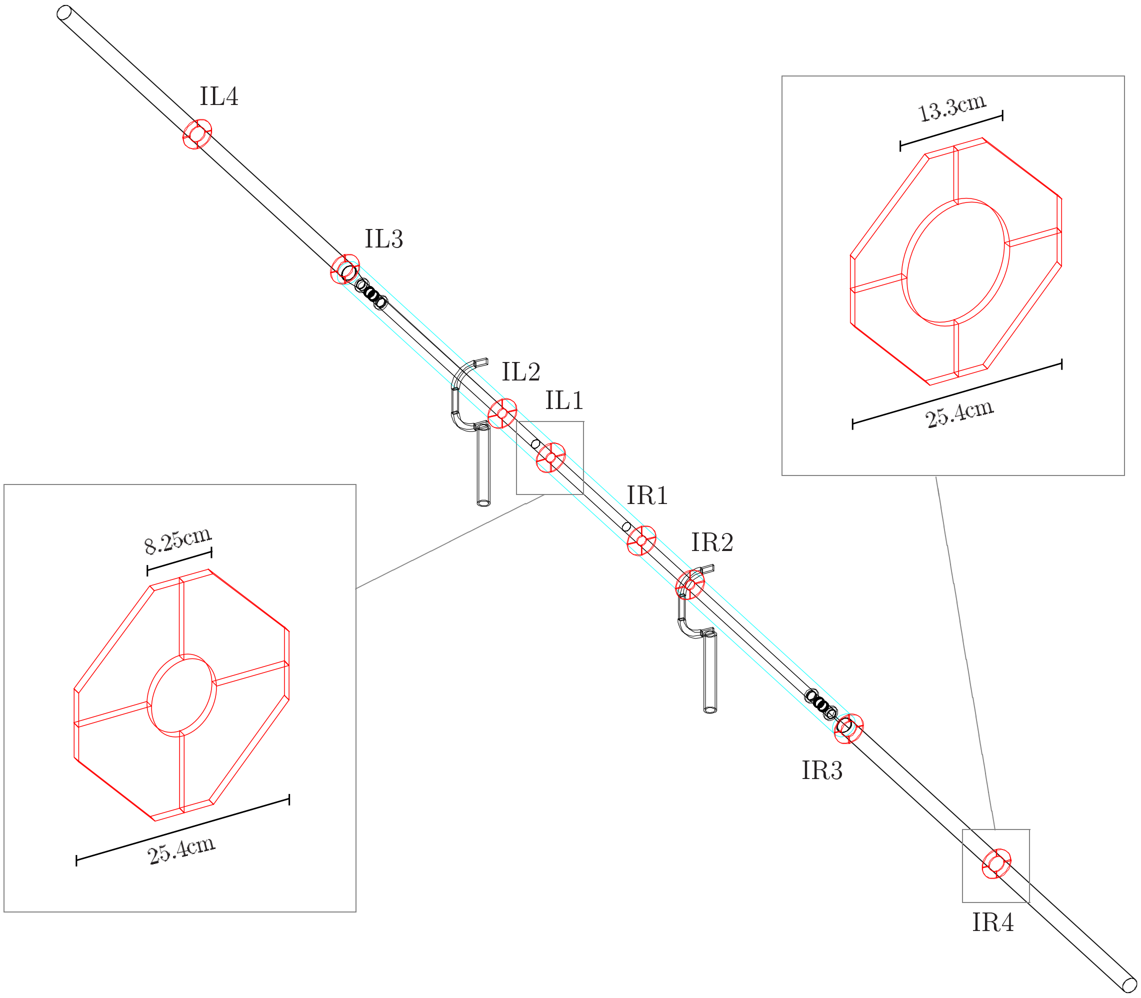

Figure 3.5: The inelastic counter setup. The eight rings are placed so they together cover angles from 0.58° to 9.75° on each side of the nominal interaction point.

determination. The magnetic field inside the magnet gap is constant and has, to first approximation, only a vertical (y) component. The magnet clamps assure a rapid decrease of the magnetic field outside the magnet.

Time–of–flight Detectors

The four time–of–flight detectors (often called hodoscopes or time–of–flight walls) consist of scintillator slats with PM tubes attached at the top and the bottom. They measure the flight time of charged particles. Given the flight time, the distance from the vertex to the detector and the particle momentum, the mass–squared of the particle can be determined and the particle identified (see section 4.3). The scintillator detectors are positioned side by side in a wall–like arrangement to obtain the desired spatial coverage.
H1 and H2 have only a single panel, each covering the full $x - y$ acceptance of the spectrometer. Every second slat is shifted in the z direction to make space for the PM tubes – this gives a small inefficiency ($\leq 5\%$) for detection of particles that do not move perpendicular to the detector.
TOFW consists of six panels positioned in an arc around the opening of the D5 magnet. Here, the slats in a panel are all in one plane and the light is transferred to the PM via lightguides. This arrangement also results in a small inefficiency since the wrapping around the slats (aluminum foil and light insulation tape) leaves small gaps between the scintillating material.

Cherenkov Detectors

C1 and C4 extend the PID in the FFS and MRS, respectively. They are threshold Cherenkov detectors that measure a light signal if a charged particle traversing the radiator gas volume has a velocity above the light speed in the gas, i.e. the velocity threshold. Particles in some momentum ranges will/will not give a signal, depending on their mass.

The design of C1 and C4 is very similar. The radiator gas is kept in a box. At the back of the box, two mirrors (positioned at angles of $\pm 45°$) reflect the emitted Cherenkov light up or down to arrays of PM tubes. C1 covers the whole $x - y$ acceptance of the FFS and is finer segmented (32 tubes) than C4 (16 tubes) that only covers a limited x range of the MRS. Details on the C1 reconstruction software can be found in section 4.4.

The RICH is a ring imaging Cherenkov detector, placed at the back of the BFS. It consist of a gas volume (the radiator), a spherical mirror that reflects and focuses the emitted Cherenkov photons and a segmented photon detection plane. The velocity of the particle can be found from the angle of the emitted photons (the Cherenkov angle), which is calculated from the radius of the detected ring image (see section 4.4.2). From the velocity and momentum of the particle, the mass–squared can be calculated and the particle identified. Details on the design can be found in refs. [88, 89]. The software for ring reconstruction and particle identification is described in section 4.4.

Figure 3.6 shows regions of the $y - p_T$ space in which the π/K separation and K/p separation can be obtained using the different PID detector systems.

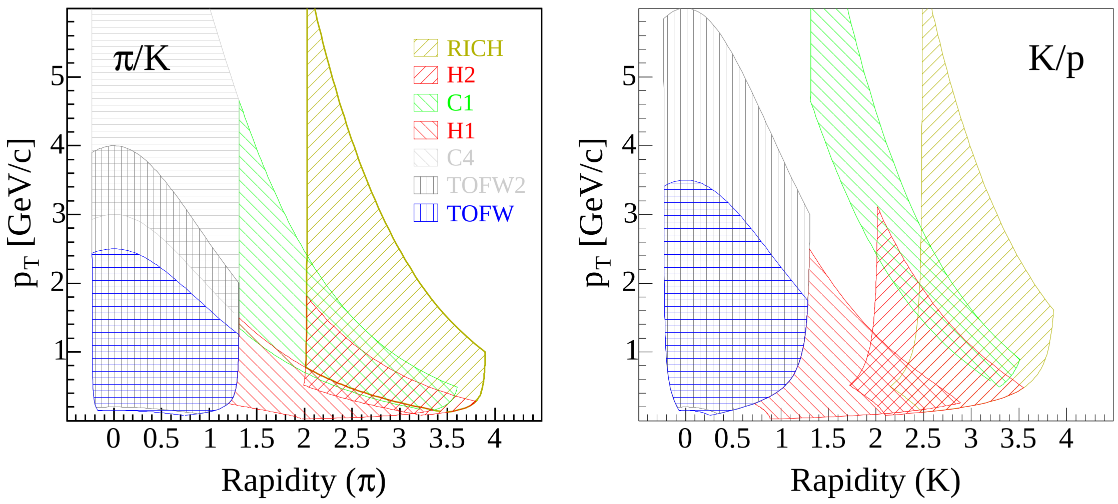

Figure 3.6: Approximate regions of π/K (left) and K/p (right) separation obtained with the different detectors. The rapidity is calculated using the mass of the pion (left) and kaon (right).

Trigger Detectors

MRST0 was used during the $d + Au$ and $p + p$ runs. It consists of 6 scintillator slats placed in front of TPM1. They cover the complete ϕ acceptance of the spectrometer and ± 15 cm in the x direction (in front of TPM1). MRST0 has two purposes. The signals from the 6 slats are used in the MRS trigger (trigger 3) in the $d + Au$ and $p + p$ run and the time signals were used as start in the TOFW and TFW2 time–of–flight measurements.

TRMRS was used during Run IV ($Au + Au$). It is similar to MRST0, but consists of 12 scintillator slats. Its position was between D5 and TPM2 and it is used in the MRS trigger (trigger 3). It covers the complete opening of D5 as seen from the beam line.

TRFS was used during Run IV ($Au+Au$). It is similar to MRST0, but consist of 7 scintillator slats. It was placed between D1 and T1 and it is used in the FS trigger.

3.2.5 Triggers

Signals from single subdetectors or combinations of these are used to define the conditions for which the DAQ should read out the data from all the detectors, i.e. record the event. These conditions are the event triggers of the experiment.

In the different runs BRAHMS had different trigger setups, see table 3.2.

The triggers are set up using hardware logic and the output (the possible trigger signals) is sent to the trigger box, which then tells the DAQ if the event should be recorded. The trigger box can be set to *scale down* the different triggers by some factors, which means that it only lets desired fractions of the different triggers survive. For example, if the minimum bias trigger is scaled down by 100, only one event out of hundred events which meet the minimum bias trigger condition will survive. The ninety-nine other events will not be recorded – unless, of course, they meet the condition of one of the other triggers (and survive the possible scale down this trigger). The trigger information (before and after scale down) is kept for each event in order to *scale up* the events in the data analysis (see section 5.3).

Down–scaling of triggers is necessary due to the limited bandwidth of the DAQ and the limited storage space.

Trigger	Run IIa ($Au+Au$)	Run IIIa ($d+Au$)	Run IIIb ($p+p$)	Run IVa ($Au+Au$)
1	-	BB	BB	BB
2	-	FS	FS	FS
3	-	MRS	MRS	MRS
4	ZDC (MB)	ZDC	-	ZDC (MB)
5	-	INEL(MB)	INEL(MB)	ZDC wide (MB)
6	TMA cent	FFS	-	FFS
7	Pulser	Pulser	Pulser	Pulser
8	Sync.	Sync.	Sync.	Sync.

Table 3.2: Trigger overview for RunIIa, RunIIIa, RunIIIb and RunIV. The excact hardware definition of the triggers varied during runs. Detailed information on the setup can be found in ref. [90].

Chapter 4

Data Reconstruction

The raw data consist of long arrays of numbers, e.g. energy (adc) and time (tdc) signals for each channel in each of the detectors. This data is processed in order to obtain the (physical) quantities that characterize the collision and the particles that emerge from it. This chapter briefly describes some of the basic ideas in this reconstruction process. An important step before the reconstruction can be done, is the calibration of detectors – this is not described in this work, but details can be found in references [81] and [86].

Special focus is put on the resolution of the angle and momentum measurements, since these are especially important in high p_T studies. Also, the reconstruction of the Cherenkov detector signals (for C1 and the RICH) will be described in detail. Open issues and possible improvements are pointed out throughout the chapter.

The tools used for reconstruction and data analysis are the ROOT package [91] and a library package, developed for the BRAHMS reconstruction, called BRAT [92]. The standard BRAT modules are used to reconstruct and reduce data to a format called Data Summary Tree (DST), which contains the relevant data for each event. The more specific analysis (like the one presented in chapter 5) is done from the DSTs.

4.1 Event Characterization

It is assumed that each time the DAQ records an event, it corresponds to a single collision. The word *event* is often used where the meaning is collisions, e.g. *event* plane or *event* characterization. Each collision is characterized by a collision point (vertex position) and a centrality. The orientation of the event plane (see section 1.2.1) is also a global feature of the collision. However, with the 2002/2003 BRAHMS setup, information on the event plane could not be obtained.

4.1.1 Vertex Determination

The vertex position is determined from the difference between time signals from the detectors placed along the beam axis on each side of the nominal interaction point, i.e. the BBC, the ZDC and the INEL (see section 3.2.3). In the $Au+Au$ data, both the BBC and the ZDC are used – in the $d+Au$ and $p+p$ runs, these detectors are not very efficient (due to the low occupancy) and the INEL counters were used instead. In general, the vertex z is calculated from

$$z = \frac{c}{2}\left(\langle t_L\rangle - \langle t_R\rangle\right) \qquad (4.1)$$

where $\langle t_L\rangle$ and $\langle t_R\rangle$ are the average time signals in the left and right detector, respectively. The actual calculation is more complicated since it also takes into account the calibration of the detectors – this is left out here for simplicity.

The ZDC vertex is calculated, as described in equation 4.1, from the average time in the left and right counters. $\langle t_L \rangle$ and $\langle t_R \rangle$ are simple averages between the time signals of the three modules (see section 3.2.3). When the third modules does not provide a valid time signal, the average is then the simple average between the two first modules. The time difference arising from the distance between the modules (difference in cable length from the modules to the DAQ) is subtracted in the calibrations.

The INEL vertex reconstruction is more elaborate: the average times are not simple averages – signals outside a reasonable time window (outliers) are not included. As in the ZDC vertex calculation, the time difference arising from the distance between the different detectors (which in this case is quite large) is subtracted in the calibrations.

The BBC vertex reconstruction algorithm also leaves out outliers in the calculation of the time average. The algorithm is more complicated since it operates with different vertexes calculated from signals in the small and large tubes. Details on the BBC vertex reconstruction can be found in ref. [81].

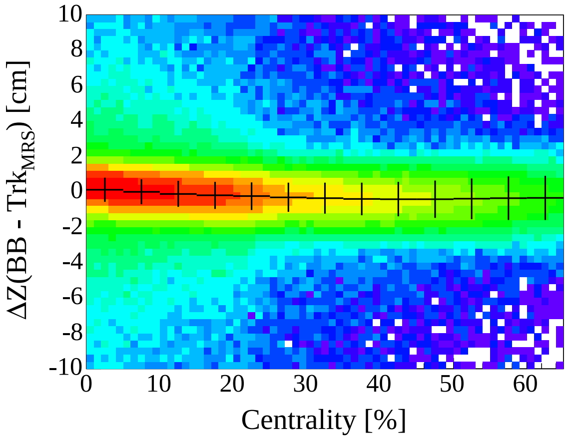

Figure 4.1: Difference in vertex determined from the BBC and the track vertex as function of centrality.

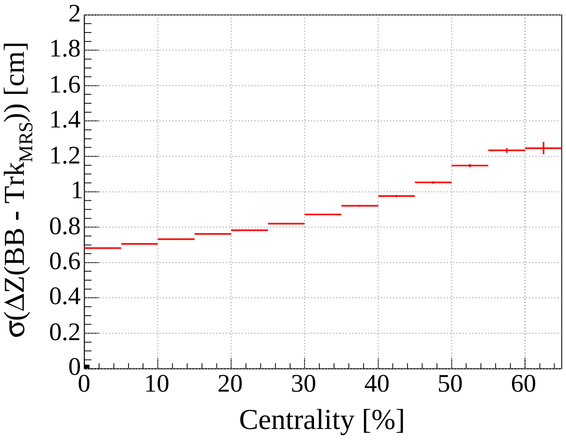

Figure 4.2: The width (from a Gaussian fit) of the difference in vertex determined from the BBC and the track vertex as function of centrality.

The resolution of the vertex determination from the different detectors can be evaluated by studying the correlation between the determined vertex z and the z-component of the MRS track intersection with the $y - z$ plane of the beam. Figure 4.1 shows the difference between the BBC vertex and the track vertex as a function of centrality in the 2002 $Au+Au$ data. The slight centrality dependent offset in vertex is not fully understood. It could arise from the way the slewing correction (see ref [81]) of the BBC tubes is done: The slewing correction is done relative to a reference tube (in the same array), which gives a correlation effect – a large adc signal in the reference tube is likely to be correlated with a large adc signal in the other tubes. A better slewing calibration could probably be obtained by using another detector system, e.g the ZDC, to give the reference time. Figure 4.2 shows the width (from a Gaussian fit) of the difference between the BBC and track vertex. The width becomes larger for less central events, where the occupancy in the BBC array is lower.

4.1.2 Centrality Determination

The centrality is determined from the charged particle multiplicity measured in the multiplicity arrays (MA multiplicity). The top panel in figure 4.3 shows the multiplicity distribution in $Au + Au$ collisions and the defined centrality classes (0-10%, 10-20%, 20-40% and 40-60%). These centrality cuts do not take into account the difference in the MA acceptance as function of the collision vertex. However, in the central region (± 30 cm) this is a minor effect.

As mentioned in section 1.2.1, the centrality definition based solely on multiplicity is not good for peripheral collisions, i.e. it gives broad and overlapping impact parameter distributions for the different centrality classes. A better handle on the impact parameter for the more peripheral collisions can be obtained from the correlation between the multiplicity and the number of detected neutrons in the ZDCs (see bottom panel in figure 4.3).

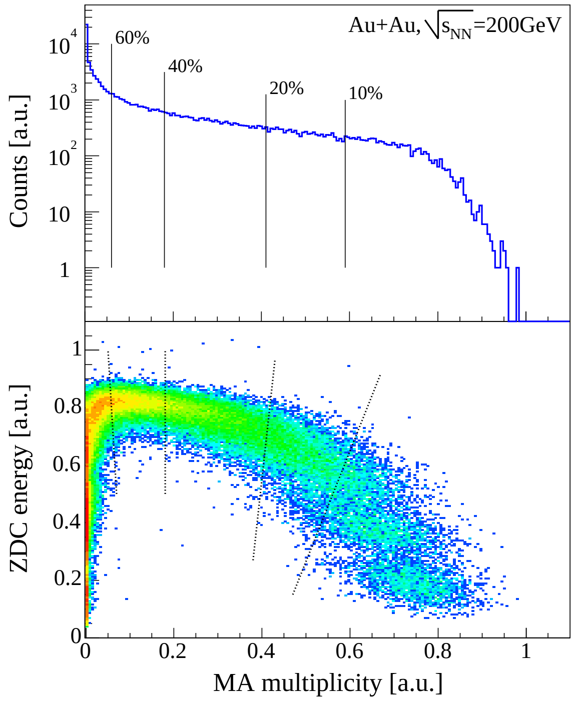

Figure 4.3: Top panel: Normalized min. bias multiplicity distribution. The vertical lines indicate the centrality cuts. Bottom panel: ZDC energy (normalized) as function of multiplicity. The dotted lines indicate how centrality cuts could be defined.

The characteristic shape of the correlation between the measured number of neutrons in the ZDCs and the multiplicity is a result of the fragmentation of the spectator compound and the deflection of these fragments in the DX magnet. The number of detected neutrons in the ZDCs is not proportional to the number of spectator neutrons. Charged fragments of the spectator compound are deflected in the DX magnet and only neutral fragments are detected in the ZDC. In very peripheral collisions ($80-100\%$), the spectator compound does not reach a very high excitation and most of the neutrons are bound in large charged fragments resulting in a low number of detected neutrons. In mid–central collisions ($20-80\%$), the spectator compound gets very exited and breaks up in many fragments, resulting in a higher number of detected neutrons. In central collisions ($0-20\%$), very few neutrons leave the collision with sufficiently small transverse momentum to be measured in the ZDC.

In the 2004 $Au+Au$ run, the high luminosity and the trigger setup (with spectrometer triggers and no centrality trigger) improved the available statistics, and particle spectra for peripheral collisions can now be obtained with reasonable statistical errors. The centrality cuts based in multiplicity alone are not good for the peripheral collisions (see section 1.2.1). Better control on the impact parameter (and N_{bin}) could be achieved by defining centrality from the ZDC–MA energy correlation. Evaluating the number of participants or the number of binary collisions with this centrality definition requires modeling of the fragmentation of the spectator compound and simulation of the deflection of the fragments in the magnetic field of the DX magnets.

In the $d+Au$ data reconstruction, the centrality is also determined from the MA charged particle multiplicity. Here the multiplicity–impact parameter correlation (or the centrality–N_{bin} correlation) is broader than in the $Au+Au$ collisions. A better handle on impact parameter (or N_{bin}) could be obtained by defining the centrality from the measurement of charged particle multiplicity in BBC on the gold fragmentation side. Including the number of neutrons detected in the left ZDC (on the gold fragmentation side) would further improve the correlation. Also, the signal in the right ZDC (in the direction of the deuteron beam) could be used to tag $p+Au$ events.

The uncertainty on the centrality determination comes from the uncertainty in the MB trigger efficiency and from the finite statistics and binning of the distribution from which the centrality is defined. Since the event samples typically contain millions of events the latter can be neglected. In practice, the uncertainty comes solely from the uncertainty in the MB trigger efficiency. This means, that if the MB trigger was 100% efficient there would be no uncertainty on the centrality, since it is defined as cuts in a measured distribution corresponding to fractions of the total integral. If the MB trigger efficiency is $95 \pm 3\%$, the centralities of, for example, 80%, 50% and 10% would be $80^{+2.6}_{-2.4}\%$, $50^{+1.6}_{-1.5}\%$ and $10^{+0.3}_{-0.3}\%$.

4.2 Track Reconstruction

The trajectories of charged particles are reconstructed in the tracking detectors. These track segments are called *local tracks*. The local tracks in two tracking detectors located on either side of a magnet are then matched in order to determine the particle trajectory through the magnet gap. From the deflection of the track in the magnetic field, the momentum to charge ratio of the particle can be determined. In the MRS and FFS, the matched tracks (TPM1–D5–TPM2 or T1–D2–T2) are called global tracks. In the FS, the different matched tracks are combined to full (global) FS tracks. Finally, the vertex of the global tracks (both in MRS and in FS) are determined.

4.2.1 Local Tracking

As a charged particle traverses a tracking chamber, the gas ionization along the trajectory induces signals that can be converted into spacial points or hits. The local tracking algorithm combines these hits and identifies the tracks. The subsequent fit to the hit positions gives the final three dimensional track segments in the chamber, i.e. the local tracks. The local tracking algorithm for the TPCs is described in ref. [86].

4.2.2 Track Matching

The local tracks (each defined by a space point and a direction) are matched in the magnet gap and the deflection angle is used to calculate the momentum to charge ratio. Before turning to the details on how the matching is done, the geometry and the calculation of the matched track momentum is described.

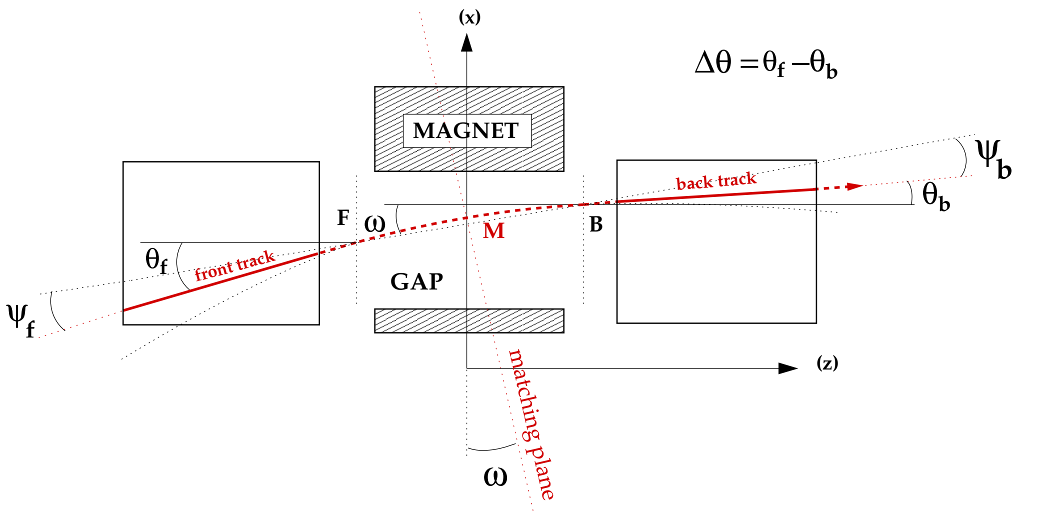

Figure 4.4: Top view of the matching geometry: tracking detector – magnet – tracking detector. F and B denotes the intersection point between the track and the effective edges of the magnetic field. The matching is done by comparing ψ_f and ψ_b which are the angle differences between the local tracks (front and back) and the line $|FB|$ in the $x-z$ plane. If the local tracks match (originate from the same particle), they should fulfill $\psi_f = \psi_b$.

The track matching uses the effective edge approximation for the magnetic fields, i.e. that the magnetic field inside a magnet is homogeneous and only has a $y-$component implying that the deflection only occurs in the $x-z$ plane. The momentum of a track in the $x-z$ plane is given by $p_{xz} = qB\rho$, where q is the charge of the particle, B is the magnetic field and ρ is the radius of the helicoidal trajectory in the magnetic field.
Figure 4.4 shows a schematic top view of two tracking detectors and the intervening magnet. The variables used in the following are defined in the figure. Figure 4.5 shows the same matching geometry seen from the side.

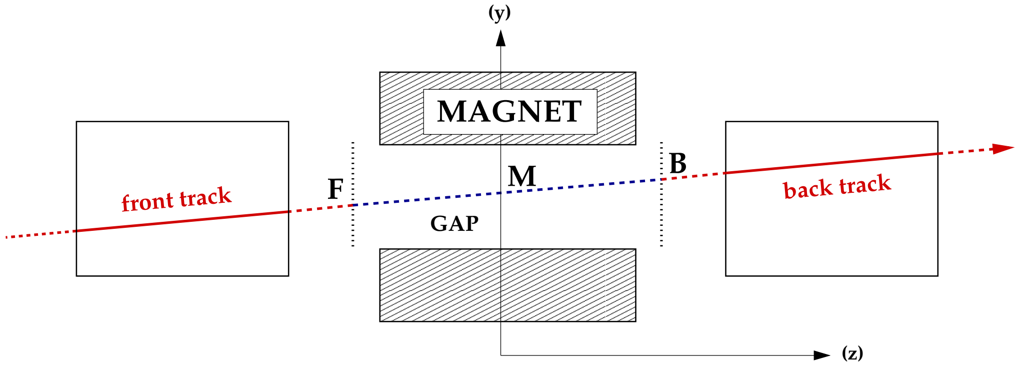

Figure 4.5: Side view of the matching geometry.

From simple trigonometry, it follows that the radius of the bending arc is

$$\rho = \frac{\Delta L}{\sin\theta_f - \sin\theta_b}. \tag{4.2}$$

Here, ΔL denotes the length of the magnetic field in the $z-$direction, i.e. the distance in z between the effective edges. The momentum component in the $x-z$ direction can now be obtained:

$$p_{xz} = \frac{qB\Delta L}{\sin\theta_f - \sin\theta_b}. \tag{4.3}$$

The full momentum is calculated by taking the $y-$component of the track into account. Using Pythagoras's rule ($p^2 = p_{xz}^2 + p_y^2$) and the measured $y-$slope of track (α_y) one gets

$$p = \frac{qB\Delta L}{\sin\theta_f - \sin\theta_b}\frac{1}{\sqrt{1-\alpha_y^2}}. \tag{4.4}$$

Ideally, the local tracks originating from the same particle should have the same $y-$slope ($\Delta\alpha_y = 0$), and point directly to each other in the y-direction, i.e point to the same y in the matching plane of the magnet ($\Delta y = 0$). Furthermore they should fulfill $\Delta\psi = \psi_f - \psi_b = 0$ (ψ_b and ψ_f are defined in figure 4.4). Due to finite angular resolution of the tracking chambers, effects from multiple scattering of the particles, slight offsets in the detector geometry and the effect of using the effective edge approximation, these conditions are not fulfilled. The track matching allows the matching parameters $\Delta\psi$, $\Delta\alpha_y$ and Δy to vary from the ideal. This is expressed in the matching condition:

$$\left(\frac{\Delta\psi - \Delta\psi_{off}}{\sigma_{\Delta\psi}}\right)^2 + \left(\frac{\Delta\alpha_y - \Delta\alpha_{off}}{\sigma_{\Delta\alpha_y}}\right)^2 + \left(\frac{\Delta y - \Delta y_{off}}{\sigma_{\Delta y}}\right)^2 < n^2 \tag{4.5}$$

The offsets $\Delta\psi_{off}$, $\Delta\alpha_{off}$ and Δy_{off} are due to slight mis–alignment of the detectors. The widths of the $\Delta\psi$, $\Delta\alpha_y$ and Δy distributions are assumed to be Gaussian and $\sigma_{\Delta\psi}$, $\sigma_{\Delta\alpha_y}$ and $\sigma_{\Delta y}$ are the respective widths of these distributions (one standard deviation). The offsets and widths are determined for each run, before the actual matching is performed. n is the number of standard deviations allowed for a pair of tracks before they are matched (normally, $n = 3$). This procedure is not optimal since the resolution of the matching parameters depends on the particle momentum (which is not taken into account in equation 4.5). As will be described in the next section $\Delta\psi$ is larger for low momentum particles. The measured spectra are typically fast decreasing with momentum and the widths of the matching parameter distributions are therefore dominated by the lowest momentum particles in the particular magnetic field setting. This means that width of the cut (σ) is dominated by the width in the low momentum range and is therefore too wide for particles with higher momenta.

Magnet Fiducial Cuts

Fiducial cuts in the magnets are introduced in order to leave out tracks that could have originated from secondary production in the magnet iron. If the helix of a matched track in the magnetic field is closer than some distance δ to the magnet iron, the track is not considered in the analysis. The value of δ is set to 1 cm for D2, D3, D4 and D5 and 0 cm for D1. The typical distance from the reconstructed track helix to the *true* track helix could be estimated from the local track angular and spacial resolutions. From this estimation the magnet fiducial cuts could be optimized.

4.2.3 Global Tracking

The global tracks are tracks that are reconstructed through the full spectrometer – MRS, FFS or the full FS. The global tracks are assigned a vertex, a momentum and a direction (at the vertex).

In the MRS, a matched track (TPM1–D5–TPM2) is a global track. The intersection between the TPM1 local track line with the $y - z$ plane of the beam is defined as the track vertex. The TPM1 local track line defines the direction of the track while the D5 matching defines the momentum to charge ratio, see equation 4.4. In the final analysis it is required that the track vertex is within some distance of the collision vertex (see section 5.2).

In the FFS the T1–D2–T2 matching gives the track momentum. The position and direction of the local T1 track and the momentum is used to determine the track helix through D1. From the position and direction of the track at the D1 entrance the track intersection with the beam plane can be found. The beam plane is, for FFS/FS tracks, defined as the $x - y$ plane with z as the reconstructed collision vertex z. The geometry and MRS/FS vertex planes are illustrated in figure 4.6.

To obtain full FS track, the FFS track reconstruction and the BFS track reconstruction are done separately. The BFS tracking matches the T3–D3–T4 matched tracks with the T4–D4–T5 matched tracks by requiring that they have the same T4 track. The BFS tracks (T3–D3–T4–D4–T5) are matched with the FFS track by introducing a T2–T3 matching. The principle of this matching is the same as that described in equation 4.5, only here, the matching variables are Δx, $\Delta\alpha_x$ Δy and $\Delta\alpha_y$. A FS track re–fitting procedure [93] has been used in reconstruction of runs after 2002. The re–fitting starts with the T1 local track (position and direction) and the average momentum ($p_{av} = (p_{D2} + p_{D3} + p_{D4})/3$). It performs a *minuit* fit, varying the momentum and the $y-$slope. The χ^2 is calculated from difference in the local track positions in the other tracking detectors. When the best (lowest χ^2) momentum and angle is determined, the track is extrapolated back through D1 to find the track vertex and angle.

4.2.4 Angular and Momentum Resolution

The angular resolutions of the tracking detectors are important for the determination of the track angle θ, i.e. the emission angle of the particle, and for the momentum determination (that comes from the bending angle $\Delta\theta$). The resolution of the angle have two components: one comes from the angular resolution of the tracking detector, the other one comes from the multiple Coulomb

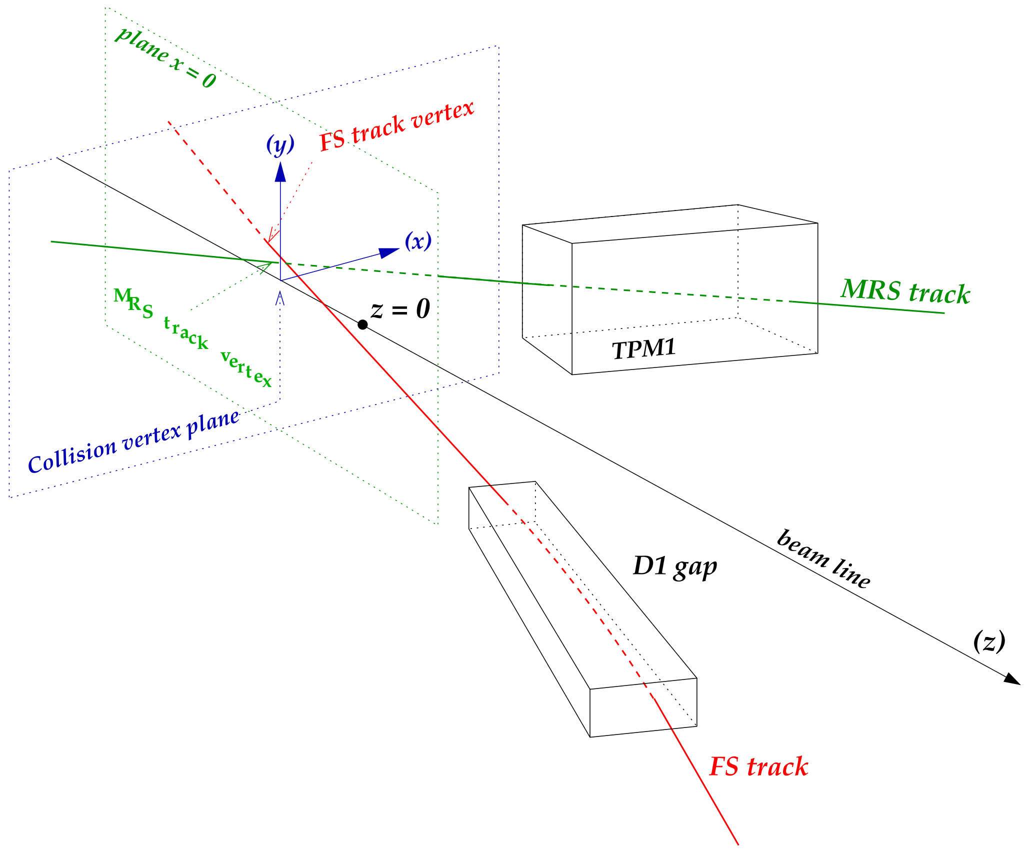

Figure 4.6: Global track vertex. For the MRS global tracks the vertex is defined as the track intersection with the $y-z$ plane ($x = 0$) of the beam. In the FFS/FS the global track vertex is defined as the track intersection with the $x-y$ plane defined by the collision vertex $z = vtx_z$ (measured by BBC, ZDC or INEL).

scattering that the particles undergoes in the traversed medium. In the forward spectrometer (FFS or FS), the momentum resolution also has an effect on the track angle resolution, since it is used in the calculation of the deflection of the particle trajectory in D1.

In the following, the angular distortion due to multiple scattering is described. Next, the resolution of the track bending angle is evaluated – this is important for the momentum resolution, which is discussed in the following section. Finally, the resolution of the track angle θ is evaluated.

Multiple Scattering

Charged particles traversing a medium are deflected by random multiple Coulomb scattering on the nuclei in the medium. For small angle deflection the angular smearing roughly follows a Gaussian of width

$$\sigma_{\theta_{ms}} = \frac{0.0136\,\mathrm{GeV/c}}{\beta p} z \sqrt{x/X_0}\,(1 + 0.038\ln(x/X_0))\,, \tag{4.6}$$

where z is the charge of the particle and x/X_0 is the thickness of the traversed medium relative to the radiation length of the medium [94]. In the following the effect of multiple scattering will simply be written $\sigma_{\theta_{ms}} = K/(\beta p)$, where K is the multiple scattering angle deflection parameter. The parameter K is estimated from the radiation lengths of the traversed medium. Table 4.1 lists the estimated K for the different spectrometer sections.

Section	L_{air} [m]	L_{Be} [cm]	x/X_0	$K \times 10^{-3}$[GeV/c]
VTX–TPM1	0.8	$0.12 - 0.24$	$0.029 - 0.033$	$2.0 - 2.2$
TPM1–TPM2	1.5	0	0.049	2.7
VTX–T1	4.8	$0.24 - 2.29$	$0.165 - 0.223$	$5.2 - 6.1$
T1–T2	2.4	0	0.079	3.5
T2–T3	2.1	0	0.069	3.2
T3–T4	3.0	0	0.099	3.9
T4–T5	2.9	0	0.095	3.8

Table 4.1: Lengths, radiation lengths and the angular smearing width from multiple scattering in the different spectrometer sections. The calculation only includes the air ($X_0 = 30.42$ m) and the beryllium ($X_0 = 0.3528$ m) beam pipe traversed. Tof walls, TPC entrance and exit windows, C1 and trigger slats are not included.

Bending Angle Resolution

The resolution of the bending angle measurements in a magnet depends on the angular resolution of the tracking detectors. The bending angle resolution $\sigma_{\Delta\theta}$ is given by $\sigma^2_{\Delta\theta} = \sigma^2_{\theta_{ms}} + (\sigma^2_{\theta_f} + \sigma^2_{\theta_b})$, where σ_{θ_f} and σ_{θ_b} are the angular resolutions of the tracking detectors in front and behind the magnet. The multiple scattering term $\sigma^2_{\theta_{ms}}$ was described in the previous section. In the following, ways to estimate the tracking angle resolution are described.

The angular resolution of the tracking detectors can be estimated from the typical number of hits and the spacial resolution σ_x of these. Assuming that the track is measured at N points separated by l along the trajectory the angular resolution can be found from linear regression

$$\sigma_{\theta_{track}} = \frac{\sigma_x}{l}\sqrt{\frac{12}{N(N^2-1)}}. \tag{4.7}$$

Typical numbers for the TPCs are $\sigma_x = 0.03 - 0.05$ cm, $l = 5$ cm and $N = 8 - 12$ which gives $\sigma_{\theta_{track}} \approx 0.001$ mrad.

The combined tracking angle resolution of two tracking detectors (which gives bending angle resolution $\sigma_{\Delta\theta}$) can be also be estimated from the data. This can be done in two different ways: from the track matching in runs where the field is off (zero–field runs) and from the matching angle parameter $\sigma_{\Delta\psi}$.

When the magnetic field in a magnet is off (zero–field runs), the spread in difference between the track angles in two detectors is the (combined) bending angle resolution of the two detectors, assuming that the multiple scattering is negligible. This assumption is reasonable in the FFS/FS when the D1 magnet has a high field (and D2–D4 are off), so that the particles have a high average momentum. In the MRS this method cannot be used, since the effect of multiple scattering smears out the distribution. The results of fits to distributions of difference in angle for the T1–T2 and T4–T5 are listed in table 4.2. Note that these numbers are consistent with the rough estimation of the TPC angular resolution.

The angular resolution of the tracking detectors can also be obtained from the width of the matching angle parameter resolution $\sigma_{\Delta\psi}$, which can be fitted from non–zero–field runs. The resolution of the matching angle parameter is however not the same as the resolution of the bending angle $\sigma_{\Delta\theta}$. The relation between $\sigma_{\Delta\psi}$ and $\sigma_{\Delta\theta}$ is derived in appendix C. It is found that

$$\sigma^2_{\Delta\psi} \approx \sigma^2_{\theta_{f+b}}\left(1 + \left(\frac{2L}{L_{mag}}\right)^2\right), \tag{4.8}$$

where L is the distance between the middle of the tracking chamber and the effective edge of the magnet – it is assumed that it is approximately the same on both sides of the magnet. L_{mag} is the

length of the effective magnetic field in the $z-$direction (equal to ΔL in equation 4.4). Estimates of the width of the matching parameter ψ and other magnet/matching characteristics are listed in table 4.2.
Including the multiple scattering in the bending angular resolution gives

$$\sigma^2_{\Delta\theta} = \left(\frac{K^2}{\beta^2 p^2}\right) + \sigma^2_{\theta_{f+b}} \tag{4.9}$$

Figure 4.7 shows the width of the track matching parameter as function of track momentum in D5 for a low field setting. In the FS, the momentum is typically too high to extract K from such fits, i.e. $\sigma_{\Delta\theta}$ is practically independent of momentum.

Section	$B\Delta L$ [Tm]	$\sigma_{\Delta\psi} \times 10^{-3}$ [mrad]	L [cm]	L_{mag} [cm]	$\sigma_{\theta_{f+b}} \times 10^{-3}$ (z.f.) [mrad]	$\sigma_{\theta_{f+b}} \times 10^{-3}$ [mrad]
TPM1–D5–TPM2	1.15	5.12 ± 0.54	59.2	83.6	-	2.95 ± 0.31
T1–D2–T2	2.95	2.15 ± 0.37	75.9	160	1.58	1.56 ± 0.27
T3–D3–T4	2.64	0.97 ± 0.01	87.2	200	-	0.73 ± 0.01
T4–D4–T5	2.48	0.84 ± 0.07	85.9	183	1.01	0.61 ± 0.05

Table 4.2: Track matching characteristics. The values for $\sigma_{\Delta\psi}$ are the mean of five fits to different data sets in the high momentum range where the effect of multiple scattering is expected to be negligible. In the MRS a more detailed fit that takes the multiple scattering effect into account was used (see figure 4.7). In the FS the $\sigma_{\theta_{f+b}}$ can also be estimated from zero–field (z.f.) runs (with the D1 magnet on) from the difference between the angles. The $B\Delta L$ for D1 is 2.64 Tm.

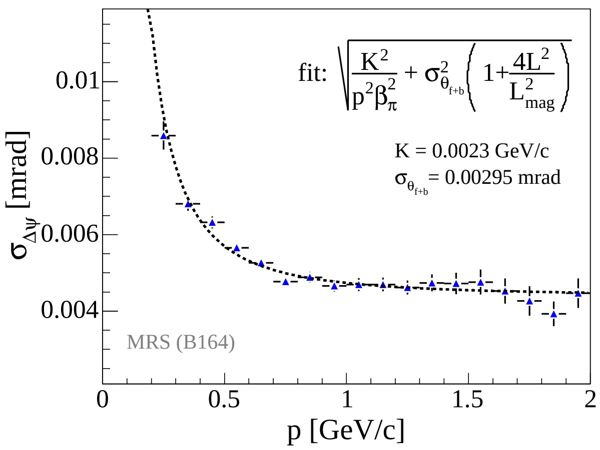

Figure 4.7: Fit to matching parameter $\sigma_{\Delta\psi}$ for D5 in a low field setting. The particles are all assumed to be pions. The effect of multiple scattering is clear at low momentum.

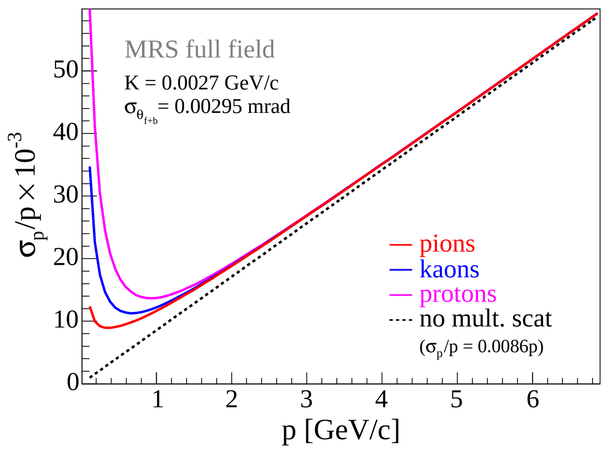

Figure 4.8: Relative momentum resolution as function of momentum in the MRS. If the multiple scattering is neglected the relative momentum resolution is approximately 1% at full field.

Momentum Resolution

The resolution on the momentum determination from one spectrometer section, e.g. T1–D2–T2, can be estimated using the small angle approximation of equation 4.4, where $p = 0.3B\Delta L/\Delta\theta$ – here the charge of the particle is set to one and the factor 0.3 comes from the conversion of the units ($[p]$ = GeV/c, $[B\Delta L]$ =Tm=Ns/Cm and the charge $q = 1.6 \times 10^{-19}$ C). The momentum resolution can be expressed as

$$\frac{\sigma_p^2}{p^2} = \frac{\sigma_{\Delta\theta}^2}{\Delta\theta^2} = \sigma_{\Delta\theta}^2 \frac{p^2}{(0.3B\Delta L)^2} = \left(\frac{K^2}{\beta^2 p^2} + \sigma_{\theta_{f+b}}^2\right) \frac{p^2}{(0.3B\Delta L)^2}, \tag{4.10}$$

which gives

$$\sigma_p^2 = \frac{1}{(0.3B\Delta L)^2} \left(\frac{K^2 p^2}{\beta^2} + \sigma_{\theta_{f+b}}^2 p^4\right). \tag{4.11}$$

Figure 4.8 shows the relative momentum resolution σ_p/p as function of momentum in the MRS where the magnetic field is the maximum.
Equation 4.11 can be used in the MRS and FFS, since the momentum is only determined in one matching. In the full FS the momentum resolution is more complicated to estimate, since the momentum is calculated as an average between different non–independent momentum determinations (the D3 and D4 momentum shares the T4 local track) or determined from the FS track re–fitting (see section 4.2.3). An accurate determination of the momentum resolution could be obtained by Monte Carlo simulation.

Rough limits on the combined momentum resolution in the FS can be obtained by assuming that the momentum is determined in two or three independent measurements and that these measurements have similar resolutions. Assuming two independent measurements gives the absolute upper limit, since it neglects one of the BFS measurements. Assuming three independent measurements sets a lower limit. The limits are obtained by using the average parameters of $\sigma_{\theta_{f+b}}$ and K for the different segments, inserting equation 4.11 and by dividing the result (σ_p) by $\sqrt{2}$ or $\sqrt{3}$.

Track Angle Resolution

In the MRS the resolution of the track angle measurement can be written

$$\sigma_{\theta_{MRS}}^2 = \frac{K_{VTX-TPM1}^2}{\beta^2 p^2} + \sigma_{\theta_{TMP1}}^2. \tag{4.12}$$

Assuming that the angular resolution of TPM1 is 4.2×10^{-3}mrad (a factor $\sqrt{2}$ higher than the combined TPM1–TPM2 bending angle resolution), and that $K \approx 0.003\,\mathrm{GeV/c}$, the angular resolution is better than half a degree for protons with $p > 0.5\,\mathrm{GeV/c}$.
In the FFS/FS, the track angle resolution is affected by the multiple scattering, the T1 angular resolution and the momentum resolution. The contribution from the momentum resolution on the track angle resolution is estimated in the following way. In the small angle limit of equation 4.4 the momentum can be written $p = B\Delta L/\Delta\theta$, which implies that the relative error on the momentum is the same as the relative error on the bending angle, $\sigma_p/p = \sigma_{\Delta\theta}/\Delta\theta$.

The two contributions to the track angle resolution (from the angular resolution in T1 and from the momentum resolution) are correlated since the local T1 tracks are used in both measurements. Assuming that the correlation imposes a second order effect one can estimate the angular resolution in the FFS

$$\sigma_{\theta_{FFS}}^2 = \frac{K_{D1}^2}{\beta^2 p^2} + \sigma_{\theta_{T1}}^2 + \frac{(0.3B_{D1}\Delta L_{D1})^2}{p^2}\frac{\sigma_p^2}{p^2} \tag{4.13}$$

$$= \frac{K_{D1}^2}{\beta^2 p^2} + \sigma_{\theta_{T1}}^2 + \frac{(B_{D1}\Delta L_{D1})^2}{(B_{D2}\Delta L_{D2})^2}\left(\frac{K_{D2}^2}{\beta^2 p^2} + \sigma_{\theta_{T1+T2}}^2\right) \tag{4.14}$$

The values of K_{D1}, K_{D2}, $B\Delta L$ and $\sigma_{\theta_{T1+T2}}$ are listed in tables 4.1 and 4.2. It can be assumed that the local track angle resolution for T1 and T2 is similar ($\sigma_{\theta_{T1}}^2 = 2\sigma_{\theta_{T1+T2}}^2$). Note that the track angle resolution does not depend on the strength of the magnetic fields, only the relative value of the $B\Delta L$ in D1 and D2, which (in the standard field settings) is 2.62/2.95. The momentum resolution increases for lower field settings (or higher momenta), but the extrapolation back through D1 gets equally more precise since the bending angle gets smaller.

In FS a similar approach can be used, using the rough approximations for the momentum resolution explained in the last section. However, if the FS track re–fitting (see section 4.2.3) is used, the angular resolution is expected to be better – instead of the local T1 track (with angular resolution $\sigma_{\theta_{T1}}$), the position and direction of the global re–fitted track is used in the extrapolation back through D1.

Transverse Momentum Resolution

The resolution of the measured transverse momentum ($p_T = p\sin\theta$) can be found from propagation of the angular resolution and the momentum resolution

$$\sigma_{p_T}^2 = \left(\frac{\partial p_T}{\partial p}\sigma_p\right)^2 + \left(\frac{\partial p_T}{\partial \theta}\sigma_\theta\right)^2 = (\sin\theta)^2\sigma_p^2 + p^2(\cos\theta)^2\sigma_\theta^2. \tag{4.15}$$

From this equation it is obvious that the resolution of the measured transverse momentum around mid–rapidity ($\theta \sim 90°$) is dominated by the momentum resolution, while at small angles it is dominated by the angular resolution. An uncertainty in the measured p_T smears the p_T spectrum, i.e. the measured spectrum are distorted compared to the *true* spectrum. The magnitude of this effect is estimated in section 5.4.4.

4.3 Particle Identification

Particle identification in BRAHMS is done by a combination of Cherenkov and time–of–flight techniques. The common approach is, for a given particle, to measure the momentum and the velocity or a quantity that depends on the velocity, i.e. the time–of–flight or the emission of Cherenkov light. In the following sections, the reconstruction and PID methods for the C1 and RICH detector are described.

The PID using the time–of–flight method is done by measuring the flight time of a given particle, i.e. the time from the collision occurs to the time the particle hits the time–of–flight wall. The path length is known and the velocity β of the particle can be calculated. From the velocity and the momentum of the particle, the mass–squared can be found, $m^2 = p^2(1/\beta^2 - 1)$. The PID selection is done in mass–squared as function of momentum. The width of the mass–squared $\sigma_{m^2}(p)$ is found from error propagation, including the error on the time measurement σ_t and the error on the momentum

$$\sigma_{m^2}^2 = 4\left[\frac{m^4 p 2\sigma_{\theta_{ang}}^2 + m^4\left(1+\frac{m^2}{p^2}\right)c}{(0.3B\Delta L)^2} + (m^2+p^2)^2\sigma_t^2\right]. \tag{4.16}$$

Figure 4.9 shows an example of measured mass–squared as function of momentum. The curves indicate $\pm 2\sigma_{m^2}$ around the *true* mass–squared for pions, kaons and protons. Fitting the $\sigma_{m^2}(p)$ as function of momentum [81] gives values of $\sigma_{\theta_{ang}}$ and K that are consistent with the ones quoted in tables 4.1 and 4.2.

4.4 The Cherenkov Reconstruction

The BRAHMS Cherenkov detectors utilizes the fact that charged particles traversing a medium with a velocity that is higher than the speed of light in the medium emit Cherenkov radiation. This speed

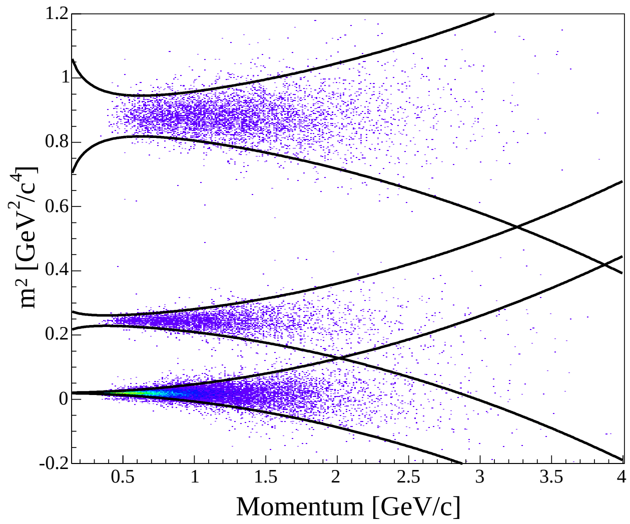

Figure 4.9: Example of mass–squared as function of momentum measured in the MRS (using TOFW). The curves indicate $\pm 2\sigma_{m^2}$ PID cuts around the pions, kaons and protons..

is given by $v = c/n$, where n is the refractive index of the medium. The radiation is emitted in a well defined angle (the Cherenkov angle θ_C), given by

$$\cos\theta_C = \frac{1}{\beta n}. \tag{4.17}$$

and the number of photons emitted is given by

$$N_\gamma = N_0 L \sin^2\theta_C, \tag{4.18}$$

where N_0 depends on the properties of the radiator medium and the detection efficiency and L is the length of the traversed medium (the radiator length).

These formulas are approximations that do not take into account the wave length dependence of the refractive index. However, the photon frequency bandwidths (λ window) of the BRAHMS Cherenkov detectors make the dependence of the wave length negligible. More details on Cherenkov radiation can be found in ref. [94].

Thanks to Cherenkov radiation, the threshold Cherenkov detectors (C1 and C4) and the Ring Imaging Cherenkov detector (RICH) can separate/identify particles of different masses.

The emission of Cherenkov radiation depends only on the velocity of the particle and the velocity threshold therefore gives different momentum thresholds for particles of different masses. Whether a particle of a certain momentum emits Cherenkov radiation or not therefore depends on the mass of the particle. The threshold Cherenkov detectors measures whether a particle emits Cherenkov radiation or not, which is used to separate pions from kaons/protons above the pion and below the kaon momentum threshold, and to separate protons from pions/kaons above the kaon and below the proton momentum threshold. The more sophisticated RICH measures directly the Cherenkov angle θ_C, from which, when combined with the momentum, the mass–squared can be derived.

4.4.1 C1 Reconstruction

The Cherenkov light emitted in the C1 radiator volume is reflected on two flat mirrors in the back of the detector and measured by an array of PM tubes (see figure 4.10). If the mirrors were not there, the emitted light would form a homogeneous disk on the back plane of the detector. In the reconstruction algorithm, the two sensitive plane are treated as if they were placed on the back plane of the detectors. The 45 degree inclination of the mirrors justifies this simplified treatment. The

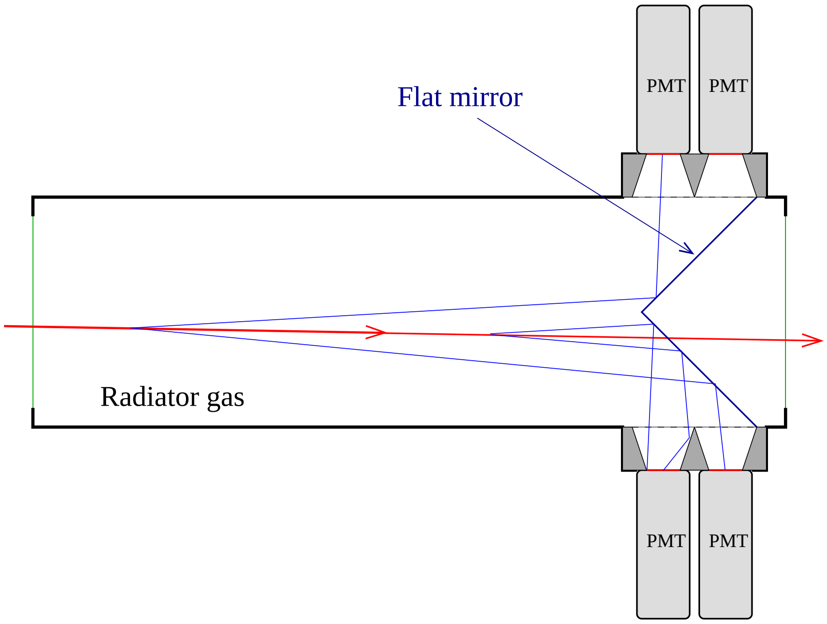

Figure 4.10: Side view of C1. The emitted Cherenkov photons are reflected on the two 45° mirrors and measured by arrays of PM tubes. The red line shows a particle track through the detector and the blue lines indicate the photon reflection on the mirrors.

center of a possible light disk is calculated as the intersection between a track and the back plane of the detector. The momentum of the particle is known and the expected radius r of the disk is calculated assuming the particle is a pion ($r = L \tan \theta_C$).

The number of photons is the sum of the (calibrated) signals in the tubes whose sensitive areas have an overlap with the disk. This is illustrated in figure 4.11.

If there are two tracks with momentum above the pion Cherenkov threshold and the two disks overlap with the same tube, the algorithm tries to separate the two signals. This is done by looking at the signal in the tubes that overlap with both disks. If the sum of the signals in these tubes is less than 50% of the sum of the signals in the tubes of one of the disks, the disks are separated. In this case the number of photons is set to the number of photons measured in the tubes that are not *shared*, scaled with the relative area of disk outside the overlap.

Figure 4.12 shows the number of measured photons as function of momentum. The energy distribution from a single photon has a certain width (typically around half of the mean value), which smears out the signal from a particle above threshold somewhat. In contrast to the other PID detectors, C1 has a high rate (up to 35%) of mis–identification, e.g. protons below threshold gives large signals because of *noise* in the detector. Especially in the $Au + Au$ data, the background rates are quite high. Using the C1 in analysis therefore requires extensive simulation of the detector response.

4.4.2 RICH Reconstruction

The RICH reconstruction algorithm requires reconstructed tracks in the BFS and looks for ring images in the photon detector plane (image plane). The ring finding algorithm uses information on the track direction and momentum in the search for rings. The algorithm looks for rings of any radii, even though only certain radii are allowed for a particle of a certain momentum, i.e. the radii corresponding to the different particle species. Such a simple algorithm (that does not use the expected radii) does not favor any radii, which simplifies the evaluation of the performance. Before turning to the ring finding algorithm the basic principles of the RICH are described.

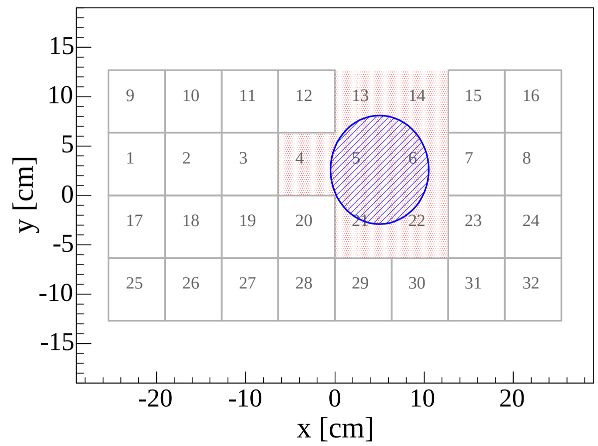

Figure 4.11: Outline of the sensitive plane of C1. The signal corresponding to a track is the sum of the signals in the tubes that has an overlap with the disk.

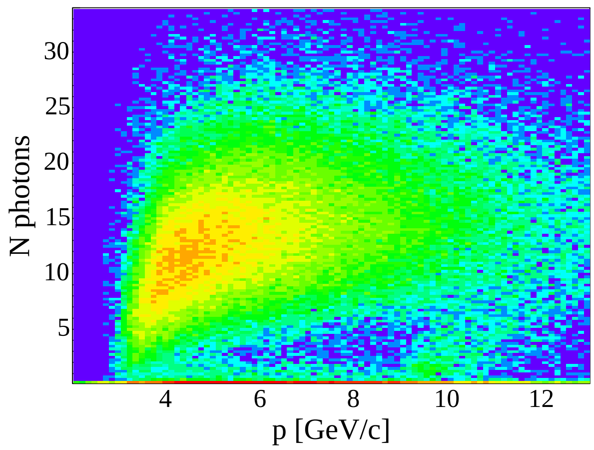

Figure 4.12: Example of the number of photons as function of momentum. The pions and kaons starts to give signals slightly above the threshold.

The Basic Principle of the RICH

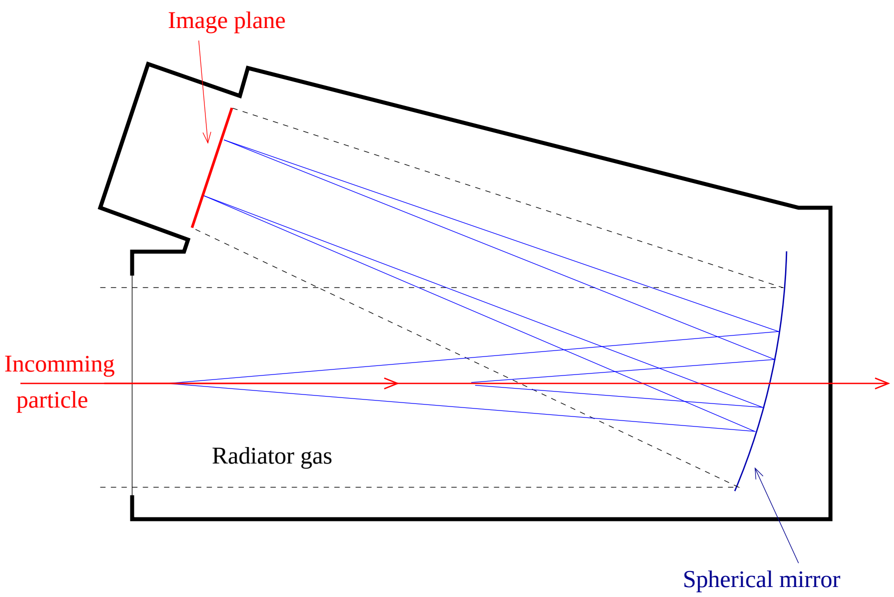

Figure 4.13: Side view of the RICH. The emitted Cherenkov photons are reflected on the mirror and form a ring image on the sensitive image plane. The red line shows a particle track through the detector and the blue lines indicate the photon reflection on the mirror.

The charged particles traverse the radiator ($L \approx 150\,\mathrm{cm}$) where the Cherenkov light is emitted. A spherical focusing mirror in the back of the detector reflects the emitted Cherenkov light. Photons with certain incoming angles are reflected onto certain points on the RICH image plane. This means, that a cone of photons emitted with the same angle θ_C relative to the particle trajectory (but with random azimuthal angle) are focused to a circle (or ring) on the image plane. Examples of ring images are shown in figure 4.15. The center of a ring is fixed according to the trajectory angle of the particle that emits the Cherenkov light. The ring radius r is related to the Cherenkov angle

$$\tan\theta_C = \frac{r}{L_{foc}}, \tag{4.19}$$

where $L_{foc} = 150\,\text{cm}$ is the focal length of the spherical mirror. Figure 4.13 shows a schematic side–view of the detector and the photon reflection on the mirror. The image plane is $26\,\text{cm} \times 21\,\text{cm}$ and has 320 photon detectors (cells).

Ring Finding Algorithm

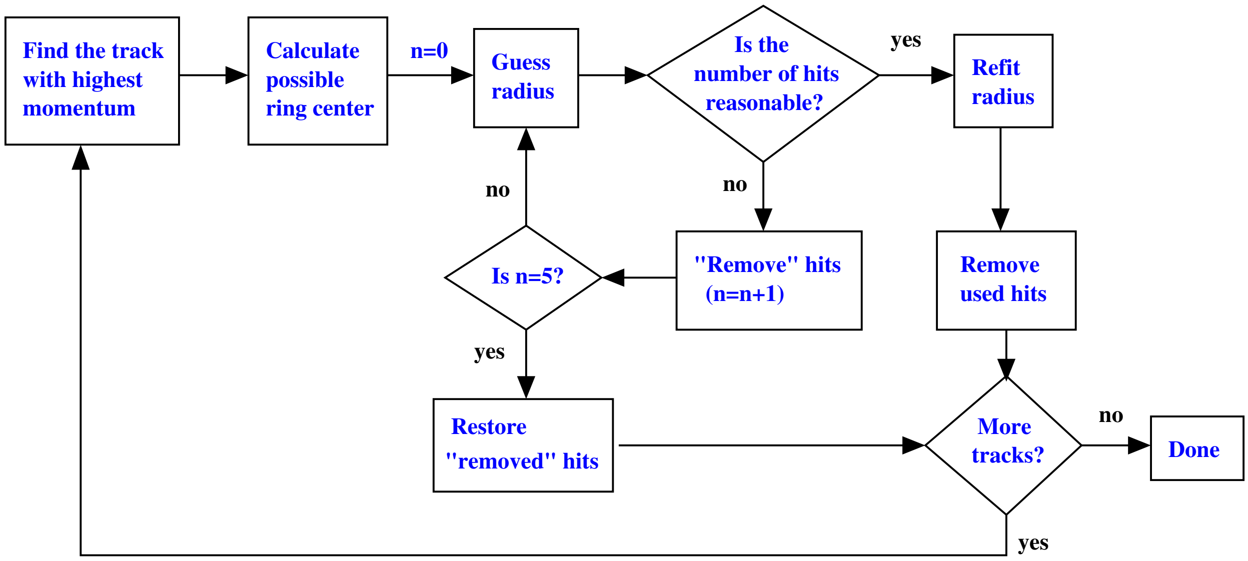

Figure 4.14: Flow diagram of the ring image finding algorithm.

A flow diagram of the ring finding algorithm is depicted in figure 4.14. The procedure is as follows:

- Find the track with the highest momentum: The algorithm starts with the reconstructed BFS tracks. In the case of more than one reconstructed BFS, the algorithm processes the one with the highest momentum first, since this is the one that is most likely to *produce* a ring.
- Calculate ring center: From the track direction the center of a possible ring can be determined by reflecting the track line on the spherical mirror. This is done by finding the track line intersection with the mirror and reflecting the track line around the line that connects the track–mirror intersection and the center of the mirror sphere. The reflected line intersection with the image plane is found – this is the center of a possible ring.
- Guess radius: The number of hit tubes that falls within a ring defined by $r \pm \Delta r$ is now counted for different values of r. The default value of Δr is set to $2\,\text{cm}$. The number of hit tubes as function of r is stored in a histogram, see figure 4.16. A ring image shows up as a peak in the histogram. The maximum of the histogram is found and the peak is fitted with a gauss. The mean of the fit is the guessed radius r_{guess}.
- Is the number of hits reasonable?: The number of emitted photons depends on the velocity of the particle and is therefore related to the radius. A reconstructed ring with a large radius and few hits is therefore not expected to originate from a fast particle, but rather from noise in the detector. The minimum expected number of detected photons is calculated from the expected number of emitted photons and an estimate of the reflection and detection efficiencies. This is compared to the number of hits in the ring image (i.e. the number that falls within $r_{guess} \pm \Delta r$). If the number of hits is equal or higher than the minimum number of expected photons, the ring is accepted. Since the number of hits can saturate, because of the finite segmentation of the image plane, rings with more than seven hits are always accepted. If the number of hits in

the ring is lower than the minimum expected the hits are disregarded (”removed”) when the next radius *guess* is made. If no rings with a reasonable number of hits are found after five radius guesses, the ”removed” hits are restored and the algorithm starts over in case of more tracks.

- Refit radius: The radius of the accepted ring is now set to the average radial distance of all the hits in the ring. The hits used in the ring are marked and left out if the algorithm tries to find rings for another track.

- More Tracks? If there are more tracks, the algorithm starts over again.

Figure 4.17 shows the reconstructed ring radius as function of particle momentum. The ring finding algorithm can be improved. The most important improvements are: **1)** The estimated number of hits could include a saturation function that takes into account the probability of two (randomly emitted) photons hitting the same tube. **2)** The refit of the radius is done using the centers of the hit tubes – this leads to a slight overestimation of the radius, since the ring intersect more cells with the cell middle outside the ring than cells with the middle inside the ring. **3)** the hits are removed as the algorithm goes to the next track. This means that *double* hits that lie on two ring images are only used on one of the rings.

However, the overall performance of the detector is good. The efficiency has been estimated to be around 97% [86].

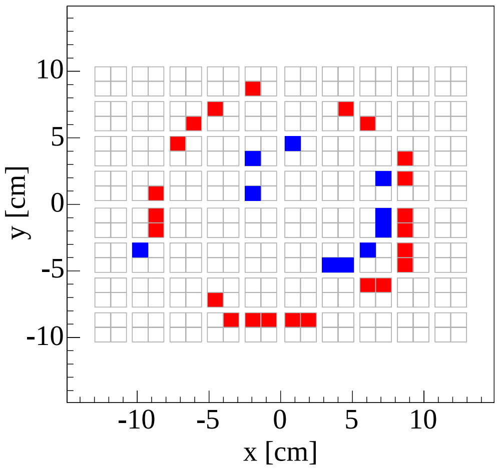

Figure 4.15: Example of ring images. The blue and the red hits are from two different events. The blue ring is from a proton with momentum of 17 GeV/c. The red ring is from a 20 GeV/c pion.

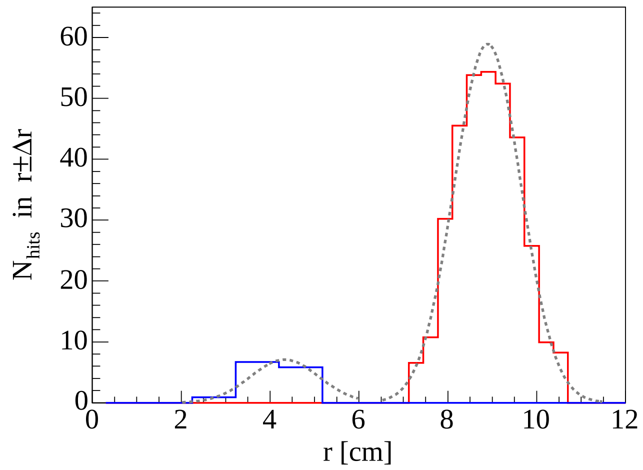

Figure 4.16: The number of hits in a ring $r \pm \Delta r$. A ring shows up as a peak in the distribution. This is used to guess a radius. The binning of the histogram is smaller than $2\Delta r$ – this is why the *number of hits* in the red histogram is larger than the 23 found in figure 4.15.

Radius Resolution

The resolution of the measured ring radius is important for the PID. The ring radius is a fit to N measured hits on the ring, each with a spacial resolution of approximately $\Delta t/\sqrt{12}$ where Δt is the size of the tubes. This gives a radius resolution of $\sigma_r = \Delta t/\sqrt{12N}$. Assuming no fluctuation in the number of detected photons and that the segmentation of the image plane is so high that effects from saturation of the number of hits can be neglected, σ_r reads

$$\sigma_r = \frac{\Delta t}{\sqrt{12 N_0 L} \sin\theta_C} = \frac{\Delta t}{\sqrt{12 N_0 L(1 - 1/(\beta^2 n^2))}}. \tag{4.20}$$

Particle Identification using the RICH

The particle identification can be done from the reconstructed mass–squared. From equation 4.19 and the fact that $\beta^2 = 1 + m^2/p^2$, the mass–squared can be derived

$$m^2 = p^2(n^2\cos^2\theta_C - 1) = p^2\left(\frac{1}{\beta^2} - 1\right) = p^2\left(\frac{n^2 L^2}{L^2 + r^2} - 1\right) \tag{4.21}$$

The error on the mass–squared can now be determined from error propagation. Note that the only quantities that are measured with an uncertainty are r and p. The focal length L and the refractive index n are constants and should therefore not be assigned uncertainties.

$$\frac{\sigma^2_{m^2}}{m^2} = \left(\frac{\partial(m^2)}{\partial p}\sigma_p\right)^2 + \left(\frac{\partial(m^2)}{\partial r}\sigma_r\right)^2 \tag{4.22}$$

$$= \left[2p\left(n^2\frac{L^2}{L^2+r^2} - 1\right)\sigma_p\right]^2 + \left[2p^2 n^2 \frac{rL^2}{L^2+r^2}\sigma_r\right]^2 \tag{4.23}$$

$$= \left[2p\left(\frac{1}{\beta^2} - 1\right)\sigma_p\right]^2 + \left[2p^2\frac{L\sqrt{\beta^2 n^2 - 1}}{\beta^2}\sigma_r\right]^2 \tag{4.24}$$

The particle identification selection (cuts) can now be done using the estimated uncertainty of the mass–squared as function of momentum. Figure 4.18 show the measured mass–squared as function of momentum. The curves indicate the estimated $\pm 2\sigma_{m^2}$ around the *true* mass–squared for pions, kaons and protons. Other parameterizations of the PID selection functions have been used in ref. [95, 81, 86].

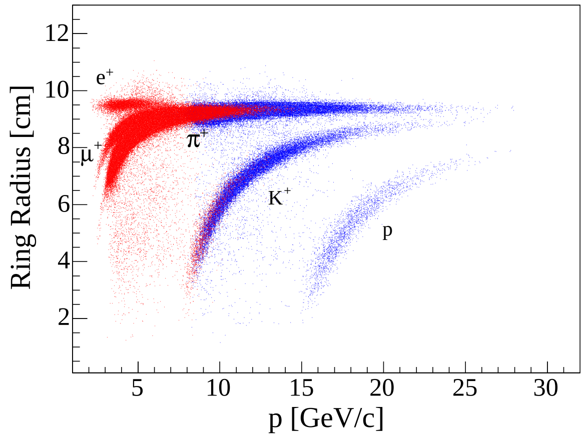

Figure 4.17: Ring radius as function of momentum for two different magnet settings (red and blue data points). The bands in the data correspond to electrons, muons, pions, kaons and protons.

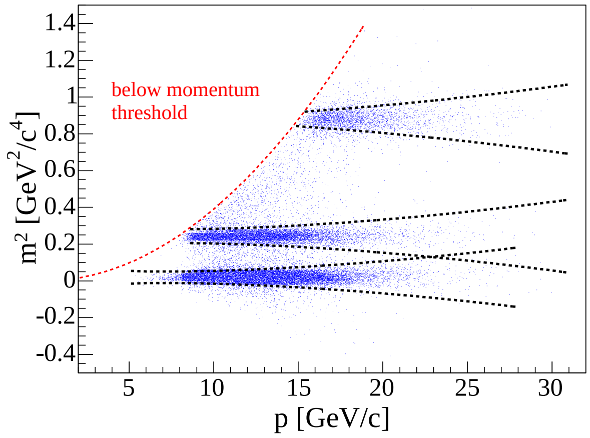

Figure 4.18: Mass–squared as function of momentum. The dashed curves indicate a $\pm 2\sigma$ cut around the pions, kaons and protons.

Alignment of the Image Plane

The position of a ring on the image plane depends on the angle of the track in the BFS. If the geometry (used in the reconstruction algorithm) is not exactly the same as *true* geometry it will result in a shift of the ring images compared to the reconstructed ring centers. Ring images can still be reconstructed, however with a reduced efficiency. Assuming that the geometry of the tracking detectors is correct, the position of the image plane (used in the reconstruction algorithm) can be aligned by studying the distance from the single hits to the reconstructed rings. The single hit is placed in an angle ϕ and a distance $r + \delta r$ from the reconstructed ring center – here, r is the radius of the reconstructed ring.

Figure 4.19 (a) shows the normalized hit position (ϕ and $(r + \delta r)/r$) relative to the ring center – this gives a picture of the *average* ring image. The dashed circle indicates the ring with the correct (reconstructed) center. It is clear from the figure that the reconstructed rings are slightly mis–aligned. Figure 4.19 (b) shows the radial distance δr from the single hits to the ring as function of ϕ. Here, the wave shape illustrates the mis–alignment. The direction and size of the mis–alignment can be found by fitting the δr as function of ϕ with $\delta r(\phi) = \delta r \cos(\phi + \delta\phi)$, see panel (c). The offset of the image plane is given by $(\delta x, \delta y) = (\delta r \cos(\delta\phi), \delta r \sin(\delta\phi))$. Figure 4.19, panel (d), (e) and (f) show the same as panel (a), (b) and (c) after the alignment of the image plane.

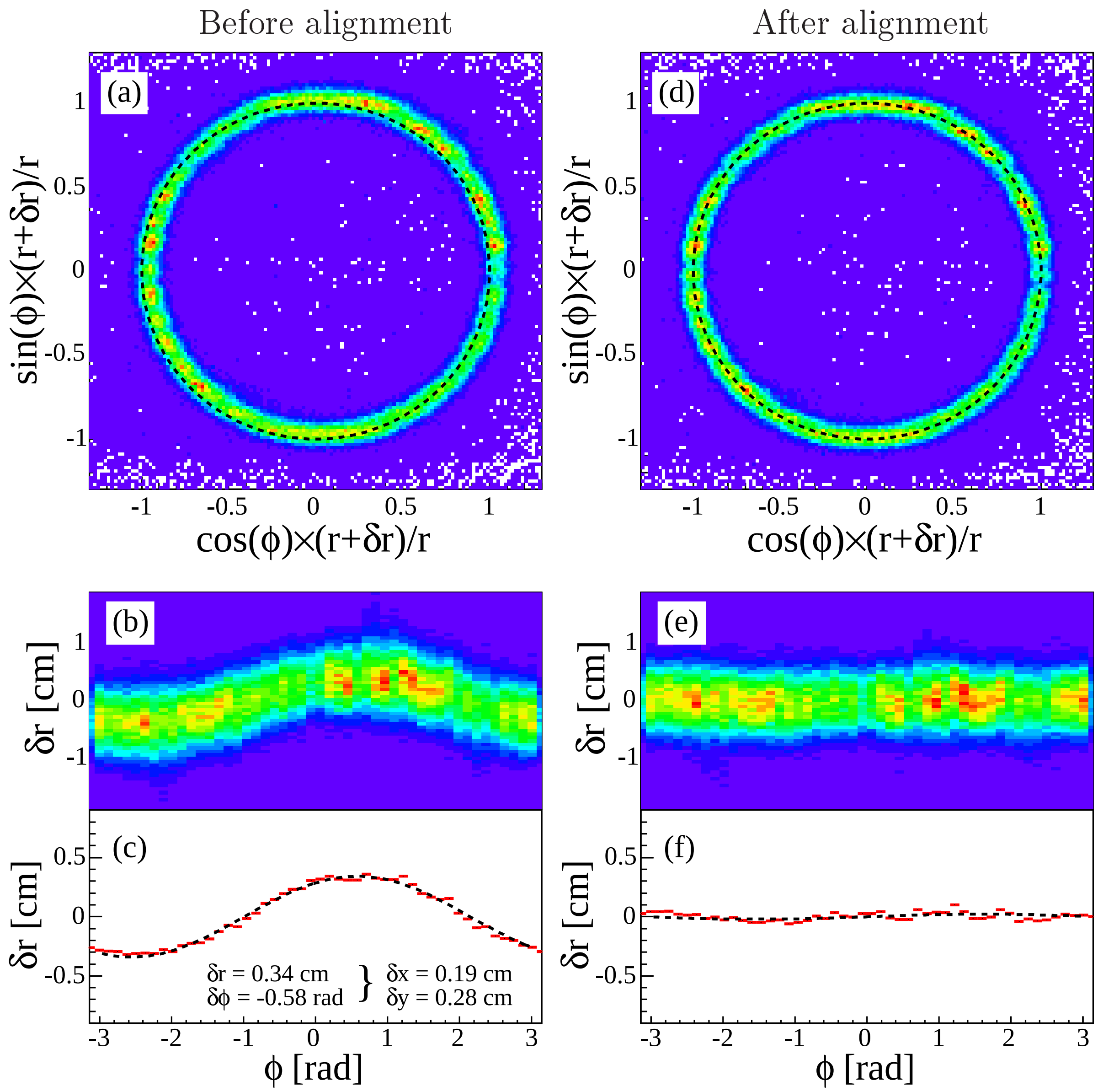

Figure 4.19: Alignment of the RICH image plane. Panels (a) and (d) show the normalized radial distance $(\delta x, \delta y)$ to the expected ring. Panels (b) and (e) show the radial distance δr as function of angle ϕ. Panels (c) and (f) show the cosine fit to the radial distance as function of angle. In panel (c) the (determined) offset of the image plane is listed in $(\delta r, \delta\phi)$ and $(\delta x, \delta y)$.

Chapter 5

High p_T Analysis

This chapter describes the analysis method used to obtain spectra of unidentified charged hadrons in $Au+Au$, $d+Au$ and $p+p$ collisions at $\sqrt{s_{NN}} = 200\,\text{GeV}$ and in $Au+Au$ collisions at $\sqrt{s_{NN}} = 62.4\,\text{GeV}$. The spectra from the nucleus–nucleus collisions and the corresponding reference spectrum from the $p+p$ collisions are used to construct the nuclear modification factors (see section 2.2). The particle spectra have been obtained at different pseudo–rapidities. In the 200 GeV $Au+Au$ data charged hadron spectra are measured at $\eta = 0$ and negative hadron spectra are measured at $\eta = 2.2$. In the 200 GeV $d+Au$ and $p+p$ data charged hadron spectra are obtained at $\eta = 0$ and $\eta = 1$. In the 62.4 GeV $Au+Au$ data charged hadron spectra are measured at $\eta = 0$ and $\eta = 0.95$. The analysis method is similar to the one used for obtaining the results in ref. [96] and ref. [97]. However, some of the corrections have been refined and the systematic errors have been studied more carefully. The 62.4 GeV $Au+Au$ analysis is preliminary.

In this thesis, the word *spectrum* $f(p_T)$ is used for the differential yield in a narrow η interval as function of transverse momentum.

$$f(p_T) = \frac{1}{2\pi}\frac{1}{p_T}\frac{d^2N}{d\eta dp_T} \tag{5.1}$$

The basic principle in the analysis is to count the number of detected tracks and the number of events in a data sample, scale them by the different correction factors and take the ratio. The particle (or track) selection and event selection are described in sections 5.1 and 5.2, respectively. Tracks (and events) are weighted by factors that takes into account the trigger scale–down, the limited acceptance of the spectrometers, detector inefficiencies etc. These correction are discussed sections 5.3 and 5.4.

The procedure for obtaining particle spectra is slightly different than the procedure used in previous BRAHMS analyses. The two methods are discussed in section 5.5, where also a few details on the analysis are presented. Sections 5.6 and 5.7 discuss the factors that goes into the nominator of the nuclear modification factor, i.e. the calculation of the mean number of binary collisions and the construction of the reference spectrum. Finally, the systematic errors stemming from the experimental setup, the data reconstruction and the analysis method are evaluated.

The different spectrometer settings are denoted by the angle (in degrees), the polarity of the magnetic field (A or B) and the current (in Ampere) applied to the D1 magnet in the FS/FFS and the D5 magnet in the MRS. For example, 40A1050 means that the spectrometer (MRS) was positioned at 40 degrees, the polarity was A (deflecting negative particles to the right) and the current applied to D5 was 1050 Ampere.

5.1 Event Selection

A number of cuts are applied to the event sample in order to select and count collisions. These are summarized in table 5.1 and explained in the following.

The vertex cut is applied to all the data samples ($Au+Au$, $d+Au$ and $p+p$) to select events in the vertex range around the nominal IP. Outside the central region the MB trigger becomes inefficient and including these data biases the results. In the $Au+Au$ data sample it is also necessary to stay well inside the MA detector array in order to get a good centrality determination. The vertex cut is applied to the ZDC vertex distribution for the 200 GeV $Au+Au$ data sample, to the BBC vertex in the 62.4 GeV $Au+Au$ data sample and to the the INEL vertex distributions for the $d+Au$ and $p+p$ data samples.

Cut	$Au+Au$ (200 GeV)	$Au+Au$ (62.4 GeV)	$d+Au$ (200 GeV)	$p+p$ (200 GeV)
Vtx (MRS/FS)	$< \pm 15$ cm/25 cm	$< \pm 15$ cm	$< \pm 15$ cm	$< \pm 15$ cm
Vtx consistency	VtxBB-VtxZDC$< 3\sigma$	–	–	–
Trigger	6 (0–20%), 4 (20-60%)	1	5	5
Centrality (%)	0–10,10–20,20–40,40–60	0–10,10–20,20–40,40–60	–	–

Table 5.1: Event selection cuts.

The vertex consistency cut is only applied in the 200 GeV $Au+Au$ data sample. Here the vertex methods (ZDC and BBC) are both 100% effecient (in the analyzed centrality ranges) and the cut ensures that possible background events are not included. Background events rarely give a large signal in the multiplicity array and the cut has little impact on the number of events in the analyzed centrality ranges. Figure 5.1 illustrates the cut.

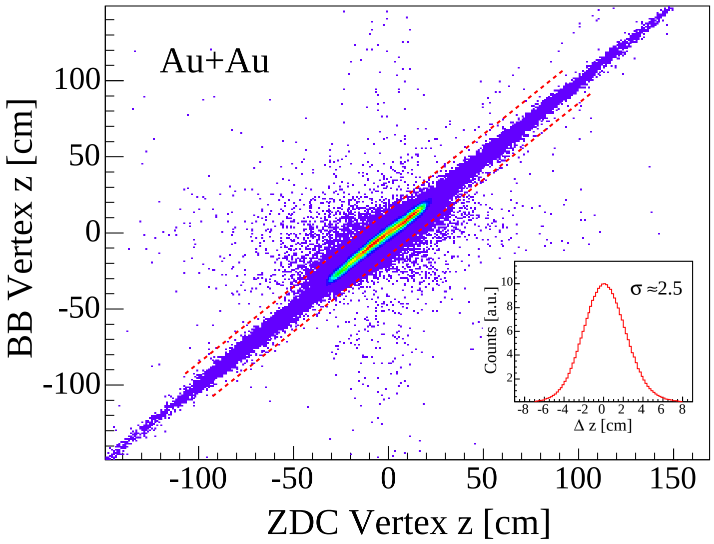

Figure 5.1: BBC vertex as function of ZDC vertex for the $Au+Au$ data sample

The trigger cuts are applied when counting the number of events (for the event normalization). In the $d+Au$ and $p+p$ this is done by selecting only events where the MB trigger have survived the scale–down. By scaling up (see section 5.3), the total number of (minimum biased) events can be found. In the 62.4 GeV $Au+Au$ data sample the ZDC trigger was not 100% efficient for the most central collisions and the BBC trigger (which is efficient in the analyzed centrality range) is used. In the 200 GeV $Au+Au$ the centrality trigger (trigger 6) is used for event count of the central event (0–20%). In this centrality range trigger 6 is 100% efficient and selecting trigger 6 events does not impose a bias on the data sample. For the more peripheral events trigger 6 becomes less efficient and below centrality of ~30% the trigger 6 condition is never fulfilled. This is illustrated in figure 5.2. For centralities > 20% the MB trigger is used for the event counting.

The centrality cuts are only applied in the $Au + Au$ data sample. This is done as described in section 4.1.2.

Figures 5.2 and 5.3 shows the centrality distributions for the 200 GeV $Au + Au$ and the $d + Au$ data. In the $Au + Au$ setup the MB trigger corresponds to 95% of the total inelastic cross section. The MB centrality distribution should therefore be flat from 0 to 95% (this is indecated by the green dashed line in figure 5.2). The effect of a BBC vertex and the trigger 6 requirements are illustrated by the red and black lines. The fact that the distributions are not flat in the central range is due to non–optimal calibration of the multiplicity/centrality. Also, the effect of requiring a track is indicated – this of course depends on the MRS setting and is only shown here to illustrate the order of magnitude.

The $d + Au$ minimum bias trigger correspond to $91 \pm 3\%$ of the inelastic cross section. The centrality distribution should therefore be flat from 0 to 91% (green dashed line in figure 5.3). Figure 5.3 shows the effect of requiring a reconstructed BBC vertex – this requirement is only fulfilled for approximately half of the minimum bias sample. Also, the effect of requiring a track in MRS is shown.

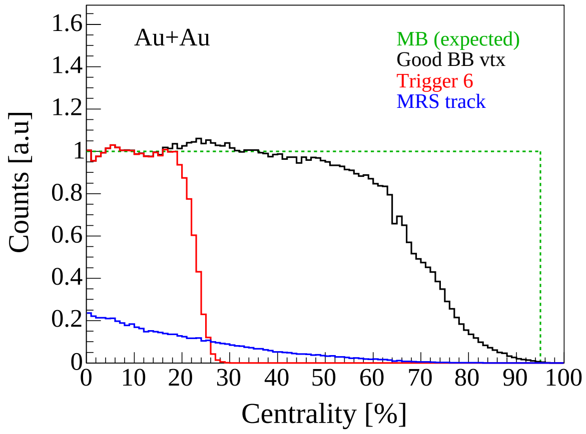

Figure 5.2: Centrality distribution for the $Au + Au$ data sample. The minimum bias trigger correspond to 95%.

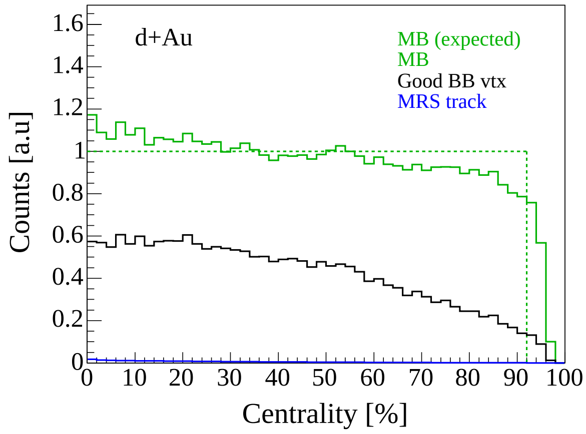

Figure 5.3: Centrality distribution for the $d + Au$ data sample.

5.2 Track Selection

Only two cuts are applied to select global tracks: one that ensures that the track comes from the vertex and one that ensures that the track hits the trigger detectors. The latter only affects the MRS tracks, since the tracks in the forward spectrometer cannot avoid hitting the FS track trigger counters (TRFS, H1 and H2).

As described in section 4.2.3 the definition of the track vertex is different in the MRS and in the FS. In the MRS, the track vertex is the intersection of the track line and the $y - z$ plane of the beam. In the FS it is the intersection with the $x - y$ plane at the z position of the collision vertex (BBC or INEL). An elliptical cut is applied to select tracks originating from the collision.

$$\left(\frac{x - x_{off}}{\sigma_x}\right)^2 + \left(\frac{y - y_{off}}{\sigma_y}\right)^2 \leq n_\sigma^2 \quad \text{(FS cut)} \tag{5.2}$$

$$\left(\frac{\Delta z - \Delta z_{off}}{\sigma_{\Delta z}}\right)^2 + \left(\frac{y - y_{off}}{\sigma_y}\right)^2 \leq n_\sigma^2 \quad \text{(MRS cut)} \tag{5.3}$$

The widths in the horizontal and vertical direction (σ_x, σ_y and $\sigma_{\Delta z}$) are found from the 1–dimensional distributions. Figure 5.4 illustrates the cuts in MRS and FS.

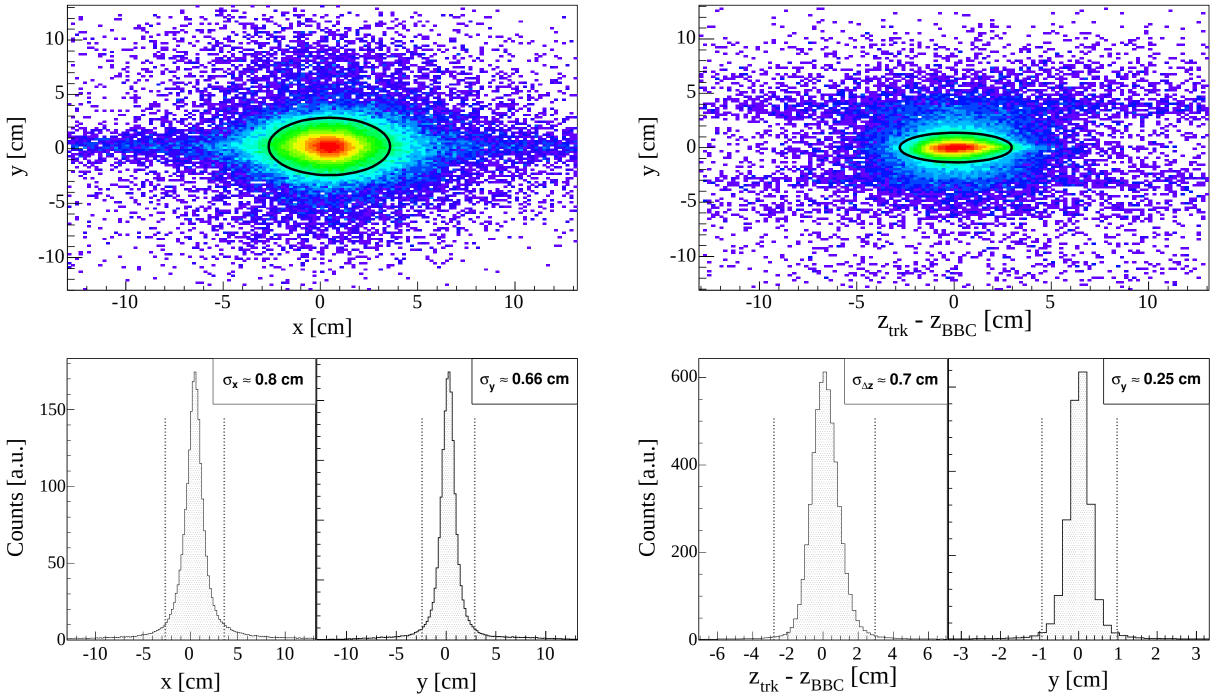

Figure 5.4: Track–to–vertex cuts in the FS (left) and in the MRS (right). The bottom panels show the one dimensional track–to–vertex distribution in y, x (MRS) and $z_{track} - z_{event}$ (FS). The top panels show the two dimensional track–to–vertex distributions. The track–to–vertex cuts are indicated by ellipses.

5.3 Scaling Up the Number of Events/Tracks

The number of events and the number of tracks is counted with the conditions explained in the two previous sections. The number of tracks per event (which is needed to obtain the spectra) cannot be obtained without taking into account the scale–down of triggers. The event sample is indeed highly biased because of the scale–down of the various triggers.

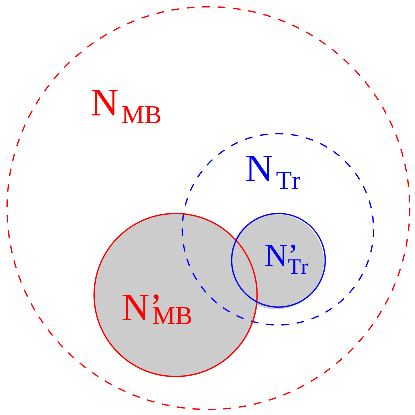

Figure 5.5: Illustration of the set of events. The scale–down factors are used to *scale up* the events in order to normalize correctly.

Of the total event sample that fulfills the MB trigger condition (and *meets* the trigger box), not all events are kept. The total number of events (recorded or not) can be obtained by counting the number of events where the MB trigger survived the scale–down and multiply it with the scale–down factor. The number of tracks in the total event sample can be obtained in a similar manner – count the number of tracks in events where the spectrometer trigger survived the scale–down and multiply by the spectrometer trigger scale–down factor. In other words, only events that survived the scale–down of the trigger related to the given measurement should be considered. By *scaling up*, information on the number of tracks per event in all the events (recorded or not) can be obtained and normalization becomes possible.

Figure 5.5 illustrates the method in the case of two triggers, a minimum bias (MB) and a spectrometer (Tr). The total number of MB events (recorded or not) is denoted N_{MB}, while the ones that survive the scale–down are N'_{MB}. The MB scale–down factor is $SD_{MB} = N_{MB}/N'_{MB}$. Similar notation is used for the events where the spectrometer trigger condition is fulfilled. The recorded events are marked with a gray background. The number of tracks per event in the total event sample (N_{MB}) is given by $N_{Tr}/N_{MB} = (SD_{Tr} \cdot N_{Tr})/(SD_{MB} \cdot N_{MB})$. The picture becomes more complicated when more triggers are included, but the principle in the *scale–up* is the same. Note, that not all the statistics (tracks) in the recorded event sample are used in the analysis. Tracks in events for which the spectrometer trigger did not survive the scale–down, but some other trigger survived are not included (in figure 5.5, these are the tracks in the events in the N'_{MB} sample that are included the N_{Tr} sample but outside the N'_{Tr} sample). The information on how to get back to the total number of tracks is lost, i.e. the number of tracks in these events cannot be *scaled up*. In other words, not all recorded tracks can be used in the analysis because the scale–down information is lost.

5.4 Corrections

The MB event sample correspond to (almost) all events, while the track sample only contains the tracks that were reconstructed in the spectrometers, i.e. tracks from particles emitted in the small regions in the $\eta - p_T$ space (see section 3.2.2). Fortunately, the spectrometer geometry and performance is known and the missed tracks can be corrected for. The charged particle spectra can also be slightly distorted due to decay of particles. This effect is also estimated and corrected for.

In the analysis presented here (as in all other BRAHMS analyses), it is assumed that the different corrections does not affect each other, i.e. that they factorize. The corrections are therefore evaluated independently. A more correct approach would be to evaluate all the corrections using a detailed Monte Carlo simulation including all the effects. However, considering the number of different setting of the spectrometers, this is an unrealistic task.

5.4.1 Acceptance Correction

The spectrometers only measure particles that are emitted in a small solid angle and within a small momentum range. Figure 5.6 illustrates how only a few out of many tracks are measured in the MRS.

In order to calculate the differential yield (including particles that are emitted outside the spectrometer acceptance), the number of measured particles must be multiplied by $2\pi/\Delta\phi$, $1/\Delta\eta$ and $1/\Delta p_T$, where $\Delta\phi$ is the spectrometer coverage in azimuthal angle, $\Delta\eta$ is pseudo–rapidity coverage and Δp_T is the width of the particular p_T bin. Figure 5.7 illustrates the $\Delta\phi$ dependence of the spectrometer angle or pseudo–rapidity. The coverage becomes larger as the spectrometer angle decreases. Also the position of the collision vertex is important for the spectrometer acceptance – this is illustrated in figure 5.8.

The acceptance correction is calculated once for each spectrometer setting and saved as so called acceptance maps. The acceptance maps contain the acceptance correction in the $\eta - p_T$ plane. As illustrated in figure 5.8, the acceptance changes with the collision vertex – this is taken into account by making acceptance maps for the different vertexes (typically divided into bins of 5 cm).

Acceptance Maps

A Monte Carlo simulation has been used to generate the acceptance maps. The exact geometry and magnetic fields of the spectrometers are used in the simulation. A large number of charged particles (starting at some vertex with some momentum vector) are propagated through the spectrometer. On the way, it is checked if the track falls outside the fiducial cuts defined in the magnets, in the tracking chambers and in the trigger or PID detectors. If the particle makes it through the spectrometer it is *accepted*. The ratio of the number of accepted to the number of thrown particles is calculated for

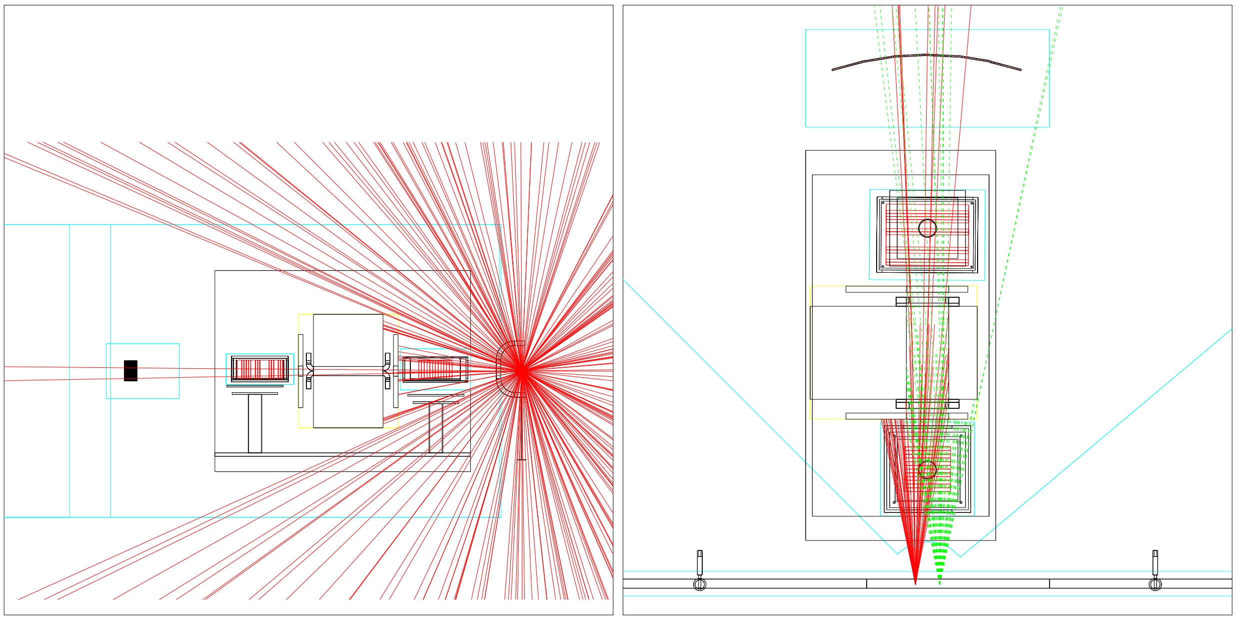

Figure 5.6: BRAG simulation illustrating the limited acceptance of the MRS. The spectrometer is seen from the side (left) and from the top (right).

each $\eta - p_T$ bin. These ratios in the $\eta - p_T$ space (one for each vertex bin) are the acceptance maps. The value of the map in a certain $\eta - p_T$ bin reflects the ϕ acceptance (for the specific vertex bin).

The finite size of the vertex bins smear out the edges of the acceptance maps. Here, the correction can become very large and uncertain. Therefore the edges are *cut off* the acceptance maps. This means that the (edge) bins in the acceptance maps where the level (bin content) is less than a certain limit is disregarded, i.e. the bin content is set to zero. The limit is set to one half of the maximum map value in the MRS and one third of the maximum in the FS.

Making $\eta - p_T$ distributions with the number of tracks and dividing these with the acceptance maps (and the number of events) will give the differential 2–D yields (here ignoring the effects of the other corrections). However, the goal is the p_T spectra where the $\Delta\eta$ is also included.

The procedure for generating acceptance maps is different from the procedure used in other BRAHMS analyses. The main difference is the Monte Carlo simulation. Traditionally, the GEANT package [98] has been used. This is a full detector simulation that can take into account all physical processes like energy loss of the particles in the traversed air and detector volumes, particle decay, etc. Since the acceptance correction used is purely geometrical (including the magnetic fields), and does not take into account inefficiencies or decay of particles etc. a full GEANT detector simulation is not necessary. The simplified Monte Carlo simulation was developed to save computation time and disk space. The Monte Carlo simulation also has the advantage that it picks up the geometry from the BRAHMS data base for the specific runs. The dis–advantage of the Monte Carlo simulation is that it cannot easily be extended to include particle decay, multiple scattering, etc.

The η Acceptance

The width of the η coverage is either limited by the acceptance (the width of the map) or by a cut. In the present analysis, the η coverage is calculated from the limits defined by the acceptance map and/or the cut and multiplied to the map. This is done for each bin in p_T. The resulting (new) maps therefore also include the η acceptance correction. Figure 5.9 shows the maps before (top panels) and after (bottom panels) the η acceptance correction (and edge cuts).

These maps contain all the information needed for the acceptance correction. How the maps are

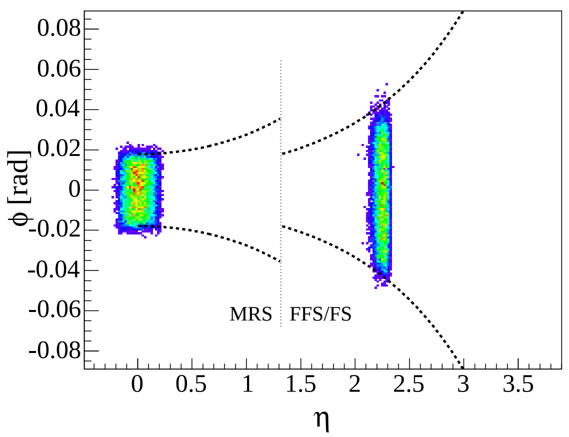

Figure 5.7: Azimuthal angle coverage. The dashed curves show the coverage calculated from the opening and distance to the back–plane of D5 (in the MRS) and D1 (in the FFS/FS). The histograms are from MRS data (at 90 degrees) and FS data (at 12 degrees).

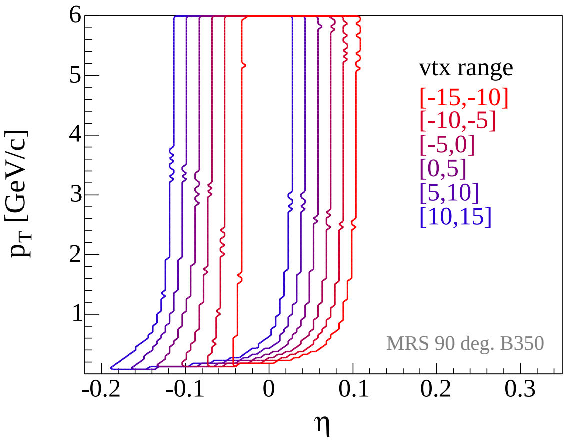

Figure 5.8: Outline of the MRS acceptance in $\eta - p_T$ for different vertex ranges (positive particles). The spectrometer covers different regions in $\eta - p_T$ for different vertexes. The η width of the coverage is changed dramatically in the low p_T region.

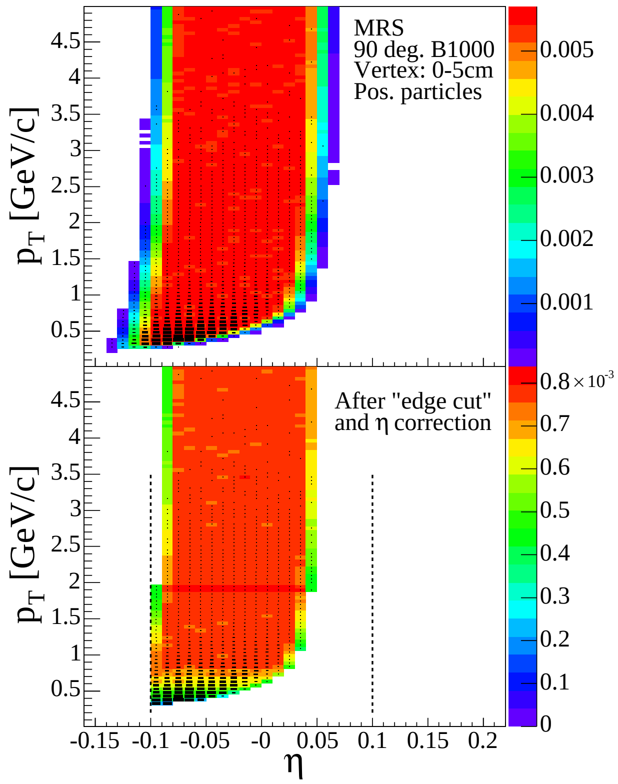

Figure 5.9: Example of maps in the MRS (left) and FFS (right). The upper panels show the ϕ correction maps in colors (number of particles that makes it through the spectrometer in the Monte–Carlo simulation divided by the number of particles thrown). The data are overlaid as black boxes. The lower panels show the maps after the η acceptance correction has been applied.

used to construct the particle spectra will be described in section 5.5.

5.4.2 Efficiency Correction

The efficiencies that affect the analysis are the trigger efficiencies (both the minimum bias trigger and the spectrometer triggers) and the tracking efficiency. The efficiency of the PID detectors are not relevant for the present analysis where only unidentified hadrons are studied.

The minimum bias trigger efficiency has been studied using GEANT simulations of the experimental setup with HIJING events as input. The MB trigger for the $Au + Au$ only picks up 95% of the inelastic cross section. The missed events are the most peripheral, which means that the data in the analyzed centrality range ($0 - 60\%$) is not biased. However, the uncertainty on the MB efficiency affects the centrality determination. If for example, the MB trigger is 93% efficient instead of the used 95%, the quoted $0 - 10\%$ are in fact the $0 - 10.2\%$ central and the quoted $40 - 60\%$ central are in fact the $40.8 - 61.2\%$ central. This error is taken into account when calculating the mean number of participants or the mean number of binary collisions for a given centrality class (see section 5.7).

In the $d + Au$ setup the MB trigger is slightly less efficient, $91 \pm 3\%$. Also here, only the more peripheral events are missed.

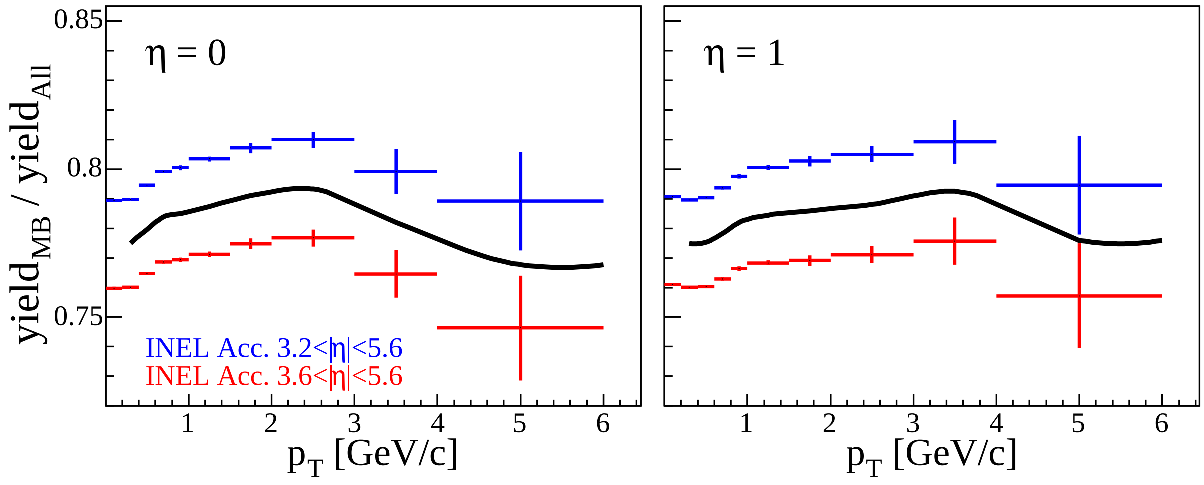

Figure 5.10: Effect of the (INEL) $p+p$ trigger efficiency on the p_T spectra of charged hadrons from HIJING for $\eta = 0$ (left plot) and $\eta = 1$ (right plot). The plots show the ratio of the spectrum from all inelastic events to the spectrum from events where the trigger condition is fulfilled. The blue and the red histograms show the ratio for two different definitions of the INEL acceptance. The black curves show the applied correction.

In the $p + p$ setup the MB trigger only selects events corresponding to $\approx 70\%$ of the inelastic cross section. Since the spectrum from $p + p$ is used as reference in the nuclear modification factor it must be corrected for the trigger efficiency (the reference spectrum in the nuclear modification factor should be the spectrum from all inelastic $p + p$ collisions). The effect of the efficiency on the p_T spectra have been evaluated from the HIJING model (which for $p + p$ collisions is identical to PYTHIA). For each event, it is required that (at least) one charged particle is emitted in the direction of the left INEL counters and one in the direction of the right INEL counters. The ratio of the p_T spectra with and without this requirement gives the correction. The acceptance of the INEL counter depends slightly on the azimuthal angle (the counters are not radial symmetric as shown in figure 3.5). The efficiency and the uncertainty in the efficiency was estimated by changing the acceptance between $3.2 < |\eta| < 5.6$ and $3.6 < |\eta| < 5.6$ relative to the nominal interaction point (see section 3.2.3). The effect of moving the vertex by 10 cm (and using the corresponding asymmetric pseudo–rapidity coverages of the counters) is also investigated. It changes the result less than one percent. Figure 5.10 shows the corrections for $\eta = 0$ and $\eta = 1$. The ratios are used to correct the $p + p$ spectrum. In ref. [97] a constant of $13 \pm 5\%$ was used to correct the spectra at all η and p_T.

A more detailed study could be done using a full GEANT simulation of the detector response. Here, only the simple geometry of the trigger detectors have been used to study the effect.

The tracking efficiency have been evaluated by two different methods, the track embedding method and the reference track method. The reference track method can only be used in the FS, since it requires more than two tracking detectors.

The track embedding method takes the raw TPC data from real events and inserts a simulated (digitized) tracks. The efficiency of the detector is the chance of reconstructing the inserted track. The combined MRS efficiency is found to have a small dependence on particle specie and a rather small dependence on centrality. In ref. [99] the MRS efficiency is determined as function of hits (see section 3.2.4) in the two TPCs. This is shown in figure 5.11. The mean number of TPC hits in the 200 GeV $Au + Au$ data sample vary from $\sim 60 - 350$ as the centrality vary from $0 - 60\%$. In the analysis presented here, the MRS efficiency is set to $90 \pm 5\%$. This number is used for all collision systems and centralities.

The reference track method is used for tracking detectors in the FS. The method makes the full FS track reconstruction, using all the detectors except the one under investigation. A modification of the global tracking is needed for this purpose – local track matching over two magnets are done, e.g. T3–D3–D4–T5 matching. The global track trajectory through the investigated tracking detector is compared to the local tracks of the detector. The chance of finding a local track that matches the global reconstructed trajectory gives the efficiency of the detector. The efficiency is calculated as function of collisions centrality and horizontal track position and slope. In the final analysis, the efficiencies are found for each single FS/FFS track by looking up the efficiency for each of the traversed detectors and multiplying these. Figure 5.12 shows efficiency distribution for track in the FFS and in the FS.

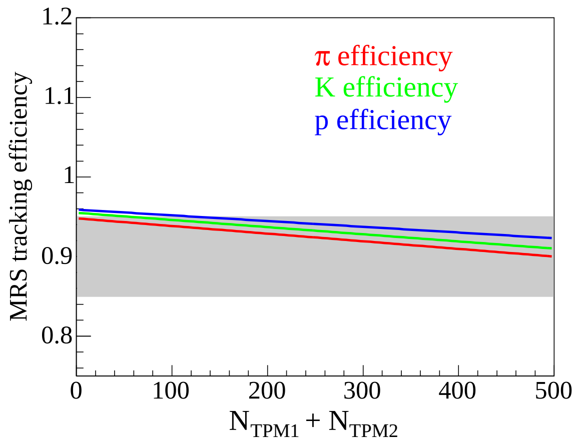

Figure 5.11: MRS tracking efficiency as function of the number of hits in TPM1 and TPM2 calculated using the track embedding method. The gray area indicates the efficiency used for unidentified hadrons (independent of the number of hits).

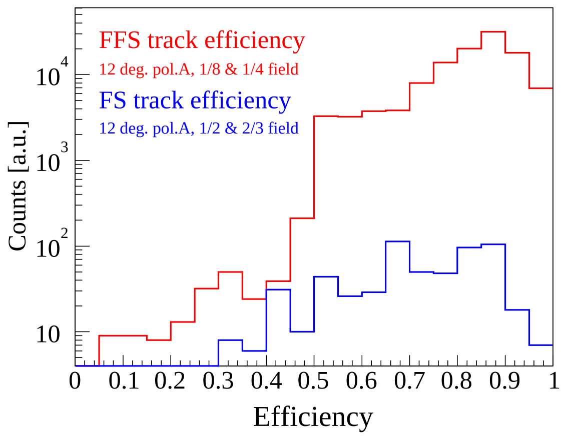

Figure 5.12: FFS/FS tracking efficiency calculated per track using the reference track method. Two track samples with the spectrometer positioned at 12 degrees are shown as examples.

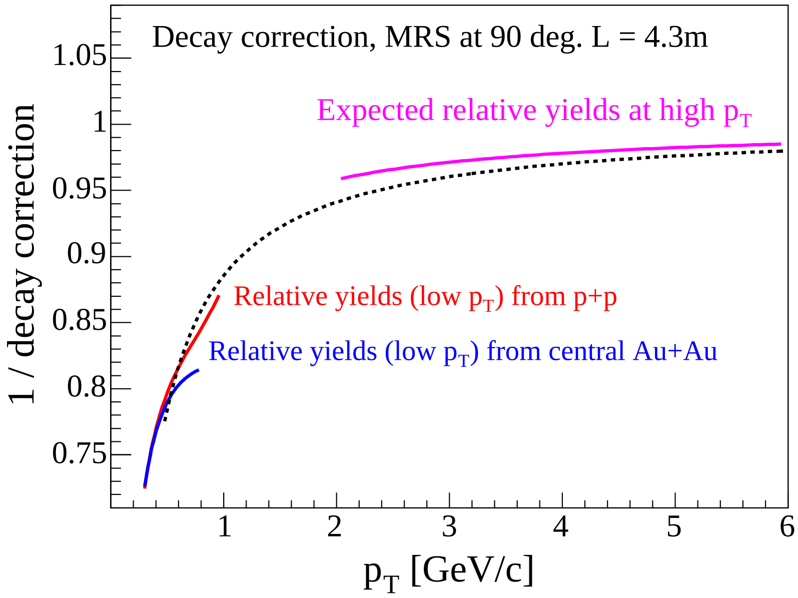

Figure 5.13: Decay correction in the MRS calculated from the decay of pions and kaons and assumptions on the relative pion, kaon and proton abundances. The dashed curve show the applied correction.

5.4.3 Decay Correction

The decay of particles is estimated from the theoretical decay law. The probability that a particle with mass m and momentum p does not decay before it has traveled the length L is given by $\exp(-Lm/(pc\tau))$, where L is the traversed distance and τ is the mean life time ($c\tau_\pi = 7.8\,\mathrm{m}$ and $c\tau_K = 3.7\,\mathrm{m}$). The effect on the unidentified hadron spectra depends on the particle composition as function of p_T. Figure 5.13 shows the correction in the MRS calculated for different relative yields of pion, kaons and protons. The relative yields at low p_T have been measured [17], while the relative yields at high p_T are assumed to be $\pi/p = 1$ and $K/\pi = 0.2$. In the high p_T region the effect of different (reasonable) assumptions on the relative yields is lower than 2% due to the fact that the high momentum particles have a smaller chance of decaying before being measured in the spectrometers. The effect of other particle species is neglected. The correction is almost independent on the collision system (and centrality) and one correction have been used for all spectra. The correction for the MRS at 40 degrees and for FFS and FS at 12 degrees can easily be calculated by scaling the p_T (on the $x-$axis in figure 5.13) by $\sin\theta$ and the spectrometer length (relative to the MRS).

In this calculation of the decay correction, it assumed that the decay products of the particle do not have any effect. In reality, a pion decaying to a muon could still be reconstructed as a particle in the spectrometer. This effect is not considered here. The effect of the decay from theoretical calculations (as described above) has been compared to a full Monte Carlo GEANT simulation including the multiple scattering of particles. The results show a difference of less than 3% [100]. The systematic error on the decay correction applied here is estimated to be less than 5% in the MRS and 2% in the FS.

5.4.4 Transverse Momentum Smearing Correction

The measured transverse momentum p'_T of particles are Gaussian distributed around the true transverse momentum p_T, as described in section 4.2.4. For a decreasing p_T spectrum this effect result in a hardening of the spectrum – the p_T that is shifted to a higher p'_T value adds more in relative terms to the yield than the p_T that is shifted to a lower p'_T. If the true spectral distribution $f(p_T)$

is known, the smeared spectral shape is given by

$$f'(p_T) = \int f(p_T) \cdot \frac{1}{\sigma_{p_T}(p'_T)\sqrt{2\pi}} \cdot e^{\frac{-(p_T - p'_T)^2}{2\sigma^2_{p_T}(p'_T)}} \, dp'_T. \tag{5.4}$$

Note that the spectrum $f(p_T)$ should be the *raw* p_T spectrum and not the invariant yield which includes a $1/p_T$ normalization. Performing the integration in 5.4 numerically requires very large computational power and the smearing is instead studied using a Monte Carlo simulation. A function of the form $p_T \times (1 + p_T/p_0)^{-n}$ has been used as input distribution. The p_T of the generated Monte Carlo tracks has been smeared according to estimated p_T resolution (equation 4.15). The momentum p was calculated from the p_T and a fixed angle (90, 40 or 12 degrees). Figure 5.14 shows the effect of the p_T smearing using the momentum and angular resolutions estimated in sections 4.2.4 and 4.2.4. The parameters p_0 and n have been set to reflect the power–law fits to the differential yields.

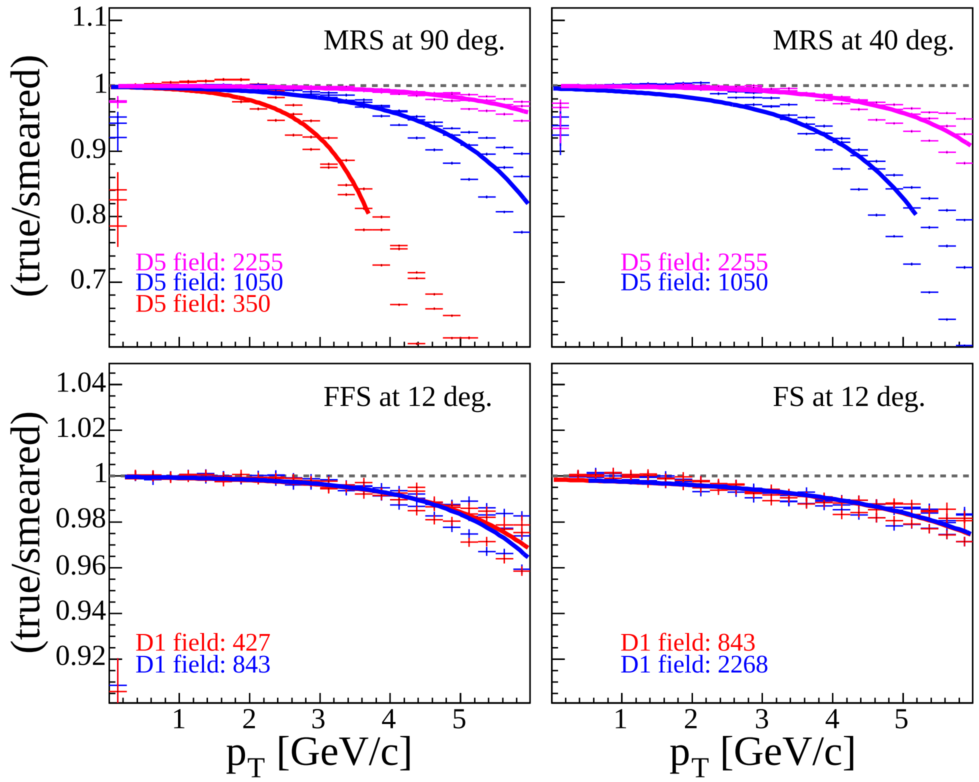

Figure 5.14: The effect of the finite p_T resolution. The histograms show the effect for different values of p_0 and n ($p_0 = 1.5 - 8\,\mathrm{GeV/c}$, $n = 12 - 30$) and for different magnetic fields. The top panels show the effect for the MRS at 90 and 45 degrees. The bottom panels show the effect in the FFS (left) and in the full FS (right) at 12 degrees. The solid curves show the applied correction.

In the FS and FFS at 12° the smearing effect is dominated by the angular resolution. Even with conservative estimation of the resolution, the effect is less than 4% for $p_T < 6\,\mathrm{GeV/c}$. In the MRS the effect is larger, especially for the low–field settings. The dependence on the choice of (reasonable) parameters p_0 and n is less important ($< 5\%$). The spectra measured in the MRS have been corrected separately for each magnetic field setting. Where the correction becomes larger than 20%, the spectra are not included in the construction of the final spectrum. The systematic error on the final spectrum arising from this correction is expected to be $\lesssim 5\%$ in the high p_T region.

5.4.5 Bin Shift Correction

The finite binning of the spectrum can result in a deviation of the data points from the true spectrum. The effect comes from the fact that the yield in a bin is set to the integral of the true spectrum in the range of the bin, i.e. the data point is placed at (x, y), where x is the middle of the bin and y is the yield (normalized by the bin width). The size of the effect depends on the shape of the spectrum and on the widths of the bins. Figure 5.15 illustrates the effect for a power–law spectrum.

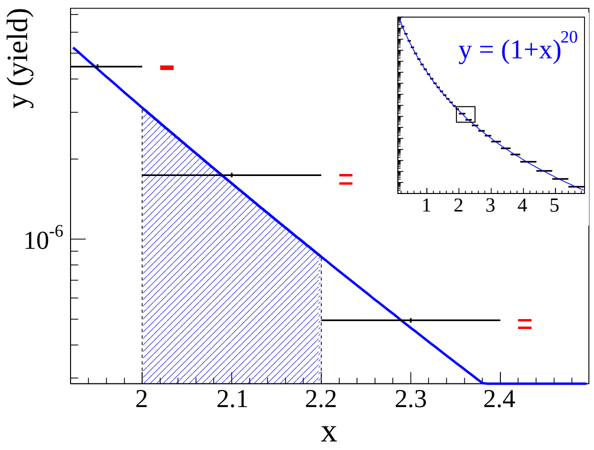

Figure 5.15: Illustration of the effect of finite bin widths. The data points are higher than the true spectrum (blue line). The two red lines to the right of each bin indicates the difference between the data point and the true spectrum at the x value of the data point.

The effect of finite bins can be corrected for by moving the data points in the direction of the p_T axis (and thereby getting data points that are placed asymmetric in the individual bins) or by moving the data points in the direction of the yield (y) axis. The latter approach has the advantage that it keeps the original x values of the data points, so that two spectra can be divided (bin by bin). If the true spectrum is described by $f(x)$, the $y-$correction to a data point in a bin with bin limits x_{min} and x_{max} is given by

$$C = \frac{\int_{x_{min}}^{x_{max}} f(x')dx'}{x_{max} - x_{min}} \frac{1}{f(x)} \tag{5.5}$$

The correction can of course only be done if the true spectrum $f(x)$ is known. A fit to the measured spectrum gives a good first approximation of the shape. In the present analysis, a power–law function is used as fit function. After the correction the new spectrum can be fitted and a better approximation to the true spectrum can be found. After a few of such iterations the corrected data points converges on the true spectrum.

The systematic error from this correction is related to the choice of fit function. If the function does not describe the exact shape of the true spectrum, a systematic error is introduced. The systematic error has been studied by using a function $f(x) = A(a_1 p_T + a_2 p_T^2)^{-n}$, which gives a better fit to the measured spectra. The difference in the correction from the two different fit functions is less than 2%.

5.4.6 Correction Summary

Table 5.2 summarizes the different corrections. The systematic errors are evaluated as described in the previous sections. Here, it is assumed that the different corrections can be treated independently. The systematic errors cannot be treated independently. For example, if the momentum for a given track is slightly off (because of the momentum resolution), the acceptance correction, which is looked up in the acceptance map, could be incorrect. The systematic errors associated with the p_T smearing and the acceptance can therefore not be treated independently. The numbers for the systematic errors listed in table 5.2 should be considered as the first rough estimate on the systematic errors. The systematic errors are discussed in more detail in section 5.8.

	MRS		FFS		FS	
	size	syst. err. [%]	size	syst. err. [%]	size	syst. err. [%]
Acceptance	$\sim 10^3 - 10^4$	2	$\sim 10^2 - 10^4$	2	$\sim 10^2 - 10^4$	2
Tracking eff.	1.1	5	~1.1	8	~1.5	12
Decay	$1 - 1.25$	5	$1 - 1.05$	2	$1 - 1.05$	2
p_T smearing	$0.8 - 1$	5	$0.96 - 1$	2	$0.98 - 1$	2
Bin shift	$0.95 - 1$	1	$0.75 - 1$	2	$0.75 - 1$	2
$p+p$ trig. eff.	~ 0.8	5	–	–	–	–

Table 5.2: Approximate sizes and estimated systematic errors (in percent) of the different corrections. In general, the systematic errors (and the corrections) depends on p_T. The listed systematic errors are the maximum values.

The bin shift correction (see section 5.4.5) does not depend on the spectrometer, but on the chosen binning of the spectrum histogram and the shape of the spectrum. The values listed in table 5.2 are for the obtained spectra at $\eta = 0$ and $\eta = 1$ (MRS at 90° and 40°) and for $\eta = 2.2$ (FS at 12°. The size of the correction (and the estimated systematic errors) varies little for the spectra from different collision systems and centralities.

The spectra have not been corrected for feed–down, e.g. a (neutral) lambda decaying into a (charged) proton and a pion which could be reconstructed as a charged hadron. The contribution from feed–down is estimated to be less than 10% in the low p_T range ($\approx 0.5\,\mathrm{GeV/c}$) and decreasing with increasing p_T. It is also expected that the contribution to first approximation is the same in heavy ion collisions and in $p+p$ collisions, since the relative particle abundances to first approximation are the same. This means that this effect on the nuclear modification factor is small (compared to the other systematic errors).

5.5 Making Spectra

As mentioned in the beginning of the chapter the goal of the analysis is to get the number of track per event in some η range and as function of p_T. Two different procedures for making spectra have been used in the analysis of BRAHMS data. The procedure of the two methods can be summarized:

Method A:

1) Acceptance maps (similar to those described in section 5.4.1) are generated using GEANT and normalized by the number of events in the corresponding vertex range.

2) Correction maps, including corrections for efficiency, absorption and multiple scattering, are multiplied to the acceptance maps. These maps, one for each vertex range, are then merged into one map that includes both the geometrical acceptance, the various other corrections and the event normalization.

3) The map is multiplied to a similar two–dimensional histogram containing the track data, which gives the two–dimensional yields $d^2N/dydp_T$.

4) The one–dimensional spectra are made by taking the number of tracks for all spectrometer settings (that falls inside the acceptance of the single setting) in the given p_T bin and divide it with the sum of the bin–content in the corresponding bins in the correction map. More details can be found in ref. [81] and ref. [86].

Method B:

1) The number of events in each vertex bin (taking into account the scale–down of MB events) are counted.
2) A histogram (the spectrum) is filled with the p_T of each track, weighted by: $1/p_T$, the acceptance correction (from the maps including the η normalization), efficiency corrections, the scale–down of the spectrometer trigger and one over the number of events in the given centrality and vertex range. This is done for each spectrometer setting.
3) The setting dependent p_T smearing correction is applied to the spectra (see section 5.4.4).
4) The spectra from the different spectrometer settings are merged. This is done by taking the weighted average bin per bin. Finally, the corrections for the bin shift effect is made.

The two methods gives consistent results in the low p_T range ($p_T \lesssim 2\,\mathrm{GeV/c}$). In the high p_T region it has not been possible to check the consistency with the available statistics. The problem is that spectra obtained using Method A cannot have variable bin width (in p_T), since the p_T binning is inherited from the acceptance maps. In the high p_T end the spectra (from Method A), therefore have a lot of bins with no data, which makes the direct comparison impossible.

Checking Method B

The analysis method have been checked using a small Monte Carlo event generator. A number of events with a number of particles following a certain p_T distribution have been generated. The particles are propagated through the spectrometer using their momentum vector and the vertex – this procedure is similar to that used in generation of the acceptance maps (see section 5.4.1). If a particle makes it all the way though the spectrometer, its track is treated as a *real* reconstructed track. The following analysis (geometrical acceptance correction, event normalization, etc.) is identical to the analysis of the real data. Corrections for effects not implemented in the Monte Carlo simulation is not applied, i.e. efficiency, decay, etc. The difference in the reconstructed spectrum and the input spectrum reflects the systematic errors that arises from the finite binning of the maps and the way the event normalization is done. The range of the reconstructed spectrum, which is smaller than the input spectrum, reflects the limited acceptance of the spectrometers.

Figure 5.16 shows the input and the reconstructed spectrum (top rows) for different settings in the MRS and FS. At the low p_T edge of the acceptance the reconstructed spectrum starts to deviate from the input spectrum. This is due to the finite binning of the acceptance maps (and the fact that the maps are generated from uniform distributions in η and p_T). The lowest couple bins should therefore be disregarded in the analysis. In the FS a similar effect is present at higher p_T. The ratio between the input and the reconstructed spectra are plotted in the lower panels of figure 5.16. Only the p_T range where the input and the reconstructed spectra are similar, is used in the analysis of *real* data. The used input distribution follows a power–law function. Varying the power–law parameters or using another (reasonable) input distribution has little effect on the ratios.

5.5.1 The $Au + Au$, $d + Au$ and $p + p$ Analyses

The principles of the $Au + Au$, $d + Au$ and $p + p$ analyses are very similar. The only differences are in trigger and centrality selections, in the scaling up of triggers and in the used vertex.

The 200 GeV $Au + Au$ analysis: In the $Au + Au$ data, trigger 6 (selecting $\sim 20\%$ central events) and trigger 4 were used to select events. No spectrometer trigger were implemented in the 2002 runs and correcting for the trigger scale–down is therefore not necessary. The vertex determined from the ZDC counters were used for all events.

The 62.4 GeV $Au + Au$ analysis: Here both the BBC trigger and the spectrometer triggers were scaled down. This was corrected for as described in section 5.3. Trigger 1 (BBC) was used to select events. This trigger is (in contrary to the ZDC trigger) 100% efficient in the centrality range $0 - 60\%$.

The $d + Au$ and $p + p$ analysss: As in the 62.4 GeV $Au + Au$ data, the scale down of triggers were corrected for. The vertex was determined from the INEL counters. The vertex resolution of the

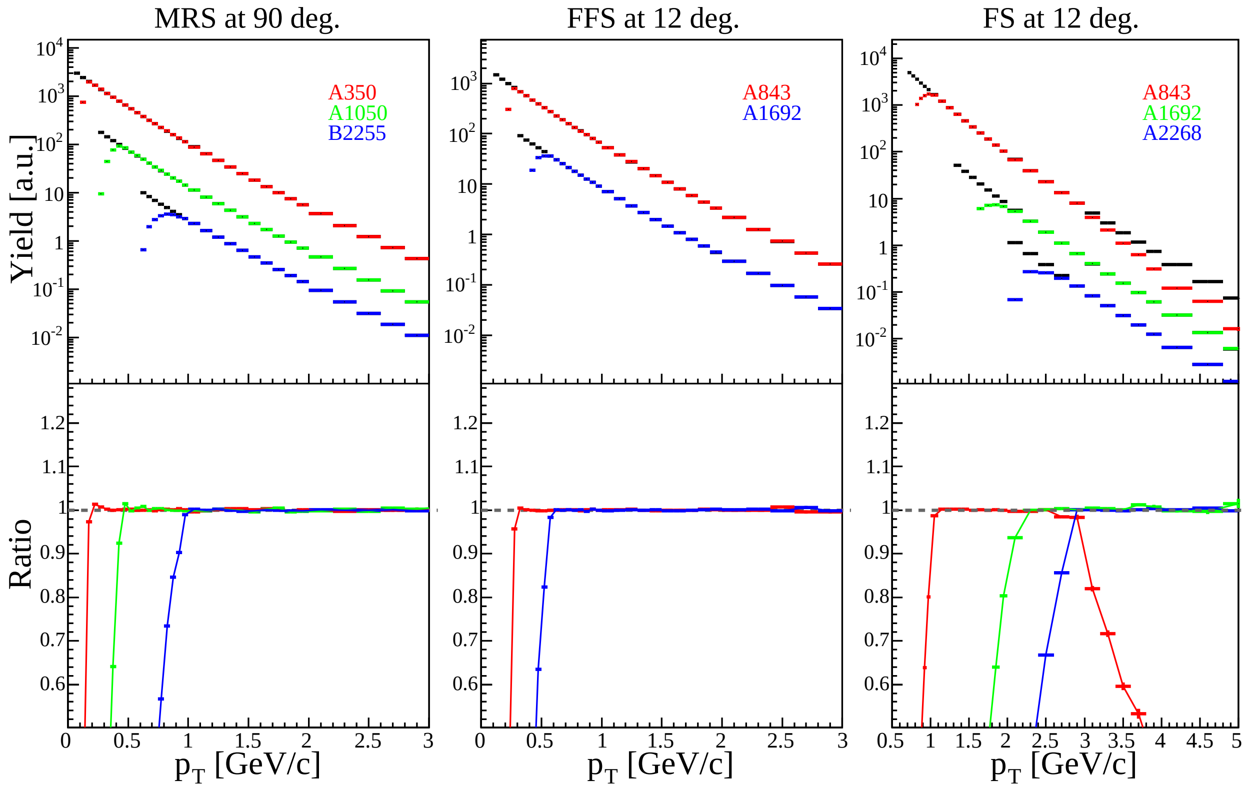

Figure 5.16: The procedure for acceptance correction and making the spectra have been checked using a Monte Carlo. The plots show the input (black) and reconstructed (colored) distributions (top panels) and the ratios (bottom panels) for different spectrometer settings. The edge effects from the acceptance correction is clear at low p_T. In the FS there is a similar effect at very high p_T, where the acceptance is very narrow (see red curves on the left panels). Fits to the ratios (above the acceptance edge) gives deviations from the input distribution of less than 2%, which leads to the conclusion that the method does not introduce any significant systematic errors. Different (reasonable) input distributions have been used with very similar results.

counter is $\approx 6\,\text{cm}$ but in some of the earlier runs (where the adc was not read out), the resolution was $\approx 9\,\text{cm}$. This imposes a smearing on the vertex distribution, which give rise to a systematic error on the measurements. The effect have been checked using the Monte Carlo simulation described in section 5.5 by smearing the vertex and assuming different vertex distributions. The effect is found to be negligible.

The quality of different data sets (runs) have been checked by plotting the number of reconstructed tracks per event (scaled by the trigger scale–down factors) in each settings. Few runs showed large fluctuations, which could arise from large detector inefficiencies. These runs have been left our in the final analysis.

The $\eta - p_T$ regions covered in the different settings are depicted in figure 5.17.

5.6 The Reference Spectra

Different reference spectra have been used for the construction of the nuclear modification factor. This section describes how the references for unidentified hadrons at $\eta = 0$ and $\eta = 2.2$ were constructed from old $p + \bar{p}$ data and how a parametrization of the measured spectra from $p + p$ is obtained. Also, the parametrization of the 62.4 GeV reference spectrum is described.

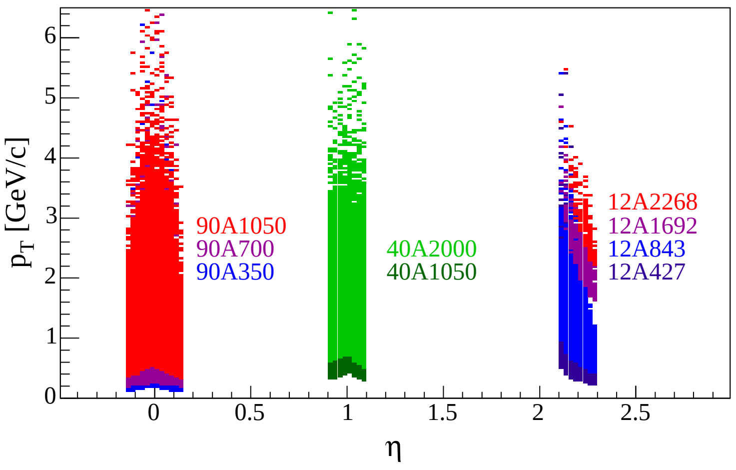

Figure 5.17: Acceptance in p_T versus η for the different spectrometer settings. In the analyzed FS settings, only negative hadrons were measured.

The 2002 $\sqrt{s_{NN}} = 200\,\text{GeV}$ Reference

Before the long $p+p$ RHIC run (in 2003), the reference spectra were constructed from the UA1 $p+\bar{p}$ data [101] at the same energy. These constructed spectra were used in ref. [96]. During the 2003 $p+p$ run, enough events were recorded to get reference spectra at $\eta = 0$ and $\eta = 1$ these were used in ref. [97]). The $\eta = 2.2$ reference constructed from UA1 data is used in the results presented in the next chapter.

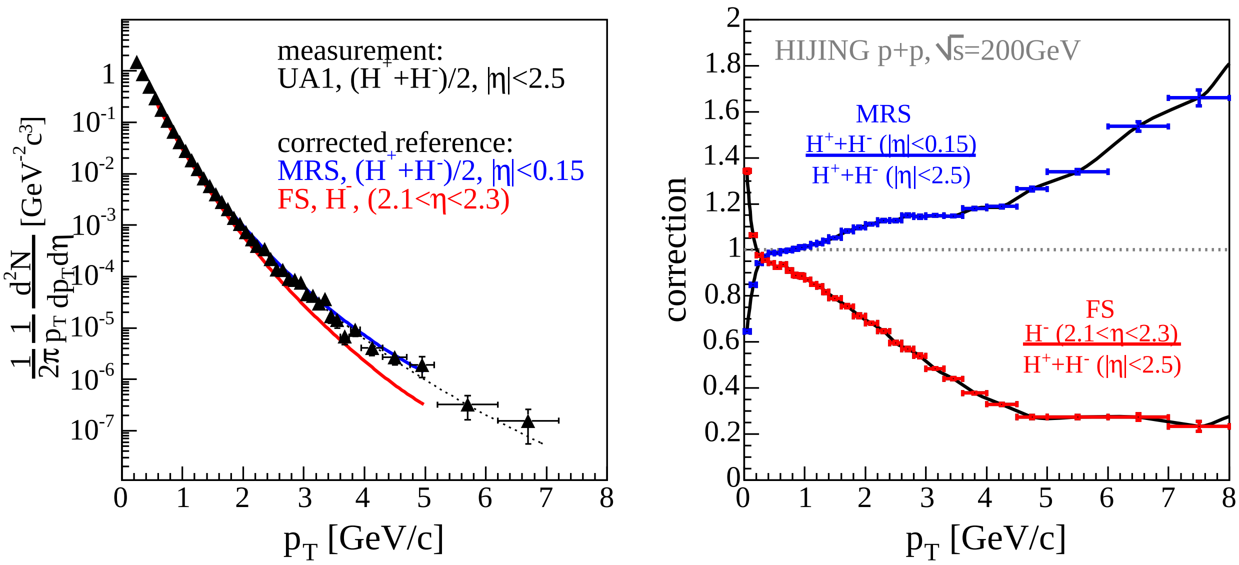

Figure 5.18: The constructed reference spectra and the UA1 $p+\bar{p}$ spectrum at $\sqrt{s_{NN}} = 200\,\text{GeV}$ (left). The correction functions obtained from HIJING simulation (right).

The acceptance of the UA1 experiment is much larger that the acceptance of a BRAHMS spectrometer in a given setting. The published UA1 spectrum shows charged hadrons integrated over $|\eta| < 2.5$, while the BRAHMS acceptance is $|\eta| < 0.15$ (MRS at 90 degrees) and negative hadrons with $2.1 < \eta < 2.3$ (FS at 12 degrees). The UA1 spectrum was corrected for this difference in acceptance using HIJING. Figure 5.18 shows the UA1 spectrum, the obtained reference spectra for the two spectrometer settings (left panel) and the correction functions (right panel). The systematic errors arising from such a correction has not been studied in details. It is assumed that the systematic error is $\lesssim$ 10% for the correction to the MRS acceptance and $\lesssim$ 15% for the correction to the FS acceptance.

The 2003 $\sqrt{s_{NN}} = 200\,\text{GeV}$ Reference

After the long p+p RHIC run (in 2003) hadron spectra at $\eta = 0$ and $\eta = 1$ have been obtained. The spectra are fitted with a function in order to even out the statistical fluctuations in the single bins. The fit function used is $f(p_T) = A(1 + a_1 p_T + a_2 p_T^2)^{-n}$. Figure 5.19 shows the ratio between the spectrum and the fit to the spectrum at the two pseudo–rapidities. The values of A, a_1, a_2 and n are listed on the figure.

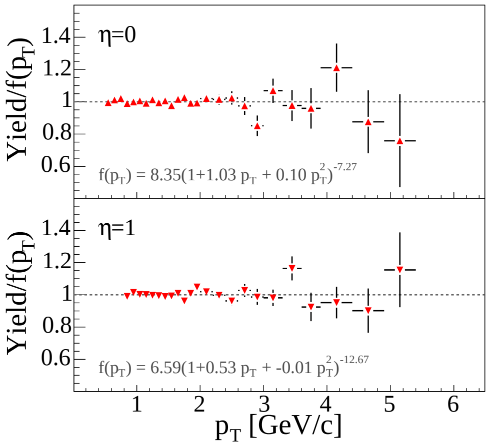

Figure 5.19: Ratio of the reference spectra to the fits.

The $\sqrt{s_{NN}} = 62.4$ GeV Reference

The reference for the $\sqrt{s_{NN}} = 62.4\,\text{GeV}$ is a parametrization of hadron yields from $p + p$ collisions measured at the ISR accelerator. The parametrization is described in ref [102]. The data from the different ISR experiments (and different parameterizations) differ by 10–15%. This difference propagates to the nuclear modification factor. A more systematic study of the hadron yields from p+p collisions is needed to minimize the systematic error introduced by the construction of the reference spectrum.

5.7 Calculating the Number of Binary Collisions

The mean number of binary collisions $\langle N_{bin}\rangle$ can be estimated by using HIJING events as input to a BRAG simulation. Centrality cuts similar to the ones used in the analysis of real data are defined in the (MA) output of the simulation. This gives a certain shape of the impact parameter distribution, which consequently gives a certain shape of the N_{bin} distribution. $\langle N_{bin}\rangle$ is the mean of this distribution. The error on $\langle N_{bin}\rangle$ has one contribution that comes from the systematic uncertainty in the Glauber model approach and one contribution that comes from the simulation of the experimental detector response. The latter is dominated by the uncertainty in the fraction of the inelastic interactions that triggers the detector system, e.g. does the MB trigger pick up 93% or 97% of the inelastic interactions? The systematic uncertainty in the Glauber model calculation comes from details in how the calculation is done and from the uncertainty in the nucleon–nucleon cross section and in the parametrization of the nuclear density function. The errors on $\langle N_{bin}\rangle$ for different centrality classes are therefore highly correlated (and have nothing to do with the widths of the N_{bin} distributions).

		$\langle N_{part}\rangle$	$\langle N_{bin}\rangle$
$Au + Au$	0 – 10%	332±10	897±117
(200 GeV)	10 – 20%	239±10	552±115
	20 – 40%	141±8	259±51
	40 – 60%	59±8	78±26
$Au + Au$	0 – 10%	325	787
(62.4 GeV)	10 – 20%	229	480
	20 – 40%	134	227
	40 – 60%	57	70
$d + Au$	0 – 20%	14.2	13.6±0.3
(200 GeV)	30 – 50%	9.2	7.9±0.4
	60 – 80%	4.6	3.3±0.4
	MB	8.2	7.3±0.3
$p + p$ (200 GeV)		2	1

Table 5.3: Mean number of binary collisions and participants.

The Monte Carlo Glauber of the HIJING model distributes the nucleons in the nuclei according to a Wood–Saxon distribution and requires a minimum distance between nucleons (0.4 fm). For each of the nucleons (in one nuclei) the number of collisions on the way through the other nuclei is calculated. The probability that two nucleons collide is given by a nucleon–nucleon overlap function that depends on the nucleon–nucleon cross section (at the given energy) and the distance between the nucleons. The total number of binary collisions is simply the sum of the number of collisions that each nucleon experiences divided by two. There is a cut–off in impact parameters b – collisions with $b > 25.6$ fm are disregarded. Note, that this approach implicitly neglects energy loss, deflection and excitation as result of a nucleon–nucleon interaction – the first interaction is identical to the last. Other Monte Carlo Glauber models use similar approaches, but with variations in the Wood–Saxon parametrization, the nucleon–nucleon overlap function (and cross section) and the impact parameter cut–off. A slightly different approach is the so–called optical Glauber approach. Here, the individual nucleons are not taken into account. The density profile of the nuclei is defined from a Wood–Saxon distribution, and the density (at a given radius) normalized to the total number of nucleons is interpreted as the probability of finding a nucleon in that specific volume element. Integration (along the z axis) of the product of the two density profiles yields the probability of having n collisions as function of impact parameter. From this quantity the number of collisions and number of participants can be found.

The different Glauber approaches gives slightly different results – the largest discrepancies are in the most peripheral centrality bins. More details on the Glauber model calculations can be found in ref. [103] and references therein. Details on the $\langle N_{bin} \rangle$ and $\langle N_{part} \rangle$ estimations used in various BRAHMS publications can be found in ref. [85]. Table 5.7 lists the $\langle N_{bin} \rangle$ and $\langle N_{part} \rangle$ for the different centralities and collision systems (from ref. [96] and ref.[97]).

The numbers for the $\sqrt{s_{NN}} = 62.4$ GeV have been calculated from HIJING simulations using a centrality cut defined from the charged particle multiplicity in the MA detector acceptance. The errors on these numbers have not been estimated, but they are expected to be of the same size as in the $\sqrt{s_{NN}} = 200$ GeV collisions.

5.8 Systematic Errors

The systematic errors on the spectra are estimated using three different methods:

- By taking the quadratic sum of the systematic error estimated for each of the corrections (see table 5.2). As mentioned, this gives a rough estimation, since these errors are not necessarily independent.
  This estimate gives systematic errors not larger than 10% for spectra obtained in the MRS and 15% for spectra obtained in the FS.

- By comparing the spectra from the different spectrometer settings. The systematic errors can have different effects for different spectrometer settings and the variations in the yields from the different settings reflect the systematic errors. Figure 5.20 shows and example of comparison between yields obtained from different spectrometer settings compared to the average (final yields). In the MRS (left panel), the deviations are on the order of 10% in the low p_T region. In the FS, the estimate is more uncertain, since only few spectrometer settings are used. Since the statistics at high p_T are limited, the systematic errors are difficult to estimate by comparing yields from the different spectrometer settings. However, figure 5.20 shows that the yields from the different settings are consistent at high p_T. Also, the systematic errors are not expected to increase with p_T, since the various corrections are smaller (and easier) to estimate at high p_T. From this method it is estimated that the systematic errors are not larger than 10% for spectra obtained in the MRS and 15% for spectra obtained in the FS.

- By varying the different cuts applied to the data. The variation in the results are associated with

the systematic errors. Figure 5.21 shows comparison between spectra obtained with different cuts and the spectra obtained with the *standard* cuts. The cuts varied are: the vertex range, the $\eta-$range and cut in the edge of the acceptance map (see section 5.4.1).
The deviations (estimated systematic errors) are on the order of 5% for the MRS and 10% for the FS.

Figures 5.20 and 5.21 show the deviations of spectra for the $0-10\%$ most central $Au+Au$ collisions for varying spectrometers settings and cuts. Spectra from other centrality classes and from $p+p$ and $d+Au$ collisions have also been checked and they show similar deviations. The p_T dependence on the systematic errors has not been studied. It is expected that they decrease with increasing momentum, since the average correction is largest (and most uncertain) at low p_T.

In summary, the systematic errors on the spectra are estimated to be at most 10% for spectra obtained in the MRS and at most 15% for spectra obtained in the FS/FFS (in the covered p_T ranges). The systematic errors in the preliminary $\sqrt{s_{NN}} = 62.4\,\mathrm{GeV}$ $Au+Au$ analysis have not been estimated carefully, but they are not expected to be significantly larger than in the $\sqrt{s_{NN}} = 200\,\mathrm{GeV}$ MRS analysis.

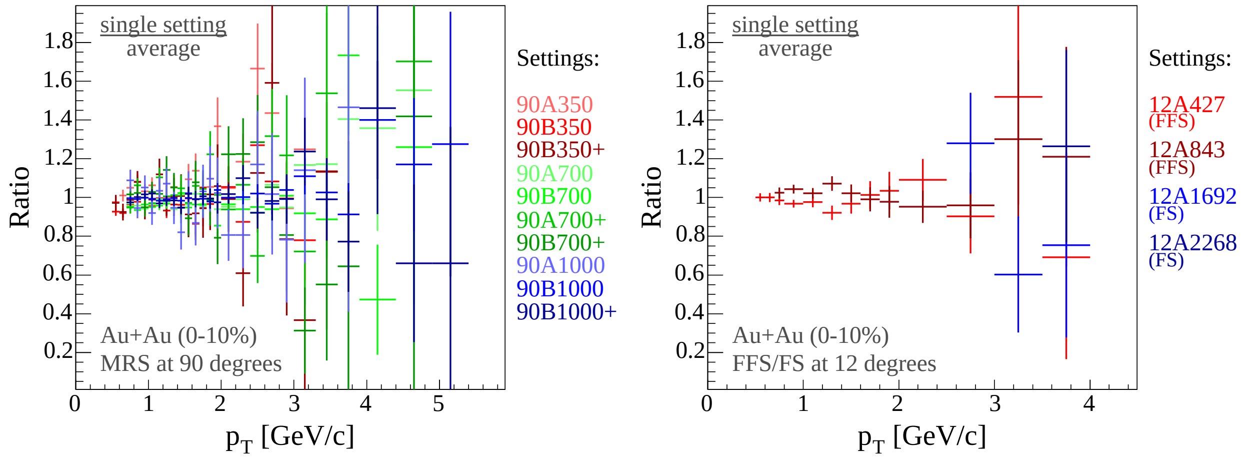

Figure 5.20: Comparison of the yields obtained in the single settings to the average (final) yield as function of p_T for the MRS (left panel) and the FFS/FS (right panel). In the low p_T region, the deviations are within 10%. In the high p_T region, the different spectra are consistent within the statistical errors. Similar analysis have been done for the $p+p$ and $d+Au$ spectra with similar results.

R_{AB} Systematic Error

The systematic errors of the spectra are different from the systematic errors on the nuclear modification factors. It is expected that the dominant part of the systematic errors arising from the acceptance correction, the p_T smearing correction, the efficiency correction, decay correction and bin shift correction cancel out when taking the ratio of the spectra from nucleus–nucleus and from the $p+p$ collisions. The systematic error in the R_{AB} at $\eta = 0$ and $\eta = 1$ is therefore dominated by the systematic error of the $p+p$ trigger efficiency correction (which is $\sim 5\%$). A conservative estimate is that the systematic error here is less than 7%.

For the R_{AuAu} at $\eta = 2.2$ the uncertainty is much larger. This is due to the fact that the $p+p$ reference spectrum is not measured (with the same experiment), but constructed from a $p+\bar{p}$ (UA1) spectrum at the same energy (see section 5.6). The systematic error on the constructed reference has not been studied. A conservative estimate is that the overall systematic error on the R_{AuAu} at $\eta = 2.2$ (including the error on the constructed reference spectrum) is $\lesssim 30\%$.

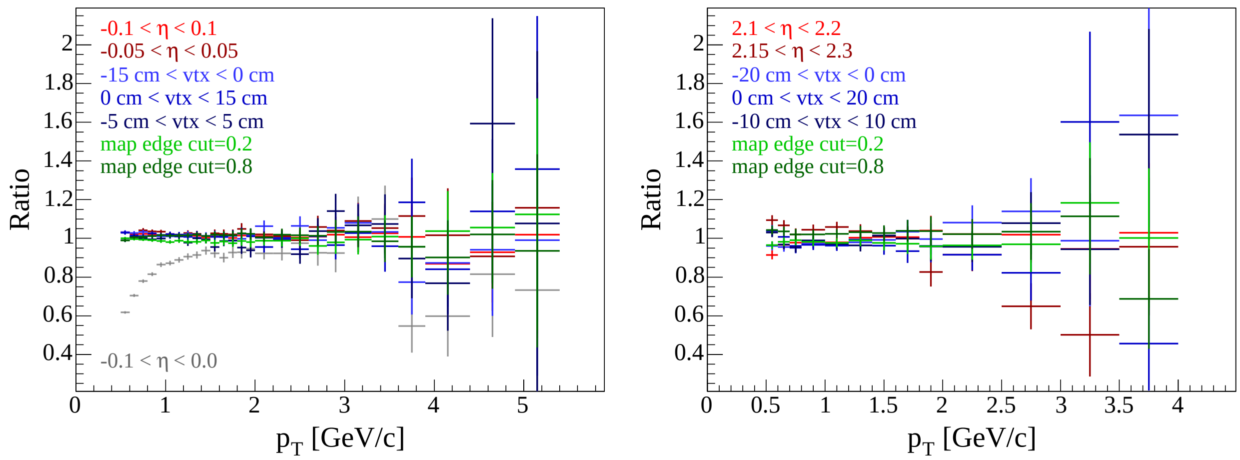

Figure 5.21: Comparison between the spectra obtained with different cuts (to the average) as function of p_T for the MRS (left panel) and FFS/FS (right panel). In the low p_T region, the systematic deviations are on the order of 10% for the FFS/FS and 5% for the MRS. An asymmetric cut in the MRS (gray ratio) gives a large deviation at low p_T – this deviation is due to the fact that only particles of one charge sign is accepted in this region ($\eta < 0$ and $p_T \lesssim 1\,\mathrm{GeV/c}$). This means that the measured yield is not the sum of the yields from positive and negative particles, but only the yields from particles of one charge (this effect is reproduced in the Monte Carlo simulation described in section 5.5). If the cut is symmetric, the deviations (and therefore systematic errors) are small.

The errors on the $\sqrt{s_{NN}} = 62.4\,\mathrm{GeV}$ nuclear modification factors are also large due to the uncertain reference spectrum (see section 5.6). The systematic error is here assumed to be 20%.

The error on the mean number of binary collisions is also considered as a systematic error in the nuclear modification factor. This error is independent of the other systematic errors and are plotted as gray bands (or boxes) around unity. For the $\sqrt{s_{NN}} = 62.4\,\mathrm{GeV}$ collisions, this error has not been estimated, but it is assumed that it is similar to that for the $\sqrt{s_{NN}} = 200\,\mathrm{GeV}$ collisions.

R_{CP} Systematic Error

In the R_{CP} ratios only the systematic errors that depend on the centrality remain. These could be the small centrality dependent differences in detector resolution and efficiency. The systematic errors on the R_{CP} is expected to be smaller than 5%.

The error on the mean number of binary collisions also plays a role here. However, the errors on the mean number of binary collisions in two different centrality classes are highly correlated (see section 5.7). The error on the mean number of binary collisions is set to the error in the most central centrality class $(0-10\%)$, which is a very conservative estimate.

Chapter 6

Results and Discussion

In this chapter the results of the high p_T analysis are presented and discussed. The results are compared to the models described in section 2.4 and to results from the other three RHIC experiments (to check the consistency). Other high p_T measurements supports and refines the conclusions drawn from the measurements of the inclusive hadron yields – these are briefly discussed in the last section of the chapter.

6.1 The Spectra

Figure 6.1 shows the inclusive p_T spectra from $\sqrt{s_{NN}} = 200\,\mathrm{GeV}$ $Au + Au$ collisions for unidentified hadrons at $\eta = 0$ and for negative hadrons at $\eta = 2.2$. The spectra follow the expected power–law shape where the vast majority of particles are produced in the low p_T region. Indeed $\sim 99\%$ of the particles have $p_T < 2\,\mathrm{GeV/c}$. The dashed lines show power–law fits to the spectra. Note that the $\eta = 2.2$ spectra are steeper than the $\eta = 0$ spectra – at higher (pseudo–)rapidities the high p_T component dies out faster than at mid–rapidity.

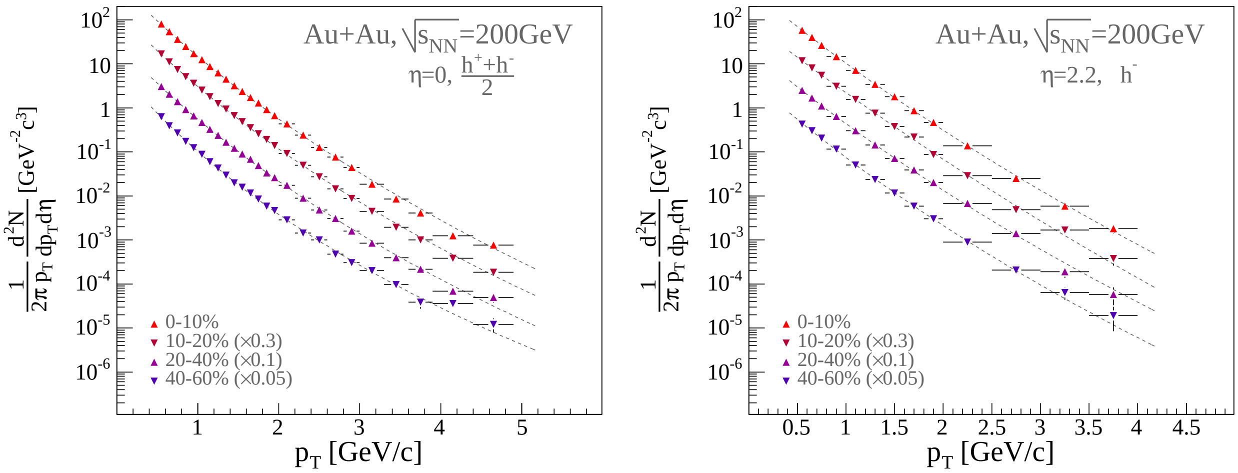

Figure 6.1: Inclusive unidentified hadron yields from $Au + Au$ collisions at $\sqrt{s_{NN}} = 200\,\mathrm{GeV}$. Left panel: charged hadrons at $\eta = 0$. Right panel: negative hadrons at $\eta = 2.2$. Only statistical errors are shown.

Figure 6.2 shows inclusive p_T spectra from $d + Au$ and $p + p$ collisions at $\eta = 0$ and $\eta = 1$. As the $Au + Au$ spectra, both the $d + Au$ and the $p + p$ spectra follow a power–law shape. Figure 6.3 shows the preliminary inclusive p_T spectra from $\sqrt{s_{NN}} = 62.4\,\mathrm{GeV}$ $Au + Au$ collisions at $\eta = 1$ and $\eta = 0.95$.

All the spectra have been fitted with a power–law function. The extracted parameters are listed in table 6.1. The extracted pseudo–rapidity densities dN/dy for the $\sqrt{s_{NN}} = 200\,\mathrm{GeV}$ $Au + Au$ and

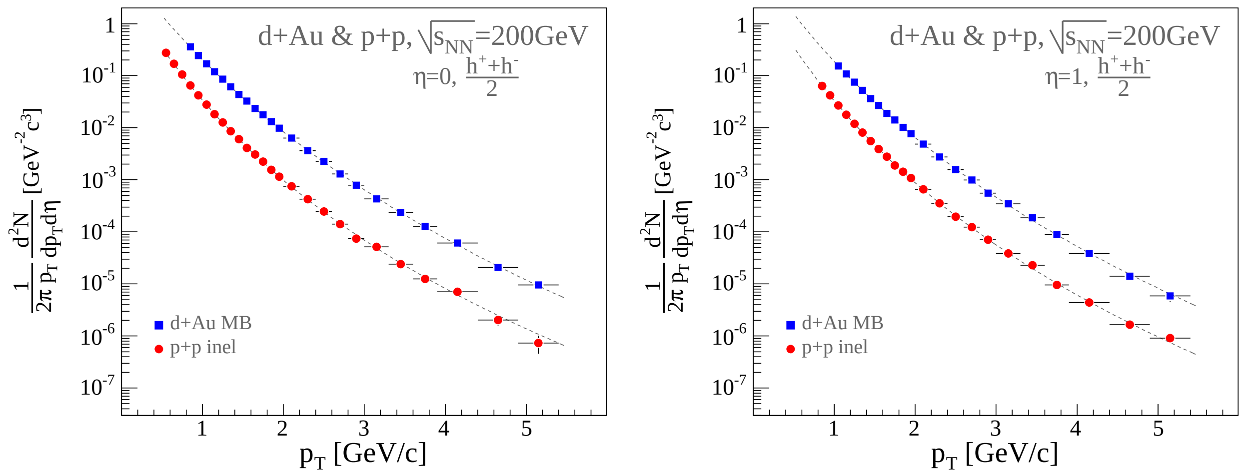

Figure 6.2: Inclusive unidentified hadron yields from $d+Au$ (minimum bias) collisions and $p+p$ (inelastic) collisions at $\sqrt{s_{NN}} = 200\,\text{GeV}$. Left panel: charged hadrons at $\eta = 0$. Right panel: charged hadrons at $\eta = 1$. Only statistical errors are shown.

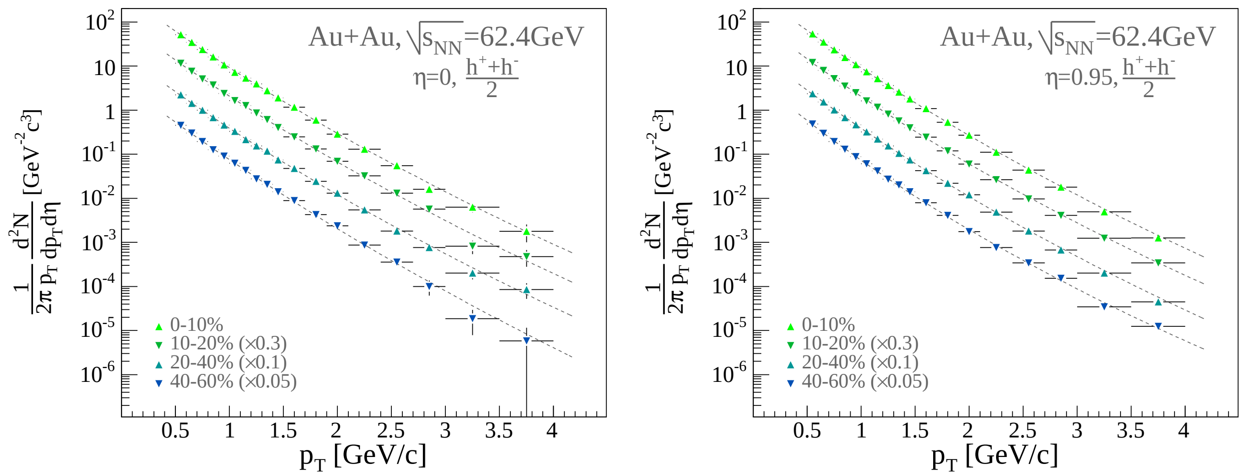

Figure 6.3: Inclusive unidentified hadron yields from $Au+Au$ collisions at $\sqrt{s_{NN}} = 62.4\,\text{GeV}$ at $\eta = 0$ (left panel and $\eta = 0.95$ (right panel). Only statistical errors are shown.

$d+Au$ data are in agreement with measurements obtained from the energy deposit in multiplicity and beam–beam counters [11, 104]. Note that the mean p_T becomes larger for larger collisions systems ($d+Au$ and more central $Au+Au$). In the most central $Au+Au$ collisions the mean p_T is largest, which is expected since the energy density in these collisions is largest.

6.2 The Nuclear Modification

Figure 6.4 shows the nuclear modification factors for the $Au+Au$ collisions at $\sqrt{s_{NN}} = 200\,\text{GeV}$ at the two pseudo–rapidities. At $\eta = 0$, the nuclear modification factor approaches unity around $p_T = 2\,\text{GeV/c}$ for the semi–peripheral collisions $(40-60\%)$. As the collision centrality decreases (more central collisions), the nuclear modification decreases in the high p_T region. For the most central collisions $(0-10\%)$ the yields are suppressed by a factor of approximately 4 as compared to the binary scaled $p+p$ yields. At $\eta = 2.2$ a similar behavior is seen for the negatively charged hadrons: approximate binary scaling in semi–peripheral collisions and strong suppression in central collisions. However, the systematic error from the construction of the reference spectrum and the limited statistics makes the conclusion for the $\eta = 2.2$ data less certain.

		cent. [%]	fit range [GeV]	$dN/d\eta$	p_0 [GeV/c]	n	$\langle p_T \rangle$ [MeV/c]
		$\sqrt{s_{NN}} = 200$ GeV					
$Au+Au$	$\eta=0$	$0-10$	$0.5-5.0$	290±1	4.74±0.13	20.38±0.44	545.8±1.4
		$10-20$	$0.5-5.0$	203±1	4.24±0.13	18.69±0.44	541.0±1.7
		$20-40$	$0.5-5.0$	112±1	4.06±0.18	17.99±0.61	541.1±2.6
		$40-60$	$0.5-5.0$	47.7±0.7	2.72±0.12	13.84±0.41	502.4±3.9
$Au+Au$	$\eta=2.2$	$0-10$	$0.5-5.0$	210±3	7.19±0.92	30.37±3.31	525.2±4.5
(h^-)		$10-20$	$0.5-5.0$	140±2	10.69±2.18	42.38±7.74	542.6±5.2
		$20-40$	$0.5-5.0$	90.5±2.3	6.22±1.13	26.84±4.04	521.6±7.3
		$40-60$	$0.5-5.0$	33.3±1.3	5.40±1.43	24.51±5.36	502.3±10.8
$d+Au$	$\eta=0$	MB	$0.8-5.5$	4.49±0.05	2.66±0.06	13.22±0.20	521.3±3.0
	$\eta=1$	-	$1.0-5.5$	4.99±0.20	2.21±0.13	12.40±0.40	470.2±11.3
$p+p$	$\eta=0$	Inel	$0.8-5.5$	1.20±0.04	1.65±0.08	11.06±0.28	410.7±7.4
	$\eta=1$	-	$0.8-5.5$	1.26±0.03	1.67±0.06	11.43±0.21	397.3±5.9
		$\sqrt{s_{NN}} = 62.4$ GeV					
$Au+Au$	$\eta=0$	$0-10$	$0.5-4.0$	185±3	6.43±0.68	27.21±2.40	530.8±5.2
		$10-20$	$0.5-4.0$	137±2	6.87±0.76	28.71±2.63	534.6±5.1
		$20-40$	$0.5-4.0$	78.6±1.4	6.78±0.86	28.67±3.07	528.0±5.5
		$40-60$	$0.5-4.0$	31.8±0.9	7.82±1.49	33.56±5.52	511.9±8.2
$Au+Au$	$\eta=0.95$	$0-10$	$0.5-4.0$	193±1	6.02±0.20	26.46±0.73	512.9±1.5
		$10-20$	$0.5-4.0$	146±1	5.59±0.26	24.89±0.94	510.6±1.8
		$20-40$	$0.5-4.0$	85.7±0.4	5.71±0.15	25.69±0.54	503.3±1.5
		$40-60$	$0.5-4.0$	35.5±0.3	4.44±0.21	21.47±0.84	480.6±2.9

Table 6.1: Extracted fit parameters. Note that the errors are statistical only. Errors on the dN/dy therefore do not reflect the uncertainty the extrapolation to the lowest p_T range.

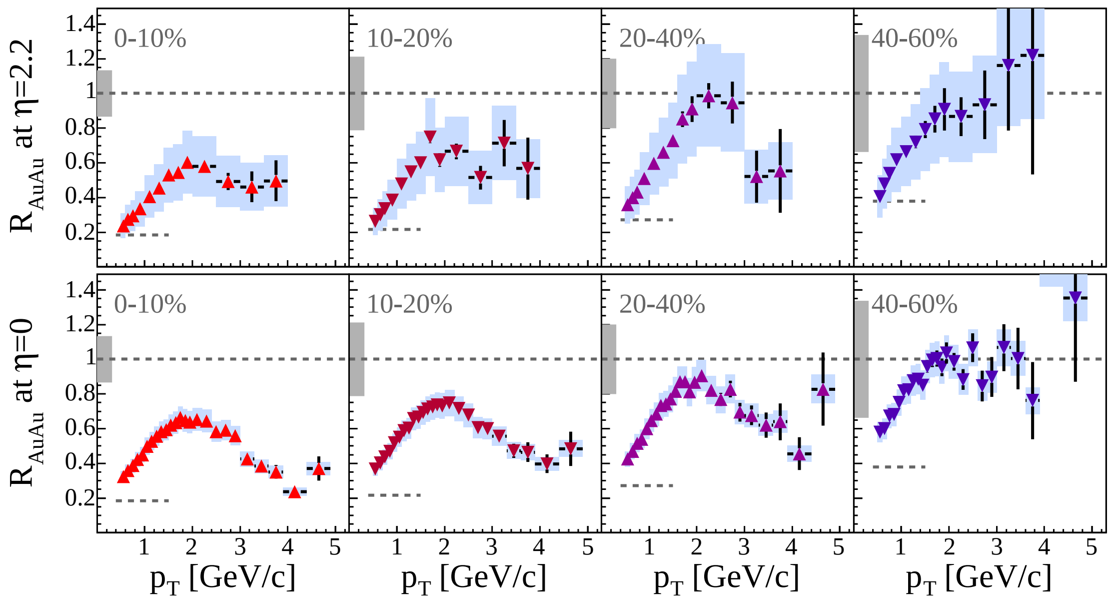

Figure 6.4: The nuclear modification factors for $Au + Au$ collisions at $\sqrt{s_{NN}} = 200$ GeV at the two different pseudo–rapidities, $\eta = 0$ (bottom panels) and $\eta = 2.2$ (top panels). The gray boxes to the left in each panel indicate the $\langle N_{bin} \rangle$ normalization error. The error bars show the statistical errors while the boxes indicate the estimated systematic uncertainties. The lower dashed lines show the $\langle N_{part} \rangle$ scaling.

Figure 6.5 shows the nuclear modification factors for the $Au+Au$ collisions at $\sqrt{s_{NN}} = 62.4\,\text{GeV}$ at $\eta = 0$ and $\eta = 0.95$. The nuclear modification is similar at the two pseudo–rapidities. In the central collisions it indicates a small suppression in the high p_T region. However, with the systematic errors on the used reference spectrum (see section 5.6) suppression cannot be concluded. For more peripheral collisions the nuclear modification factor rises above one. The Cronin enhancement due to multiple scattering, is at this collision energy expected to be more pronounced than at $\sqrt{s_{NN}} = 200\,\text{GeV}$, since the spectra are steeper (see section 2.3.1).

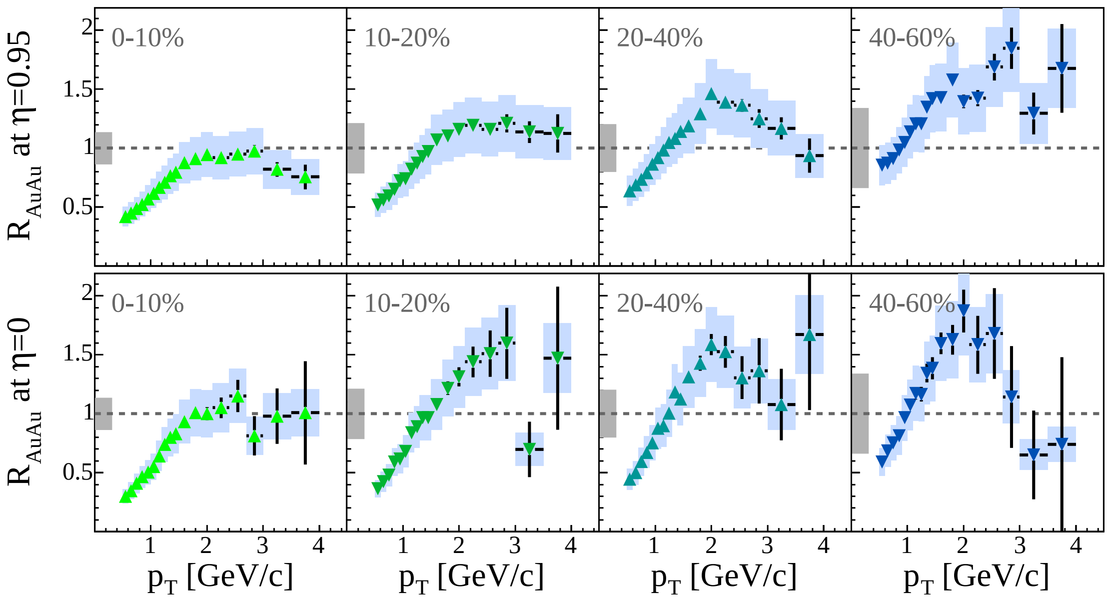

Figure 6.5: The nuclear modification factors for $Au + Au$ collisions at $\sqrt{s_{NN}} = 62.4\,\text{GeV}$ at the two different pseudo–rapidities, $\eta = 0$ (bottom panels) and $\eta = 0.95$ (top panels). The behavior of the nuclear modification factor is the same at the two pseudo–rapidities.

By taking the ratio of the central to the semi–peripheral (the R_{CP} ratio) most of the systematic errors cancel out (see section 5.8). Since the nuclear effect is expected to play a relatively small role for the semi–peripheral collisions, the R_{CP} ratio is expected to show a similar behavior as the R_{AuAu} for the central collisions – however with smaller systematic errors.

The measured R_{CP} for $Au + Au$ collisions at $\sqrt{s_{NN}} = 200\,\text{GeV}$ supports the conclusion drawn from the measured nuclear modification factor (this is important at $\eta = 2.2$ where the systematic errors are large). The yields in the central $Au + Au$ collisions at $\sqrt{s_{NN}} = 200\,\text{GeV}$ are significantly suppressed as compared to the semi–peripheral or elementary collisions, when scaled by the number of binary collisions.

The suppression evidences strong nuclear effects. As described in section 2.3.5 the suppression in the central $Au+Au$ collisions must be related to energy loss of the produced jets in the medium. The question is, if the suppression can be explained by hadronic energy loss (re–scattering). Wang argues that the "detailed analysis of jet quenching data concludes that the data are not compatible with such a scenario of hadronic absorption and that the observed patterns of jet quenching in heavy–ion collisions at RHIC are the consequence of parton energy loss" [105]. The conclusion of the studies by Cassing, Gallmeister and Greiner, was also that the hadronic re–scattering could not reproduce the observed suppression pattern (see section 2.4.3). The magnitude of the suppression can apparently only be described by gluon radiation in the medium. The energy density of the medium has been estimated from the suppression pattern by different assumptions on the energy loss mechanism in ref. [56]. It is found that the energy density of the created medium is in the range $12 - 20\,\text{GeV/fm}^3$.

The suppression in the $\sqrt{s_{NN}} = 200\,\text{GeV}$ data at the forward pseudo–rapidity can be interpreted in a simple static picture where the suppression amplitude scales with the integrated gluon density

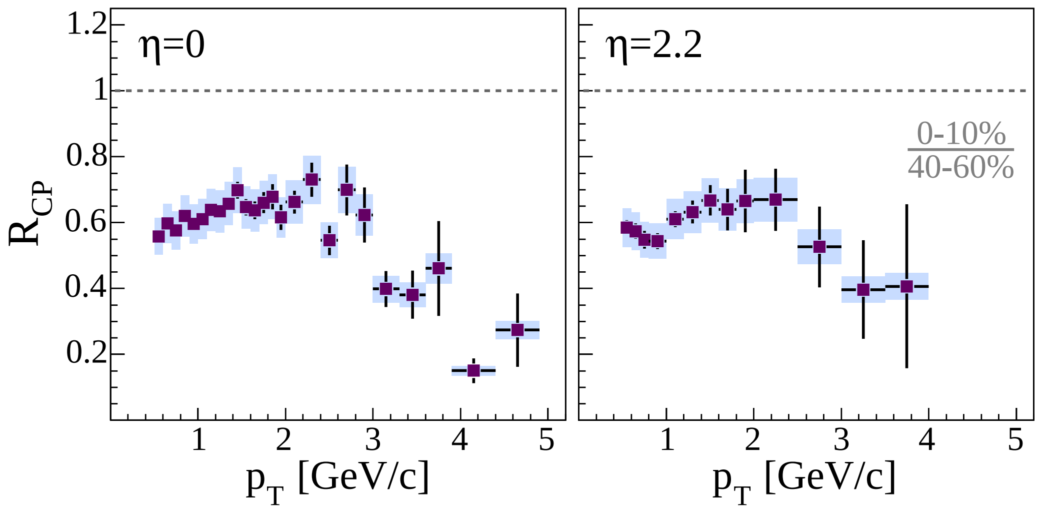

Figure 6.6: R_{CP} for $Au+Au$ collisions at $\eta = 0$ (left panel) and $\eta = 2.2$ (right panel). The yields in the central collisions are suppressed compared to the semi–peripheral, when scaled by $\langle N_{bin} \rangle$. This measurement supports the conclusions based on the (more uncertain) R_{AuAu} ratio. The suppression is similar at the two pseudo–rapidities.

on the way out of the medium. Since the charged particle density is directly related to the gluon density, the suppression amplitude should scale with the charged particle (pseudo–rapidity) density. This interpretation is in agreement with the observation that both the suppression patterns and the charged particle density at $\eta = 0$ and $\eta = 2.2$ are similar.

However, this picture does not take the longitudinal expansion of the medium into account. Around mid–rapidity, the medium expands in the same direction (outward) as the jets. At higher pseudo–rapidities the high p_T particles move through a medium that expands both longitudinally and radially. The energy loss is governed by the velocity difference between the medium and the high momentum particle at all times as the particles traverses the medium. Interpretation of the high p_T suppression at higher pseudo–rapidities is therefore more complicated and it must be based on assumptions on the longitudinal expansion of the medium. Hirano and Nara have modeled the jet–quenching in an expanding hydrodynamical medium [70] and reproduced the observed suppression at both pseudo–rapidities (see section 2.4.4). Their study "suggests that the longitudinal region of dense partonic matter produced in $Au + Au$ collisions reaches to $\eta \sim 2$ and that the strong hadron suppression at off–midrapidity is consistent with the final state parton energy loss in the medium.". Their calculations predicts a suppression at $\eta = 3.25$ similar to that at $\eta = 0$ (and $\eta = 2.2$), even though the charged particle density here is only around 2/3 of the value in the mid–rapidity region [11].

The effect of saturation at higher pseudo–rapidities in the $Au + Au$ collisions have not been investigated in the literature. As discussed in section 2.3.3, the saturation scale depends on the rapidity difference between the initial parton and the produced hadron. This means that the nuclear modification factor at high rapidities is sensitive to the low$-x$ partons in the nucleus with the rapidity of the opposite sign (the nucleus moving away from the detector). But the nuclear modification factor also probes partons of higher x in the other nucleus (that moves in the direction of the detector) and here the parton distribution is enhanced (due to the so–called anti–shadowing). If the two effects cancel out in a symmetric collision is not know, but it is expected that the effect of saturation is less pronounced in symmetric than in anti–symmetric collisions.

In the $d + Au$ collisions, the nuclear modification factors have a very different behavior – they rise above unity in the high p_T region as shown in figure 6.7. At $\eta = 0$ the R_{dAu} reaches a value of approximately 1.3 for $p_T > 2.5\,\text{GeV/c}$. At $\eta = 1$ it is closer to unity. The nuclear modification factor for central $Au + Au$ collisions (at the same energy, $\sqrt{s_{NN}} = 200\,\mathrm{GeV}$) is indicated on the left panel in figure 6.7 as a dashed line for comparison.

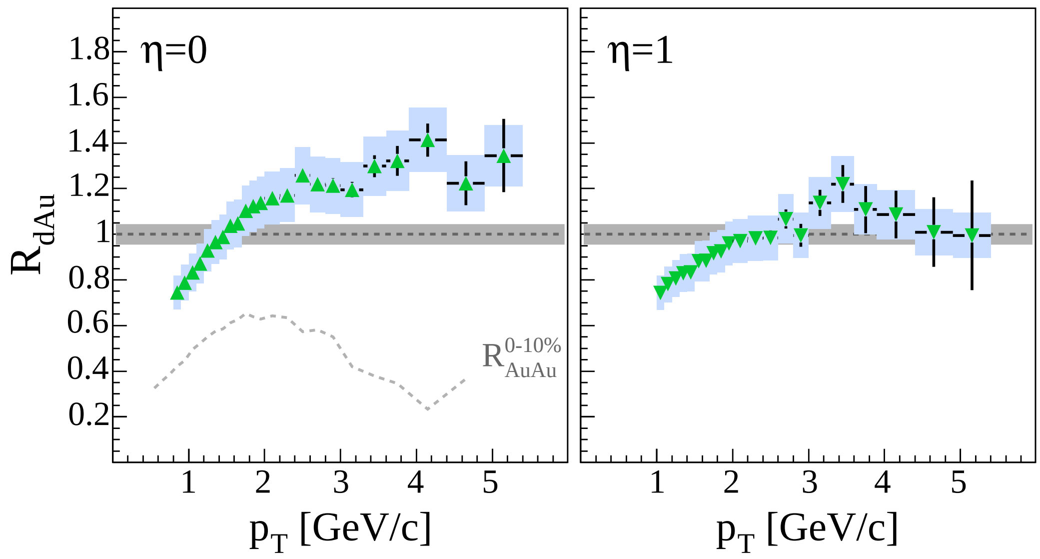

Figure 6.7: Nuclear modification factor for minimum bias $d + Au$ collisions at $\eta = 0$ (left panel) and $\eta = 1$. The dashed line in the $\eta = 0$ panel indicates the nuclear modification factor for central $Au + Au$ collisions.

The enhancement compared to the binary scaled $p + p$ collisions has been explained by multiple scattering in the initial (and final) state, but also quark recombination models reproduce the enhancement. These theoretical ideas were discussed in section 2.3.1. The definitive conclusion that can be drawn from the observed enhancement is that the suppression in the central $Au + Au$ cannot be due to modification of the initial parton distributions in the Au nuclei. Shadowing and saturation effects thus play a minor role at these energies, at least around mid–rapidity. If the enhancement in the R_{dAu} is due to multiple scattering in the initial state, it should be expected that this effect also enhances the yield in the $Au + Au$ collisions. Considering this, the jet quenching effect in the central $Au + Au$ collisions seems even stronger.

The fact that R_{dAu} decreases from $\eta = 0$ to $\eta = 1$ is in agreement with saturation predictions (see section 2.3.3). Other measurements indicate that the trend continues at higher pseudo–rapididties [97]. These observations favor the saturation explanation of the shadowing effect. McLerran argues that shadowing (explained in the multiple scattering approach) will lead to a stronger Cronin enhancement at forward rapidities since the probe propagates through more matter in the nucleus [75]. This should be seen in contrast to shadowing explained by saturation, where the nuclear modification factor is expected to decrease with increasing pseudo–rapidity.

The decrease in the R_{dAu} with pseudo–rapidity is an intriguing observation, but the data (and the present state of the theoretical work) is not detailed enough to make any definitive conclusions in this direction. Even McLerran (and Gyulassy) are careful not to make definitive conclusions. When discussing the created quark gluon plasma at RHIC, they argue that "there is growing evidence that its source is well described by a saturated gluon CGC initial state". The decrease in R_{dAu} with increasing pseudo–rapidity is also predicted by quark recombination (see section 2.3.1) or it could simply be due to the decrease in pseudo–rapidity density. More $d + Au$ (or $p + Au$) data at higher rapidities is needed to understand whether saturation effects play a role at this energy.

Figure 6.8 shows another representation of the high p_T data for $Au + Au$ collisions at $\sqrt{s_{NN}} = 200\,\mathrm{GeV}$. The nuclear modification factor in the high p_T region is plotted as function of the number of participants at the two pseudo–rapidities. The behavior at $\eta = 0$ and $\eta = 2.2$ is similar. The strong decrease in the $Au + Au$ data shows how the jet–quenching sets in as the collision zone gets larger. The $d + Au$ nuclear modification is shown on the $\eta = 0$ plot. It follows the trend from the $Au + Au$ data.

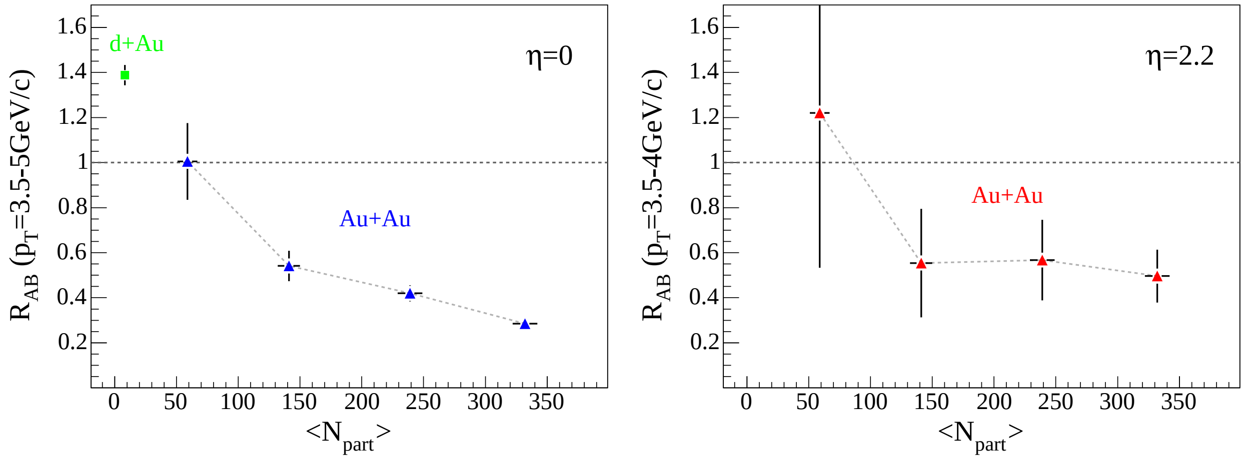

Figure 6.8: Left panel: R_{AB} at $\eta = 0$ in the p_T range from 3.5 to 5 GeV/c as function of the mean number of participants. Right panel: R_{AB} (for negative hadrons) at $\eta = 2.2$. The trend is similar to that observed at $\eta = 0$.

Energy Dependence

The high p_T data from heavy ion collisions at the SPS are sparse and the suppression studies are difficult due to large uncertainties in the parametrization of the reference spectrum.

Only two high p_T measurement in collision systems comparable to $Au + Au$ were carried out at SPS energies: The WA98 measurement of π^0 yield in $Pb + Pb$ collisions [106] and the CERES measurement of $\pi^\pm$ in $Pb+Au$ collisions [107], both at $\sqrt{s_{NN}} = 17.3$ GeV. Reference spectra have not been measured directly and the parameterization of the reference is somewhat uncertain [108]. Figure 6.9 shows the nuclear modification factor using different reference parameterizations. Regardless of what reference parametrization is used, the measurements show an enhancement in the high end of the measured p_T spectra ($p_T \approx 4$ GeV/c).

In ref. [108] it is argued that in central heavy ion collisions the "data appear to be consistent within errors with the pertubative expectations of scaling with the number of nucleon–nucleon collisions". In other word, the data are consistent with a nuclear modification factor around unity. The argument is based on the uncertainty in the reference spectrum. A nuclear modification factor around unity is approximately a factor of two lower than the expectation (which includes a Cronin enhancement). On this basis, it is concluded that already at SPS, jet–quenching plays an important role in the high p_T particle production. On the other hand Wang argues that the nuclear modification factor in central collisions at the SPS is "consistently above 1 due to strong Cronin effect via initial multiple scattering, leaving not much room for large parton energy loss." [110].

The reference for the measured $\sqrt{s_{NN}} = 62.4$ GeV data is also somewhat uncertain (see section 5.6). Around $p_T = 4$ GeV/c the nuclear modification factor in the central collisions is slightly lower than unity, but with the uncertainty on the reference it is consistent with unity.

Figure 6.10 shows the nuclear modification factor for central heavy ion collisions around $p_T = 4$ GeV/c as function of collision energy. The energy dependence of the nuclear modification shows a clear trend. At SPS energy the nuclear modification is higher than one, at $\sqrt{s_{NN}} = 62.4$ GeV the suppression starts to set in and at the top RHIC energy the yields are strongly suppressed.

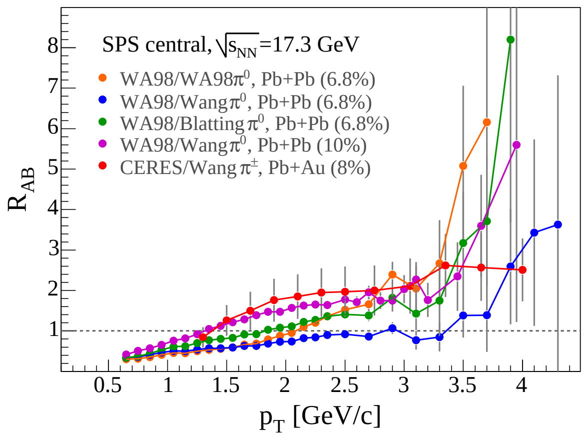

Figure 6.9: Nuclear modification factor (around $\eta = 0$) for pions in central heavy ion collisions at the top SPS energy. The data are from WA98 and the CERES experiments. The reference spectra are from refs. [108] and [109].

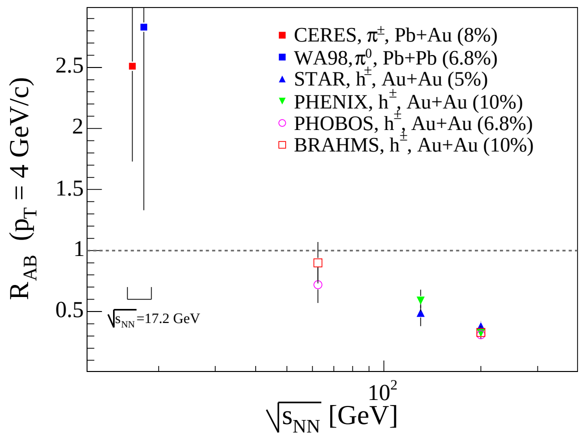

Figure 6.10: The nuclear modification factor (around $\eta = 0$) in central heavy ion collisions as function of center–of–mass energy.

6.2.1 Comparison to Models

In the previous sections the data were discussed qualitatively and conclusion from the nuclear modifications were drawn. This sections presents a single quantitative comparison between the models described in section 2.4 and the measurements. The comparison is only done for central $Au + Au$ collisions at $\eta = 0$ where predictions from all the models have been published. Figure 6.11 shows nuclear modification factor $\eta = 0$ for central $Au + Au$ collisions at $\sqrt{s_{NN}} = 200\,\mathrm{GeV}$ as obtained by the different models and the measurement. In general, the quantitative agreement between the model calculations and the data is not very convincing. However, some of the quantitative features are reproduced. HIJING (which was developed long before the measurements were done) is in good agreement with the data at low p_T. At higher p_T it undershoots the data. This can be explained by the very schematic jet quenching mechanism introduced in the model.

The Vitev–Gyulassy model does not consider the soft physics and is not expected to be able to reproduce the low p_T range of the spectrum. That the data lies above the prediction in the p_T range from $2 - 3.5\,\mathrm{GeV/c}$ could be explained by the contribution from the thermal component in this region (which is not considered in the model). At $p_T \approx 4\,\mathrm{GeV/c}$ the model is in agreement with the data. The model predicts essentially no p_T dependence for $p_T = 4 - 10\,\mathrm{GeV/c}$, which is in agreement with data from STAR and PHENIX (see next section). The yellow band covers the region obtained by varying the initial gluon rapidity density (at $y = 0$) from 800 to 1200.

The Cassing–Gallmeister–Greiner model gives a too large nuclear modification factor from $p_T > 2\,\mathrm{GeV/c}$. The overprediction could be related to underestimation of the energy loss in the pre–hadronic phase (see section 2.4.3).

The Hirano–Nara model shows the best agreement with the data. The energy loss is calculated using the same energy loss mechanism as the Vitev–Gyulassy model and gives similar result in the high p_T range. The (correct) behavior in the low p_T range is obtained by the detailed hydrodynamical description of the bulk matter production. The model predicts a similar suppression at $\eta = 2.2$, which is in agreement with the measurement (see figure 6.4).

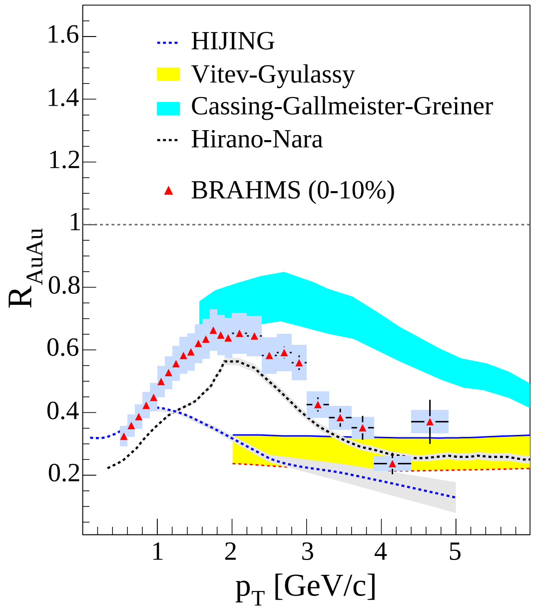

Figure 6.11: Model calculations of the nuclear modification factor at $\eta = 0$ for central $Au + Au$ collisions at $\sqrt{s_{NN}} = 200\,\mathrm{GeV}$ compared with the data.

6.3 Consistency of RHIC Results

This section presents a comparisons of the high p_T measurements from the four different RHIC experiments. Comparison is only possible for unidentified hadrons around mid–rapidity, since this is where all four experiments are able to measure.

The different experiments have used different reference spectra in their papers on high p_T suppression. Figure 6.12 shows a comparison. The spectra are divided by an arbitrary power–law function to make the comparison easier.
STAR has measured directly the charged hadrons from $p + p$ collisions. A correction is applied to take into account the difference between the measured spectrum and that from all inelastic collisions (similar to the one described in section 5.4.2). **PHENIX** has constructed the $N + N$ reference from the measured π^0 yields. A simple parametrization of the neutral pion to hadron ratio π^0/H (constant above $p_T = 1.5\,\mathrm{GeV/c}$) have been used to correct a power–law fit to the π^0 yields. Details can be found in ref. [111]. **PHOBOS** has used a power–law fit to the charged hadron spectra from UA1 [101] ($p + \bar{p}$ at the same energy). A correction for the difference in the PHOBOS and UA1 acceptance was applied (based on PYTHIA). **BRAHMS** has used a fit to the UA1 spectrum as explained in section 5.6. This is labeled BRAHMS 2002 in the figure. The BRAHMS 2003 curve represent the reference used in this work.

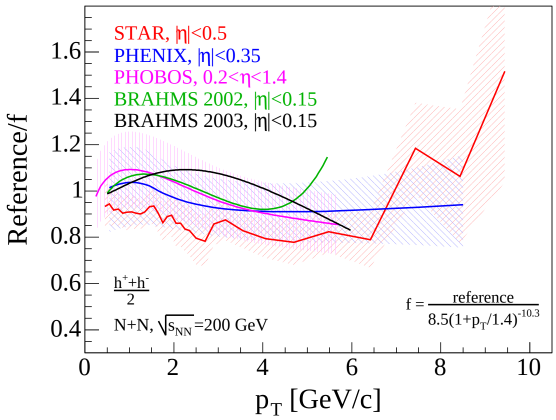

Figure 6.12: Comparison between the reference spectra used by the different experiments after the 2002 $Au + Au$ run. The hatched areas indicate the quoted errors. Note that the acceptance of the four experiment are different.

Within the quoted errors, the results are consistent. It should be noted that a direct comparison is not correct, since the acceptances of the detectors are different. However, the difference in the yields due to the different acceptances is less than 2% for $p_T > 0.5\,\mathrm{GeV/c}$ according to PYTHIA.

The Nuclear Modifications

Figures 6.13 and 6.14 show comparison of the nuclear modification factor at $\eta \approx 0$ in central $Au+Au$ collisions and in minimum bias $d+Au$ collisions. The data from STAR, PHENIX and PHOBOS are shown as simple curves (without errors) for clarity. The data are remarkably consistent. The $Au+Au$ data are from refs. [112], [111] and [113]. The $d+Au$ data are from refs. [114], [115] and [116].

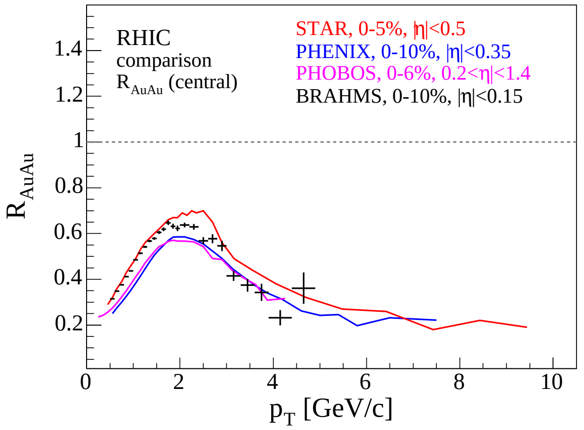

Figure 6.13: Comparison between the nuclear modification factors for central $Au+Au$ collisions measured by the four experiments.

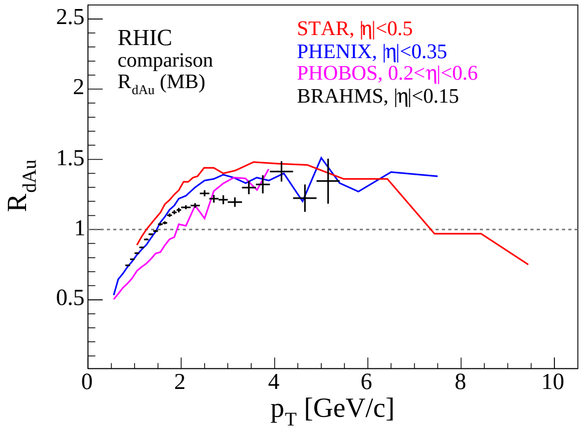

Figure 6.14: Comparison between the nuclear modification factors for minimum bias $d+Au$ collisions measured by the four experiments.

6.4 Other High p_T Measurements

The suppression pattern of the high p_T unidentified charged hadrons at the maximum RHIC energy evidences jet quenching and thereby the existence of an extremely dense medium created in the collisions. The measurements are refined and the conclusion strengthened by other high p_T measurements. In particular, the data on identified hadrons and on the azimuthal angle correlation of high p_T hadrons show interesting features.

6.4.1 Identified Particles

The PHENIX collaboration has measured the proton to pion ratio up to $p_T = 4.5\,\mathrm{GeV/c}$ in central $Au+Au$ collisions [117]. The ratios show, that above $p_T \approx 2.5\,\mathrm{GeV/c}$ the protons (and anti–protons) are as abundant as the pions. The p/π^+ and $\bar{p}/\pi^-$ ratios are much higher than the ratios from pQCD calculations or from the measured ratios in jets created in elementary collisions. PHENIX has also measured the proton and anti–proton yields in both central and peripheral $Au+Au$ collisions. The proton and anti–proton R_{CP} ratio shows that in the range $p_T = 2-4.5\,\mathrm{GeV/c}$ the proton and anti–proton yields in central collisions scales with the binary scaled yields in the very peripheral collisions. This is shown in figure 6.15. The large suppression in the hadronic yield in this p_T region is consequently due to suppression of the mesons.

The observations have been explained by the strong collective radial flow which boosts the heavier baryons to higher p_T. The thermal radial boosted source thus plays a role at $p_T = 3 - 4\,\mathrm{GeV/c}$. Quark recombination (or coalescence) models predict a similar baryon enhancement [118, 119]. The different theoretical descriptions all predict that the baryon to meson ratio decreases for higher p_T and returns to the pQCD expectation.

Information on the baryon/meson ratio at higher p_T can be extracted by studying the hadron to π^0 ratio, which has been measured by PHENIX [117]. The results indicate that the baryons are enhanced in the region up to $p_T \approx 5\,\mathrm{GeV/c}$. Above this p_T the hadron to π^0 ratio settles around the value observed in elementary collisions and at lower energies. This observation is supported by the STAR measurements of the R_{CP} strange mesons (K_S^0) and baryons (Λ). While the R_{CP} for mesons peaks around $p_T \approx 2\,\mathrm{GeV/c}$ the R_{CP}^{Λ} peaks at a higher p_T (around $3 - 4\,\mathrm{GeV/c}$) and decreases to reach the meson R_{CP} at around $5 - 6\,\mathrm{GeV/c}$.

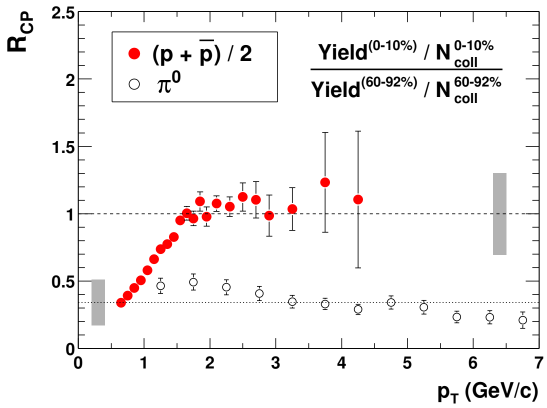

Figure 6.15: R_{CP} for protons/anti–protons and neutral pions measured by the PHENIX experiment [117].

Detailed measurements of identified particles to very high p_T can reveal information on the fragmentation and recombinations processes in the strongly interaction medium. Especially deviations from the relative particle abundances observed in elementary collisions can lead to new discoveries on the strongly interacting medium.

Measurements and theoretical implications of the high p_T identified hadron yields seen from a BRAHMS perspective are discussed in details in ref. [95].

6.4.2 Back-to-back Jets

With the 2π azimuthal coverage of the STAR tracking system, the back–to–back correlation of produced jets can be studied. In $p + p$ collisions two back–to–back jets can be directly identified as particles emitted within the narrow jet cones. In the high multiplicity environment created in heavy ion collisions the jets cannot be reconstructed and jet studies can only be carried out statistically. The procedure is to look for a high p_T (*trigger*) particle ($p_T = 4 - 6\,\mathrm{GeV/c}$) and study the azimuthal angular correlation with all semi–hard particles ($p_T = 2 - 4\,\mathrm{GeV/c}$) coming from the collision. A jet will show up as a peak in the correlation function, since it typically consist of a very hard particle (the leading hadron) and a number of semi–hard particles within the jet cone (see section 2.1). The jet emitted in the opposite direction (away side) will show up as another peak, shifted by π from the peak of jet that contains the *trigger* particle. The presence of a dense absorbing medium will suppress the away–side peak. In the case of an extremely dense medium, only jets produced on the surface will survive.

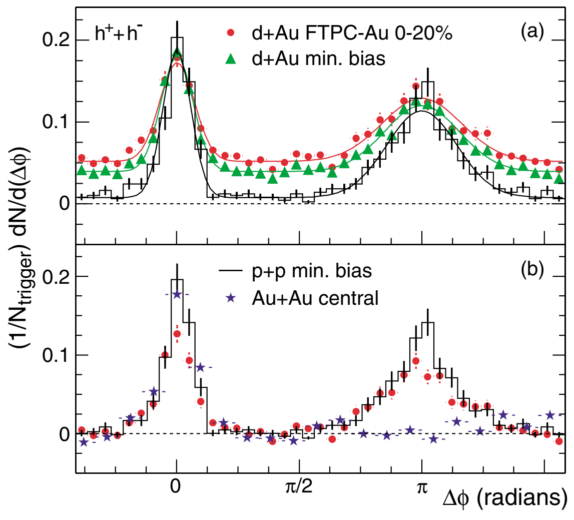

Figure 6.16: Azimuthal angular correlation in $p + p$, $d + Au$ and $Au + Au$ collisions. The disappearance of the away side peak in the $Au + Au$ collisions evidences the quenching of jets in the dense medium.

Figure 6.16 shows the azimuthal angular correlation function measured by STAR [114]. The top panel shows the azimuthal angular correlation in $d + Au$ (MB and $0 - 20\%$ central) and in $p + p$ collisions. The correlation due to the away side jet is clearly visible in both the $p + p$ and $d + Au$ collisions as a peak around π. The bottom panel shows the correlation in $p + p$, $d + Au$ and central $Au+Au$ collisions. Here, the known background (from the thermal particle production) is subtracted, i.e. the level of the correlation function is zero around $\pi/2$. The striking feature is the clear difference between the away side correlation in the $d + Au$ and the $Au + Au$ collisions. In $d + Au$ collisions the away side jet is only slightly broadened as compared to the $p + p$ data, which indicates that the cold nuclear medium created in these collisions does not affect the produced high p_T substantially. In the central $Au + Au$ collisions, the away side jets are fully absorbed. Such a direct measurement of the absorption of jets in heavy ion collisions was first proposed by Bjorken in 1983: "An interesting signature may be events in which the hard collision occurs near the edge of the overlap region, with one jet escaping without absorption and the other fully absorbed." [120].

More detailed studies show that the suppression of the away side jet is correlated with the direction of the jet relative to the event plane [121]. Jets produced in the direction of the event plane is less suppressed than jets going out of the event plane. This is expected since the particles on average travel through a longer distance in the suppressing medium when they travel in the direction of the event plane. Also, particles on the away side (opposite a high momentum particle) have a slightly higher momentum than the average particles [122]. This supports the picture that the jets are absorbed in the medium and the energy of the jet is converted into heat (higher energy density) in the system. In summary, the statistical study of di–jet and mono–jet production gives additional confidence that jets produced in the central $Au + Au$ are quenched in the dense medium. It also provides a unique possibility to study the jet attenuation as function of the extension of the suppressing medium.

Chapter 7

Conclusion

In this work, measurements of the nuclear modification factor R_{AB} in $Au + Au$ and $d + Au$ at the top RHIC energy $\sqrt{s_{NN}} = 200\,\mathrm{GeV}$ have been measured and presented. The R_{AuAu} have been measured for charged hadrons at $\eta = 0$ and for negative hadrons at $\eta = 2.2$. The measurement indicates a strong suppression in the high p_T yields in central collisions at both pseudo–rapidities – at $p_T = 5\,\mathrm{GeV/c}$ the yields are suppressed by a factor of ~ 4 as compared to the binary scaled yields from elementary collisions. The suppression decreases as the centrality increases and for the mid–central collisions $(40 - 60\%)$ the nuclear modification factor approaches unity in the high p_T region. The nuclear modification factor in the $d + Au$ data shows a very different behavior. At $\eta = 0$ it rises above unity ($R_{dAu} = 1.3$ at $p_T = 4\,\mathrm{GeV/c}$). At $\eta = 1$ it is closer to unity. This *null* experiment was performed in order to understand the effect of the denser medium created in the $Au + Au$ collisions and disentangle the nuclear modifications arising from initial state (shadowing/saturation) and final state (jet–quenching) effects. The observed enhancement in $d + Au$ rules out shadowing/saturation as explanation of the strong suppression in the central $Au + Au$ collisions. The suppression in the $Au + Au$ must primarily be due to jet–quenching in the dense medium. Other measurements, like the statistical measurement of the disappearance of back–to–back jets, support the conclusion.

Preliminary measurements of the nuclear modification in $Au+Au$ collisions at $\sqrt{s_{NN}} = 62.4\,\mathrm{GeV}$ indicates a slight suppression in the central collisions and an enhancement for the semi–peripheral collisions. This is in agreement with the expectations from extrapolation between SPS and top RHIC energy results.

The magnitude of the suppression in the $Au + Au$ collisions has been interpreted using different jet–quenching models. These models are based on calculations of the energy loss of partons or hadrons in the dense partonic or hadronic medium. Assumptions on the extension and dynamics of the medium are necessary in order to extract information on the medium density. The strength of the high p_T suppression shows that the jet–quenching must be due to parton radiative energy loss, i.e. gluon radiation. With the present theoretical knowledge and reasonable assumptions on the collision dynamics, it is estimated that the energy density in the central $Au + Au$ collisions reaches $12 - 20\,\mathrm{GeV/fm}^2$. At these densities the medium cannot consist of individual hadrons.

Interpretation of the suppression in the forward direction ($\eta = 2.2$) is more uncertain, since the longitudinal dynamics (and extension) of the medium becomes more important. Moreover, the particles produced at higher rapidities can be affected by saturation in the nucleus with the rapidity of the opposite sign, i.e. the nucleus moving away from the detector. Measurements of the yields in $d + Au$ collisions at forward rapidities are consistent with model calculations including saturation of the gold nucleus. The lack of detailed measurements and better theoretical understanding makes the observation suggestive, but not conclusive. The saturation in the $Au + Au$ collisions is expected to play a smaller role at forward rapidities, since the high rapidity region is only sensitive to the low$-x$ parton distribution in the nucleus moving away from the detector. A detailed calculation of jet energy loss in an expanding hydrodynamical medium (produced in the $Au + Au$ collisions) reproduces the data at two pseudo–rapidities ($\eta = 0$ and $\eta = 2.2$). In general, theoretical studies on the high p_T particle production at forward rapidities in $Au + Au$ collisions are sparse.

Due to the design of the detectors and the limited statistics obtained during the first years of operation, the primary focus (in this work as well as in most other high p_T studies so far) has been on the unidentified hadrons. The yields of pions and protons have been measured up the $p_T \approx 4.5\,\mathrm{GeV/c}$. These yields show that the high p_T suppression is due to suppression of mesons, while the baryons are not suppressed. This has been explained by different mechanisms, e.g. quark recombination and radial flow that boosts the baryons more than the mesons. With the analysis of the 2004 RHIC data, the high p_T suppression pattern of identified particles will be extended to higher p_T and extensive studies of the fragmentation and recombination processes can begin.

Detailed and quantitative description of the nuclear effects can only be achieved with reference measurements at the same energy (and with the same detectors). The understanding of the jet–quenching mechanisms in both cold and hot/dense matter, the fragmentation/recombination processes and the modification of the parton distribution functions in the fast moving nuclei is far from complete. Most of the theoretical work (with predictive power) is to a large extend based on phenomenological descriptions and the links to the fundamental physical processes are not fully developed. More data on $d + A$ ($p + A$), $p + p$ and eventually $e + A$, which could be realized with the proposed upgrade of RHIC to eRHIC, are crucial for the detailed understanding of the mechanisms behind high p_T particle production.

The field of high p_T particle production in heavy ion collisions has indeed flourished since RHIC started operating. Many important conclusions have been made and the high p_T region will undoubtedly reveal new interesting physics in the future. The BRAHMS experiment will play an important role with its unique ability to perform detailed high p_T measurements at forward rapidities.

During the spring and summer of 2004, the four RHIC collaborations have written so–called whitepapers that express the collaborations interpretations of the measurements. Also, theorists in the field have written up their thoughts on the results. In all these papers, the high p_T results are used as a key argument for the discovery of extremely dense deconfined matter. The bulk of theorists do not hesitate to call the observed matter a quark gluon plasma. For example, Gyulassy and McLerran state that the RHIC data "are so striking and decisive that several strong physics conclusions can already be drawn. They establish empirically that a special form of strongly coupled QGP (sQGP) exists with remarkable properties." [32]. The experimentalists are more careful – none of the four RHIC experiments state that they have found evidence for the QGP. For example, the BRAHMS whitepaper reads: "...the high density phase that is observed, is not identical to the idealized QGP as it was imagined a decade or two ago.". In general the experimentalist seems to dislike the idea of calling the observed high density medium a QGP because it has different properties than the QGP people had in mind ten years ago (it is short lived and strongly interacting). At the same time they do not hesitate to argue that the medium shows evidence of deconfinement and early thermalization. At this point, the question is perhaps more semantic than scientific – the discussion tends to get more focused on what to call the dense matter than what its actual properties and characteristics are.

Appendix A

Variables and the Coordinate Systems

Table A.1 lists the kinematic variables used to describe particles emitted from a heavy ion collision.

Notation	
x, y, z	cartesian coordinates
θ	polar angle
ϕ	azimuthal angle
m	rest mass
p	momentum
E	energy
p_T	transverse momentum
m_T	transverse mass
$k_T = p_T/\hbar$	transverse momentum
y	rapidity
η	pseudo–rapidity
x_F	Feynmann–x
x_{Bj}	Bjorken scaling variable

Table A.1: List of kinematic variables.

The Coordinate System

The cartesian coordinate of the experiment system is placed so that the $y-$axis is the axis of the two colliding beams and the $x-$axis points away from the center of the accelerator (see figure A.1). The *local* coordinate systems of the sub–detector systems are differennt – here, the $z-$axis points away from the nominal interaction point and the $y-$axis points up. The polar and azimuthal angles (θ and ϕ) are defined as normally, see figure A.2.

The Kinematic Variables

The transverse momentum is defined as the momentum in the transverse plane $p_T = \sqrt{p_x^2 + p_z^2} = p|\sin\theta|$, while the transverse mass is defined $m_T^2 = p_T^2 + m^2$. To describe the longitudinal motion of a particle, the rapidity is used

$$y = \frac{1}{2}\left(\frac{E + p_z}{E - p_z}\right) = \frac{1}{2}\left(\frac{1 + \beta\cos\theta}{1 - \beta\cos\theta}\right), \tag{A.1}$$

where E is the energy of the particle ($E^2 = p^2 + m^2$). The rapidity has the advantage that it is additive under a Lorentz boost, i.e. $y' = y + y_{boost}$. The pseudo–rapidity η is defined

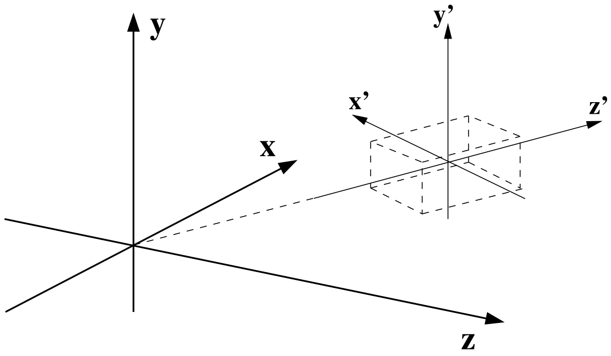

Figure A.1: The origin of the global coordinate system used by BRAHMS is placed at the nominal interaction point, the $z-$axis goes along the beam line and the $x-$axis points away from the middle of the accelerator. The definition of the local coordinate system (x', y', x') is also shown.

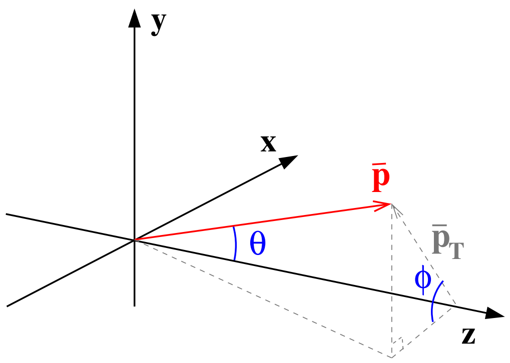

Figure A.2: The polar angle θ is the angle between the paticle momentum vector and the beam axis. The azimuthal angle is the angle between the $x-$axis and the transverse momentum vector.

$$\eta = \frac{1}{2}\left(\frac{p+p_z}{p-p_z}\right) = \frac{1}{2}\left(\frac{1+\cos\theta}{1-\cos\theta}\right) = -\ln\left(\tan\frac{\theta}{2}\right). \tag{A.2}$$

Note that in the pseudo–rapidity equals the rapidity in the limit of vanishing mass or infinite momentum.

The Parton Model

The parton model was developed by Feynman to describe the observed cross–sections the deep inelastic scattering. The fact that the cross–sections are large (compared to the elastic scattering cross–section) and weakly dependent on the momentum transfer indicates that the nucleon have pointlike constituents. Feynman named these constituents the *partons*. Each parton carries a fraction x_F of the total momentum of the nucleon. In a reference frame where the nucleon has a very large momentum (the infinite momentum frame), the Feynman x_F is equivalent to the emperical Bjorken scaling varaible. This is defined $x_{Bj} = q^2/2M\nu$, where q is the momentum transfer, M is the mass of the of the nucleon and ν is the energy transfer (evaluated in the laboratory system). Often the label (F or Bj) is left out and the bare x is simply used. Figure A.3 shows schematic picture of a deep inelastic scattering.

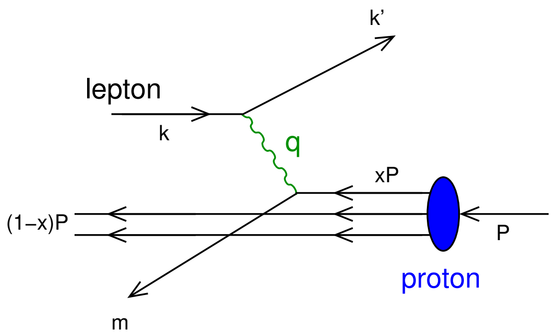

Figure A.3: Lepton parton collision via single photon exchange.

The cross–section are expressed in terms of the structure functions $F(x)$, which then can be accessed experimentally. In the parton model, the structure functions can be written as the sum of the parton distribution functions $f_q(x)$ (here q denotes the different quark flavors). The function $xf_q(x)$ is the density of quarks of flavor q as function of x. More on the parton model can be found in ref. [94].

Appendix B

The Power–Law

Throughout the thesis the term power–law is used for a function of the form

$$f(p_T) = A\left(1 + \frac{p_T}{p_0}\right)^{-n}, \tag{B.1}$$

where p_0 and n are the power–law parameters and A is a normalization constant. If the differential yield (the spectrum in p_T) is fitted with a power–law, the total yield at that (pseudo–)rapidity can be extracted by integrating[1] over p_T:

$$\frac{dN}{d\eta} = \int_0^\infty 2\pi p_T A\left(1 + \frac{p_T}{p_0}\right)^{-n} dp_T = 2\pi A \frac{p_0^2}{(n-2)(n-1)}. \tag{B.2}$$

Typical fits to the spectra gives $n > 15$, so the requirement that $n \neq 1, 2$ is fulfilled. The constant A can now be written

$$A = \frac{(n-1)(n-2)}{2\pi p_0^2}\frac{dN}{d\eta}. \tag{B.3}$$

Also, the mean p_T can be extracted from a power–law fit to the differential yields by integrating[2]:

$$\langle p_T \rangle = \frac{\int_0^\infty 2\pi p_T^2 A\left(1 + \frac{p_T}{p_0}\right)^{-n} dp_T}{\int_0^\infty 2\pi p_T A\left(1 + \frac{p_T}{p_0}\right)^{-n} dp_T} = \frac{2p_0}{n-3} \tag{B.4}$$

[1]Using that $\int x(ax+b)^c dx = \frac{(ax+b)^{c+2}}{(c+2)a^2} - \frac{b(ax+b)^{c+1}}{(c+1)a^2}, c \neq 1, 2.$

[2]Using that $\int x^2(ax+b)^c dx = \frac{(ax+b)^{c+3}}{(c+3)a^3} - \frac{2b(ax+b)^{c+2}}{(c+2)a^3} + \frac{b^2(ax+b)^{c+1}}{(c+1)a^3}, c \neq 1, 2, 3$

Appendix C

Bending Angle Resolution Derivation

The relation between the combined tracking angle resolution $\sigma_{\Delta\theta}$ and the resolution of the matching angle parameter $\sigma_{\Delta\psi}$ can be derived the following way. It is first assumed that the tracks comes from the middle of the tracking detectors. Assuming that the tracks originate from points in the tracking detectors (front and back) with x coordinates x_f and x_b and that they have the $x-$slopes $\sin\theta_f$ and $\sin\theta_b$. The distance from these points to the effective edge of magnetic field in the $z-$direction are L_f and L_b and the length of the magnet is L_{mag}. The angle ω of the matching line ($|FB|$ in figure 4.4) is given by

$$\sin\omega = \frac{x_f + L_f\sin\theta_f - (x_b - L_b\sin\theta_b)}{L_{mag}}. \tag{C.1}$$

Since $\psi_f = \theta_f - \omega$ and $\psi_b = \omega - \theta_b$ (see figure 4.4) and the the angles (ω,θ_f and θ_b) are small, the small angle approximation can be used and the matching parameter can be written

$$\Delta\psi = \psi_f - \psi_b = \theta_f + \theta_b - \frac{2(x_f - x_b + L_f\theta_f - L_b\theta_b)}{L_{mag}} \tag{C.2}$$

Error analysis show, ignoring the errors on x_f,x_b,L_f and L_b,

$$\sigma^2_{\Delta\psi} = \sigma^2_{\theta_f} + \sigma^2_{\theta_b} + \left(\frac{2L_f\sigma_{\theta_f}}{L_{mag}}\right)^2 + \left(\frac{2L_b\sigma_{\theta_b}}{L_{mag}}\right)^2. \tag{C.3}$$

The quantity $\sigma^2_{\theta_f}+\sigma^2_{\theta_b}$ is the bending angle resolution squared (without the contribution from multiple scattering). Now assuming that the angular resolutions of the two tracking detectors are similar ($\sigma_{\theta_f} \approx \sigma_{\theta_b}$) and that the distances to the magnet are similar ($L = L_f \approx L_b$),

$$\sigma^2_{\Delta\psi} \approx (\sigma^2_{\theta_f} + \sigma^2_{\theta_b})\left(1 + \left(\frac{2L}{L_{mag}}\right)^2\right) = \sigma^2_{\theta_{f+b}}\left(1 + \left(\frac{2L}{L_{mag}}\right)^2\right). \tag{C.4}$$

Here defining $\sigma^2_{\theta_{f+b}} = \sigma^2_{\theta_f} + \sigma^2_{\theta_b}$. Equation C.4 shows that the angular resolution of the matching parameter is bigger than the bending angle resolution. The modification depends on the distance from the tracking detectors to the magnet and on the length of the magnetic field L_{mag}.

Appendix D

The BRAHMS Collaboration

(2003)

I. Arsene[10], I. G. Bearden[7], D. Beavis[1], C. Besliu[10], B. Budick[6], H. Bøggild[7], C. Chasman[1], C. H. Christensen[7], P. Christiansen[7], J. Cibor[3], R. Debbe[1], E. Enger[12], J. J. Gaardhøje[7], M. Germinario[7], K. Hagel[8], H. Ito[1], A. Jipa[10], F. Jundt[2], J. I. Jørdre[9], C. E. Jørgensen[7], R. Karabowicz[4], E. J. Kim[1,11], T. Kozik[4], T. M. Larsen[12], J. H. Lee[1], Y. K. Lee[5], S. Lindal[12], R. Lystad[9], G. Løvhøiden[12], Z. Majka[4], A. Makeev[8], M. Mikelsen[12], M. Murray[8,11], J. Natowitz[8], B. Neumann[11], B. S. Nielsen[7], D. Ouerdane[7], R. Płaneta[4], F. Rami[2], C. Ristea[10], O. Ristea[10], D. Röhrich[9], B. H. Samset[12], D. Sandberg[7], S. J. Sanders[11], R. A. Scheetz[1], P. Staszel[7], T. S. Tveter[12], F. Videbæk[1], R. Wada[8], Z. Yin[9], and I. S. Zgura[10]

[1] Brookhaven National Laboratory, Upton, New York 11973
[2] Institut de Recherches Subatomiques and Université Louis Pasteur, Strasbourg, France
[3] Institute of Nuclear Physics, Krakow, Poland
[4] Smoluchkowski Inst. of Physics, Jagiellonian University, Krakow, Poland
[5] Johns Hopkins University, Baltimore 21218
[6] New York University, New York 10003
[7] Niels Bohr Institute, Blegdamsvej 17, University of Copenhagen, Copenhagen 2100, Denmark
[8] Texas A&M University, College Station, Texas, 17843
[9] University of Bergen, Department of Physics, Bergen, Norway
[10] University of Bucharest, Romania
[11] University of Kansas, Lawerence, Kansas 66049
[12] University of Oslo, Department of Physics, Oslo, Norway

Bibliography

[1] R. Barate *et al.* , Phys. Rept **294**, 1–165 (1998).

[2] LEPS Collaboration, T. Nakano *et al.* , Phys. Rev. Lett. **91**, 012002 (2003).

[3] S. Muroya, A. Nakamura, C. Nonaka, and T. Takaishi , Prog. Theor. Phys. **110**, 615–668 (2003).

[4] Z. Fodor and S. D. Katz , Phys. Lett. **B534**, 87–92 (2002).

[5] K. G. Wilson , Phys. Rev. **D10**, 2445–2459 (1974).

[6] F. Karsch , Nucl. Phys. **A698**, 199 (2002).

[7] C. A. Oligvie , Nucl. Phys. **A698**, 3 (2002).

[8] C. Lourenco , Nucl. Phys. **A698**, 13 (2002).

[9] X.-N. Wang and M. Gyulassy , Phys. Rev. **D44**, 3501 (1991).

[10] BRAHMS Collaboration, I. G. Bearden *et al.* , Phys. Lett. **B523**, 227–233 (2001).

[11] BRAHMS Collaboration, I. G. Bearden *et al.* , Phys. Rev. Lett. **88**, 202301 (2002).

[12] PHOBOS Collaboration, B. B. Back *et al.* , Phys. Rev. **C65**, 061901 (2002).

[13] PHENIX Collaboration, K. Adcox *et al.* , Phys. Rev. Lett **86**, 3500 (2001).

[14] PHOBOS Collaboration, B. B. Back *et al.* , Submitted to Phys. Rev. Lett., `nucl-ex/0301017`.

[15] P. J. Siemens and J. O. Rasmussen , Phys. Rev. Lett. **42**, 880 (1979).

[16] E. Schnedermann and U. Heinz , Phys. Rev. **C 47**, 1738 (1993).

[17] STAR Collaboration, J. Adams *et al.* , Phys. Rev. Lett. **92**, 112301 (2004).

[18] I. Bearden *et al.* , BRAHMS note (to be published).

[19] F. Retiere *et al.* , J. Phys. **G30**, S827–S834 (2004).

[20] PHENIX Collaboration, S. S. Adler *et al.* , Phys. Rev. Lett. **91**, 182301 (2003).

[21] STAR Collaboration, J. Adams *et al.* , Phys. Rev. Lett. **92**, 062301 (2004).

[22] STAR Collaboration, K. H. Ackermann *et al.* , Phys. Rev. Lett. **86**, 402–407 (2001).

[23] P. F. Kolb and U. Heinz **,** `nucl-th/0305084`.

[24] P. Braun-Munzinger, J. Stachel, and C. Wetterich , Phys. Lett. **B596**, 61 (2004).

[25] F. Becattini, M. Gazdzicki, A. Keranen, J. Manninen, and R. Stock , Phys. Rev. **C69**, 024905 (2004).

[26] PHENIX Collaboration, S. S. Adler *et al.* , Phys. Rev. **C69**, 034909 (2004).

[27] BRAHMS Collaboration, I. G. Bearden *et al.* , Phys. Rev. Lett. **90**, 102301 (2003).

[28] P. Braun-Munzinger and J. Stachel , J. Phys. **G28**, 1971–1976 (2002).

[29] BRAHMS Collaboration, I. G. Bearden *et al.* , Submitted to Phys. Rev. Lett., `nucl-ex/0312023`.

[30] J. D. Bjorken , Phys. Rev. **D27**, 140 (1983).

[31] F. Videbaek and O. Hansen , Phys. Rev. **C52**, 2684–2693 (1995).

[32] M. Gyulassy and L. McLerran **,** `nucl-th/0405013`.

[33] BRAHMS Collaboration, I. G. Bearden *et al.* , Whitepaper (to be published).

[34] F. Karsch , Nucl. Phys. **A590**, 367 (1995).

[35] J. F. Owens , Rev. Mod. Phys. **59**, 465 (1987).

[36] J. C. Collins, D. E. Soper, and G. Sterman , Nucl. Phys. **B308**, 833 (1988).

[37] K. Gallmeister, C. Greiner, and Z. Xu , Phys. Rev. **C67**, 044905 (2003).

[38] J. Cronin , Phys. Rev. **D11**, 3105 (1975).

[39] A. Airapetian , Phys. Lett **B557**, 37 (2003).

[40] A. Accardi , `hep-ph/0212148`.

[41] X.-N. Wang , Phys. Rept. **280**, 287 (1997).

[42] X.-N. Wang , Phys. Rev. **C61**, 064910 (2000).

[43] G. Barnafoldi, G. Papp, P. Levai, and G. Fai , To be published in J. Phys. G, `nucl-th/0404012`.

[44] R. C. Hwa and C. B. Yang `nucl-th/0403001`.

[45] M. Arneodo , Phys. Rep. **240**, 301 (1994).

[46] A. Bodek *et al.* , Phys. Rev. Lett. **50**, 1431 (1983).

[47] M. Arneodo *et al.* , Nucl. Phys. **B441**, 12–30 (1995).

[48] Y. L. Dokshitzer , Sov. Phys. JETP **46**, 641 (1977).

[49] V. N. Gribov and L. N. Lipatov , Sov. J. Nucl. Phys. **15**, 438 and 675 (1972).

[50] G. Altarelli and G. Parisi , Nucl. Phys. **B126**, 298 (1977).

[51] E. Iancu and R. Venugopalan `hep-ph/0303204`.

[52] A. Accardi and M. Gyulassy , `nucl-th/0304083`.

[53] A. Accardi *et al.* `hep-ph/0308248`.

[54] D. Kharzeev and M. Nardi , Phys. Lett. **B507**, 121–128 (2001).

[55] D. Kharzeev, Y. V. Kovchegov, and K. Tuchin , Phys. Rev. **D68**, 094013 (2003).

[56] I. Vitev , To be published in J. Phys. G, `hep-ph/0403089`.

[57] R. Baier, D. Schiff, and B. G. Zakharov , Ann. Rev. Nucl. Part. Sci. **50**, 37–69 (2000).

[58] L. D. Landau and I. Pomeranchuk , Dokl. Akad. Nauk Ser. Fiz. **92**, 735 and 738 (1953).

[59] A. B. Migdal , Phys. Rev. **103**, 1811 (1956).

[60] I. Vitev and M. Gyulassy , Phys. Rev. Lett. **89**, 252301 (2002).

[61] X.-N. Wang , Phys. Lett. **B579**, 299–308 (2004).

[62] X.-N. Wang and M. Gyulassy , Comp. Phys. Comm. **83**, 1994 (307).

[63] X.-N. Wang and M. Gyulassy , Phys. Rev. Lett. **68**, 1480 (1992).

[64] K. J. Eskola, V. J. Kolhinen, and C. A. Salgado , Eur. Phys. J. **C9**, 61–68 (1999).

[65] I. Vitev, P. Levei, and M. Gyulassy , Phys. Lett. **B538**, 282 (2002).

[66] W. Cassing, K. Gallmeister, and C. Greiner , Nucl. Phys. **A735**, 277–299 (2004).

[67] W. Ehehalt and W. Cassing , Nucl. Phys. **A602**, 449–486 (1996).

[68] B. Andersson, G. Gustafson, and B. Nilsson-Almqvist , Nucl. Phys. **B281**, 289 (1987).

[69] W. Cassing, K. Gallmeister, and C. Greiner , J. Phys. **G30**, S801–S808 (2004).

[70] T. Hirano and Y. Nara , Phys. Rev. **C68**, 064902 (2003).

[71] T. Hirano and K. Tsuda , Phys. Rev. **C66**, 054905 (2002).

[72] I. I. Balitsky and L. N. Lipatov , Sov. J. Nucl. Phys. **28**, 822 (1978).

[73] E. A. Kuraev, L. N. Lipatov, and V. S. Fadin , Sov. Phys. JETP **45**, 199 (1977).

[74] E. Iancu , `hep-ph/0309044`.

[75] L. McLerran `hep-ph/0402137`.

[76] H. Hahn *et al.* , Nucl. Instrum. Meth. **A499**, 245 (2003).

[77] STAR Collaboration, K. H. Ackermann *et al.* , Nucl. Instrum. Meth. **A499**, 624–632 (2003).

[78] PHENIX Collaboration, K. Adcox *et al.* , Nucl. Instrum. Meth. **A499**, 469–479 (2003).

[79] PHOBOS Collaboration, B. B. Back *et al.* , Nucl. Instrum. Meth. **A499**, 603–623 (2003).

[80] BRAHMS Collaboration, M. Adamczyk *et al.* , Nucl. Instrum. Meth. **A499**, 437–468 (2003).

[81] D. Ouerdane. PhD thesis, University of Copenhagen, 2003.

[82] C. Adler *et al.* , Nucl. Instrum. Meth. **A470**, 488 (2001).

[83] E. S. Jakobsen Master's thesis, University of Copenhagen, 2001.

[84] C. H. Christensen Master's thesis, University of Copenhagen, 2003.

[85] H. Ito. PhD thesis, Kansas University, 2002.

[86] P. Christiansen. PhD thesis, University of Copenhagen, 2003.

[87] J. I. Jorde Master's thesis, University of Bergen, 2001.

[88] R. Debbe *et al.* , Nucl. Instrum. Meth. **A371**, 327 (1996).

[89] R. Debbe *et al.* , Nucl. Instrum. Meth. **A362**, 253 (1995).

[90] F. Videbæk *et al.* , BRAHMS web server (http://pii3.brahms.bnl.gov/ operator/).

[91] R. Brun and F. Rademakers , Nucl. Instrum. Meth. **A389**, 81–86 (1997).

[92] C. Christensen and F. Videbæk , BRAHMS Analysis Toolkit (http://pii3/brahms/bnl.gov/ brahmlib/brat/guide).

[93] K. Hagel , personal correspondance.

[94] D. Haidt and P. Zerwas, *Eur. Phys. J. C, Volume 3, Particle and Fields.* Springer, 1 ed., 1998.

[95] Z. Yin. PhD thesis, University of Bergen, 2004.

[96] BRAHMS Collaboration, I. Arsene *et al.* , Phys. Rev. Lett. **91**, 072305 (2003).

[97] BRAHMS Collaboration, I. Arsene *et al.* , Submitted to Phys. Rev. Lett., `nucl-ex/0403005`.

[98] R. Brun, F. Carminatti, and F. Rademarkers. GEANT (http://wwwinfo.cern.ch/asd/geant/).

[99] T. Larsen Master's thesis, University of Oslo, 2003.

[100] E.-J. Kim, 'Internal note.' 2002.

[101] UA1 Collaboration, A. C. *et al.* , Nucl. Phys. **B335**, 261 (1990).

[102] B. Alper *et al.* , Nucl. Phys. **B100**, 237 (1975).

[103] STAR Collaboration, J. Adams *et al.* , To be published in Phys. Rev. C, `nucl-ex/0404020`.

[104] BRAHMS Collaboration, I. Arsene *et al.* `nucl-ex/0401025`.

[105] X.-N. Wang `nucl-th/0405017`.

[106] WA98 Collaboration, M. M. Aggarwal *et al.* , Phys. Rev. Lett. **81**, 4087–4091, [Erratum–ibid.84:578–579,2000] (1998).

[107] CERES Collaboration, G. Agakishiev *et al.* `hep-ex/0003012`.

[108] D. d'Enterria , Phys. Lett. **B596**, 32 (2004).

[109] E. Wang and X.-N. Wang , Phys. Rev. **C64**, 034901 (2001).

[110] X.-N. Wang , nucl-th/0405029.

[111] PHENIX Collaboration, S. S. Adler *et al.* , Phys. Rev. **C69**, 034910 (2004).

[112] STAR Collaboration, J. Adams *et al.* , Phys. Rev. Lett. **91**, 172302 (2003).

[113] PHOBOS Collaboration, B. B. Back *et al.* , Phys. Lett. **B578**, 297–303 (2004).

[114] STAR Collaboration, J. Adams *et al.* , Phys. Rev. Lett. **91**, 072304 (2003).

[115] PHENIX Collaboration, S. S. Adler *et al.* , Phys. Rev. Lett. **91**, 072303 (2003).

[116] PHOBOS Collaboration, B. B. Back *et al.* , Submitted to Phys. Rev. C Rapid Comm., nucl-ex/0406017.

[117] PHENIX Collaboration, S. S. Adler *et al.* , Phys. Rev. Lett. **91**, 172301 (2003).

[118] R. C. Hwa and C. B. Yang , Phys. Rev. **C69**, 034902 (2004).

[119] V. Greco, C. M. Ko, and P. Levai , Phys. Rev. Lett. **90**, 202302 (2003).

[120] J. Bjorken , Report No. Fermilab-Pub-82/59-THY (1982).

[121] STAR Collaboration, K. Schweda , J. Phys. **G30**, S693–S700 (2004).

[122] STAR Collaboration, F. Wang , J. Phys. **G30**, S1299–S1304 (2004).